science.sciencemag.org/content/371/6528/498/suppl/DC1

Supplementary Materials for

Reversible disorder-order transitions in atomic crystal nucleation

Sungho Jeon*, Taeyeong Heo*, Sang-Yeon Hwang*, Jim Ciston, Karen C. Bustillo, Bryan W. Reed, Jimin Ham, Sungsu Kang, Sungin Kim, Joowon Lim, Kitaek Lim, Ji Soo Kim, Min-Ho Kang, Ruth S. Bloom, Sukjoon Hong, Kwanpyo Kim, Alex Zettl, Woo Youn Kim, Peter Ercius†, Jungwon Park†, Won Chul Lee†

*These authors contributed equally to this work.
†Corresponding author. Email: wonchullee@hanyang.ac.kr (W.C.L.); jungwonpark@snu.ac.kr (J.P.); percius@lbl.gov (P.E.)

Published 29 January 2021, *Science* **371**, 498 (2021)
DOI: 10.1126/science.aaz7555

This PDF file includes:

Other Supplementary Material for this manuscript includes the following:
(available at science.sciencemag.org/content/371/6528/498/suppl/DC1)

Movies S1 to S7 (.mp4)

Materials and methods

1.1 Sample preparation

The method for synthesizing gold cyanide (AuCN) nanoribbons is reproduced from previous works (*19, 20*). In brief, the AuCN nanoribbons are synthesized on graphene by putting Au nanoparticles and the graphene together into an ammonium persulfate ($(NH_4)_2S_2O_8$) solution. The detailed preparation steps are as follows (fig. S2A). (i) The graphene is transferred onto Quantifoil holey carbon TEM (transmission electron microscope) grids using the direct transfer method (*33*), i.e., after placing the Quantifoil TEM grid onto a graphene-covered copper (Cu) foil with the graphene side facing up, 2.5 μL of IPA is dropped onto the sample to wet the interface, and then the sample is dried at 85 ˚C on a hot plate for 15 minutes to promote adhesion between the carbon film and the graphene. (ii) The Cu foil is etched by floating the sample on an aqueous solution of 113 mM $(NH_4)_2S_2O_8$ for 1 hour. (iii) Au nanoparticles (spherical nanoparticles of 8 nm in diameter or nanorods of 25 nm in diameter and 73 nm in length, purchased from Nanopartz Inc.) dispersed in organic solvents are dropped and dried on the grids. (iv) The grids are floated on an aqueous solution of 250 mM $(NH_4)_2S_2O_8$ for 10 hours to initiate nanoribbon growth on the graphene and rinsed by transferring the grids to deionized water multiple times.

An alternative method using Au grid mesh of a TEM grid as an Au precursor (fig. S2B) is implemented likewise for the sample preparation. In this method, the graphene-covered Cu foil is partially cut beforehand to expose the Au grid mesh to the reaction solution during the incubation. After the graphene transfer, the sample is floated on the 250 mM $(NH_4)_2S_2O_8$ solution for 17 hours to etch the Cu foil and incubate the nanoribbons. Both methods yield analogous AuCN nanoribbons on graphene for further investigations.

The pre-synthesized Au particles for a control experiment (section 4.1) are synthesized by a method inspired by the work of Brust and Schiffirin. Thiol ligands including 6-mercaptohexanoic acid (MHA), cysteine (Cys), and p-mercaptobenzoic acid (p-MBA) are utilized to synthesize Au particles of desired size (< ~ 2 nm in diameter) (*34-36*). The solution containing Au particles was dropped and dried on the graphene-covered grids fabricated by the same method explained above.

1.2 Electron microscopy

Most of the high-speed movies were acquired by the transmission electron aberration-corrected microscope 1 (TEAM I), a modified FEI Titan TEM equipped with a high-brightness Schottky-field emission electron source (X-FEG), spherical- and chromatic-aberration corrector and a Gatan K2 IS direct electron detector (fig. S1B) at the National Center for Electron Microscopy within the Molecular Foundry in Lawrence Berkeley National Laboratory. The aberration-corrector is aligned for approximately -10 μm third-order spherical aberration (C_3 or $C_{3,0}$) which allows an optimal phase contrast with slight positive defocus. We operated the microscope at 300 kV, which yields a theoretical information limit of 0.065 nm. Using the direct electron detector, images of 1920 × 1792 (pixel size: 0.0203 nm) were captured every 2.5 ms, and 4 successive frames were averaged to reduce noise for all of the presented data, yielding the resultant temporal resolution of 10 ms for the final images. It is noteworthy that the previous microscopic studies of atomic or molecular nucleation were limited to *ex-situ* observations in atomic/molecular-scale (*9, 14, 16*) and in-situ TEM observations with maximum temporal resolution of ~0.1 – 1 s (*4, 5, 10, 12, 13, 15*).

As we aim to observe crystal nucleation and growth from the very first stage of the process, it is important to minimize the electron dose on the target AuCN nanoribbon before the investigation (i.e., capturing a high-speed movie), because AuCN nanoribbons are reduced to Au

atoms once they are exposed to the electron beam (e-beam). Consequently, we pursued the following strategy (fig. S1D), which is explained with imaging procedures of TEAM I as an example:

1. We find an auxiliary AuCN nanoribbon near the target AuCN nanoribbon at low current density ($3 \times 10^3 – 8 \times 10^3$ A/m^2).
2. TEM imaging parameters – focus, magnification, beam convergence, etc. – are adjusted and saved for the optimum imaging of the auxiliary AuCN nanoribbon. At the optimum condition, the current density ranged from 7×10^6 to 10×10^6 A/m^2.
3. The electron beam is now turned back to the low current density and the target AuCN nanoribbon is moved to the center of the electron beam.
4. As soon as the positioning is complete, the shutter is immediately closed to block the electron beam.
5. The imaging parameters saved from the auxiliary AuCN nanoribbon are loaded and recording of a high-speed movie starts as the shutter opens.

In this way, each target nanoribbon is only exposed to a low current density for less than 10 seconds before capture of a high-speed movie. The electron dose in these 10 seconds is equal to that delivered in 3 – 11 ms (or 0.3 – 1.1 frame) during the high-speed observation. This value is presumed to be insignificant for investigating the early stage of crystal nucleation and growth processes. As the vertical positions of the neighboring AuCN nanoribbons were slightly different, the high-speed movie of the target AuCN nanoribbon was not always focused tightly. Among more than 150 observations following this method, we selected 24 well-focused movies for further analyses.

Other movies acquired at higher temporal resolution (1.6 ms) were captured using the ThemIS (operated at 200 kV), an FEI TEM equipped with an X-FEG gun, an image aberration corrector, and a Ceta2 complementary metal oxide semiconductor (CMOS) camera. The Ceta2 is capable of capturing 2048 × 2048 resolution images at 39 fps (frames per second). To increase the frame rate, we added an electrostatic subframing (ES) system to the ThemIS as shown in fig. S1C (*21*). The ES system includes an electrostatic deflector placed after the TEM projector lens, using a design based on the system used in Movie Mode Dynamic TEM (*37, 38*). As configured for the present work, the deflector rapidly switches among a discrete set of 16 subframe positions on the camera in a 4x4 array. The deflection sequence is synchronized with the camera readout so that each camera frame produces 16 distinct images, each roughly 500 × 500 pixels in size (452 × 465 pixels in the present case, after trimming off the overlap regions and dead space at the edges). This raises the frame rate by a factor of 16 to 624 fps (around 1.6 ms per frame). The camera and ES system can run in this mode continuously at a near-100% duty cycle.

Other movies acquired at low dose rates (6.6×10^2 to 1.3×10^4 A/m^2 or 41 to 810 e$^-$/Å^{2}s) were captured using the JEM-ARM200F (operated at 80 kV and 200 kV), equipped with a spherical aberration corrector in the objective lens and an OneView camera. The OneView camera is capable of capturing 2048 × 2048 resolution images at 100 fps (frames per second). The frames from JEM-ARM200F are also averaged likewise and the resultant temporal resolution is 40 ms for the averaged image.

1.3 Image processing

For all images shown in this paper, low-pass filtering with a 0.1 nm cut-off wavelength was applied to reduce high-frequency noise, while the image processing procedures explained below were performed using the original images.

To extract information about the sizes, shapes, and orientations of the nanocrystals, we analyzed discrete Fourier transform images produced by the fast Fourier transform (FFT) algorithm. We used the intensity of the strongest peak in the FFT image (omitting zero-frequency peak or peaks from AuCN by applying reciprocal mask) as a measure of the degree of crystallinity of a selected nanoparticle. To reduce background noise effects for this calculation, the FFT was performed only at the 0.8-nm-radius circular region centered on the nanoparticle (fig. S7). The typically produced data are shown in Fig. 1C.

The determination of the shape and orientation of the nanoparticle under concern was based on the further analysis of the FFT of the full image as shown in figs. S8 and S9. To determine the shape, we applied geometric phase analysis (GPA), a widely used method to deduce the lattice area from an FFT peak (*39*) (fig. S8). First, we applied a fifth-order Butterworth notch filter with a cut-off wavelength of 0.1 nm to the selected peak. Then, a certain area around the FFT peak is cropped and placed in the center of a void image that has the same size as the original image. An inverse Fourier transform then yields an estimate of the real-space image of the region associated with the selected peak. The filtered image was binarized with a threshold to produce an estimate of the shape and projected area of the nanoparticle. The error bars in the areal plot (Fig. 1E, fig. S17F - S21F, and fig. S25E) are calculated by applying three different threshold values for binarization (Exemplary images showing the areal change depending on the three-threshold values are shown in fig. S8C and fig. S8D).

The three-dimensional orientation of the crystal was determined in two steps. First, the angular position of the brightest spot in the FFT image was determined, using interpolation to improve precision (fig. S8). The outcome provided one of the three orientational degrees of freedom. This method is also used to plot nanocrystal <111> direction (Fig. 1F, fig. S17G – S21G, and fig. S25F) where we selected the brightest spot that corresponds to <111> direction using the reciprocal mask explained above (fig. S8). The error bars in the plot are deduced from the full width at half maximum (FWHM) of the FFT intensity peak. To determine the other two degrees of freedom, we compared the FFT image to the library of simulated diffraction patterns with various electron-beam directions through the crystal (fig. S9) (*40*). These patterns were rotated in plane to match the angle known from the peak position, and we selected the pattern with the largest correlation with the power spectrum of the original real-space image.

Having the three-dimensional orientation and projected area, we estimated the three-dimensional atomic model of the nanocrystal by constructing an ideal lattice of the correct orientation and cropping it to half of an ellipsoid. The major axis, minor axis, and orientation within the plane of the image were determined from the shape of the projected area, and the thickness was set to half of the minor axis.

Finally, the dynamics of gold atoms were displayed by the standard deviation of the intensities of pixels in the image as explained in fig. S10.

1.4 TEM image simulation

We simulated TEM images of Au nanocrystals to validate our experimental TEM images under various conditions. The results of the analysis are described in the next section. The simulations were based on the multi-slice algorithm and simulation code (*40*). The parameters

including accelerating voltage, defocus, third-order aberration, fifth-order aberration, and wobble value were set corresponding to the imaging condition of TEAM1: 300 kV, 15 nm, −10 μm, 3 mm, and 0.1 Å, respectively. The defocus fluctuation was considered as a Gaussian distribution with a standard deviation of 4 nm. To add background noise, we added a graphene image extracted from an experimental TEM image.

1. Overall characteristics of the nucleation and growth processes

We describe the overall characteristics of the crystal nucleation and growth processes in this section. The following four characteristics are presented by deliberately reducing the frame rate of the high-speed movie (movie S1) using frame-averaging (fig. S3A; effective temporal resolution of 0.5 s). First, the in-situ movie shows the decomposition of AuCN nanoribbons (characterized by FFT peaks in fig. S3, B and C) as well as the formation and growth of gold nanocrystals (characterized by lattice fringes in fig. S3A). Second, nucleation sites appear preferentially near boundaries (steps) between AuCN and graphene, following thermodynamic mechanisms described by the TSK (terrace-step-kink) model (*41*). Accordingly, 16 out of 20 nucleation sites appear near the boundaries in the in-situ movie S1. Third, consistent with the Volmer-Weber growth mode (*41*), gold atoms aggregate to form separated islands rather than a continuous 2D layer due to the non-wetting behavior of gold on graphene. Fourth, the average growth speed measured from 5 gold nanoparticles in movie S1 is ~20 atoms per second, which roughly means that one atom is added to a single nanoparticle in every five frames on average. We also note that nanoparticles observed in this study are generally composed of ~20 to ~200 gold atoms.

2. Analysis of TEM image frames with or without lattice fringes

3.1 Interpretation of the appearance and disappearance of lattice fringes

We interpret the appearance and disappearance of lattice fringes in individual video frames as the appearance and disappearance of crystalline order, or at least as a strong proxy thereof. For this interpretation to hold, we must address other possible explanations for the lack of visibility of lattice fringes, including simple tilting of nanoparticles into and out of high-contrast orientations. Based on the following observations, we believe our interpretation is the most plausible, i.e. that the loss of visible lattice fringes corresponds strongly enough with the disappearance of crystalline order to justify the conclusions of the work.

First, in bulk crystals, the disappearance of lattice fringes often means that the crystals are tilted away from low index zone axes. However, recent studies (*22, 26*, *42*), along with simulation results presented herein (fig. S12), indicate that this is no longer true for nanocrystal sizes less than 2 nm under imaging conditions such as those we are using. Instead, lattice fringes are expected to be visible at virtually all orientations, and this should be more prevalent as the particle size is further reduced. We simulated TEM images of hemispherical Au nanocrystals over a wide range of orientations as shown in fig. S12. The Au nanocrystals were modeled to be face cubic centered (FCC); the typical structure of gold crystal at diameters greater than 1.5 nm. The size of the crystal was set to 2 nm in diameter (3.14 nm^2 in area), i.e., larger than most of the crystals analyzed in this article and thus appropriate for testing the plausibility of the interpretation. As shown in fig. S12, lattice fringes were visible in every orientation, with relatively little modulation of contrast. The large changes in lattice fringe visibility found in our experiment therefore cannot be explained by the tilting of crystalline material only.

Second, the fast rotation of nanocrystals within the TEM exposure time (in our case: 10 ms) could be a possible reason for the lattice disappearance. We checked this hypothesis using TEM image simulations (fig. S13), which shows that concentric circles are observed if a nanocrystal rotates at high speed. The concentric circles are invisible only when relatively large lateral motions are added to the fast nanocrystal rotation (fig. S13C). However, these kinds of fast rotations and relatively large lateral motions are not realistic because nanocrystals observed in this study are supported on a solid substrate (graphene). More importantly, this hypothesis is contradictory to experimental TEM images such as fig. S14. In fig. S14, crystalline domains decrease in size and then disappear in successive frames during which lattice orientations did not change (no rotation). However, because the nanocrystal rotation intrinsically includes different orientations of the nanocrystal (fig. S13, B and C), fast rotation cannot be a reason for the lattice disappearance in this study.

Third, irregular vertical drift (or vibration) of the sample was also considered as a reason for the disappearance of the lattice fringes. If the sample or the focus drifted vertically, the AuCN nanoribbon should be also defocused. However, as shown in Fig. 1B the disappearance or defocus of the nanoribbon lattice was not observed while the nanocrystal disappeared numerous times. It is also confirmed in other nucleation sites (fig. S17 – S21 and fig. S27 – S29).

The only reason for the disappearance of the lattice fringes we could find was the structural transition of the nanocrystal to the amorphous state. The nanoparticle images identified as amorphous are consistent with our understanding of evolving metastable amorphous structures as well as previous observations. While the contrast in the TEM image captured at high temporal resolution is poor, it is still observable that disordered dots are changing position in each frame within nucleation sites (The lattice fringes are obscure in a section of movie S2 from 230 ms to 1190 ms, and the dynamic change of the frame during this section is depicted in Fig. 1D). This suggests continuous ongoing atomic-scale evolution at the particle's internal structure, which is not typically associated with crystalline material. In addition, the visual appearance of the disordered dots in the high-resolution TEM (HRTEM) images is consistent with that of other noble metal (Pt) nanoparticles presented in previous studies (*16*, *26*). The data collected from X-ray diffraction (XRD), MD (Molecular Dynamics) simulations, X-ray photoelectron spectroscopy, and measurements of catalyst functionality establish that the Pt nanoparticles lose their crystallinity when the particle size is less than ~1 nm.

3.2 Classification of structural states in each frame of the TEM movies

We applied a universal standard for thresholding of maximum peak intensities in FFT images to classify between disordered and crystalline states without bias. Nonetheless, fluctuating weak signal-to-noise ratio and background signal of each in-situ image can still lead to an ambiguity in the classification while applying the universal threshold. Therefore, we introduced an indicator (purple circle) that represents an undefinable state (gray zone in the disordered/crystalline classification) to improve the clarity of data analysis. In this type of frame, the lattice fringe appears unclear and blurry, which is likely due to the particle being in both states during the acquisition time which is in millisecond regime. Our experimental findings are still valid even with these undefinable frames. Figure S4B shows two extreme cases in which all undefinable frames in the nucleation path of Fig. 1 were assigned as either disordered (upper trajectory) or crystalline (lower trajectory) states. The two trajectories are very similar because the undefinable frames are relatively rare (38 frames out of 1,500 frames) and almost all of them appear during the transition processes from disordered to crystalline states or vice versa, indicating that the frames contain both

states. In these cases, we should label these frames as belonging purely to either one or the other state. In both trajectories, the nucleation process was observed as a structural evolution through dynamic and stochastic fluctuations between the two states. Identifying structural characteristics of a certain frame based on not only the target frame itself but also its neighboring frames (previous and next frames) can improve accuracy of the structural identification. In the beginning of our research, we tested this technique (weighted decision using successive frames) as well as other sophisticated techniques (such as pattern recognition based on neural networks and a modified version of geometric phase analysis), but we decided not to use these techniques in this work. The main problem with these sophisticated methods is that the programmers' intention (or initial reference dataset) strongly affects the individual identification results. To improve the reliability of this work, therefore, we chose a non-biased and straightforward method (thresholding of maximum peak intensities in FFT images) for the structural identification, although this method cannot prevent a few undefinable frames. The analyzed results indicate (regardless of the undefinable frames) that structural fluctuations occur during the nucleation process.

3. Electron beam effects on the observed nucleation process

4.1 TEM observation of pre-synthesized nanocrystals

The electron beam can transfer a certain amount of energy to Au clusters through elastic and/or inelastic scattering, which may generate transformations of clusters. Therefore, we need controlled imaging experiments showing that the observed structural fluctuations are not an artifact of the e-beam irradiation or other aspect of the experiments. Entire parts of Supplementary section 4 aim to present that this is not the case in our study, and this section (4.1) focuses on showing TEM observations of Au nanoclusters which are not under the nucleation process but in a static condition (no supply of Au atoms, because this sample contains no AuCN). Sub-2 nm Au nanoclusters were prepared by a typical colloidal synthesis (see Supplementary section 1.1) and observed using the identical TEM under the identical conditions (nanoparticles on single-layered graphene were observed at an acceleration voltage of 300 kV and a current density of 7.0×10^6 A/m^2, equivalent to an electron dose-rate of 4.4×10^5 e$^-$/Å^{2}s) for a prolonged time. As shown in fig. S32, we observed 62 pre-synthesized Au nanoclusters whose diameters range from 0.8 nm to 2.7 nm (2D projected areas: 0.5 nm^2 to 6 nm^2). The important point in this experiment is to quantitatively compare the size-dependent stability of crystalline states of nanoparticles during the nucleation process to that in a static condition. We performed the quantitative comparison by measuring the temporal fraction of crystalline states and 2D projected area of nanocrystals. Figure S32C shows that nanoparticles during the nucleation process are more unstable than pre-synthesized nanoclusters. Pre-synthesized nanoclusters mostly stay in the crystalline state throughout the imaging for particle sizes > ~1 nm. Because the two stabilities should be very similar if the e-beam irradiation is the main source for the structural fluctuations, this experimental result supports our claims in the manuscript. This stability difference presumably originates from different surrounding environments of the two kinds of nanoclusters. While there should be almost no Au adatoms near the pre-synthesized nanoclusters, many Au adatoms supplied from the solid precursor (AuCN) appear near the nanoclusters in our system. Interactions between the nanoclusters and adatoms cause the stability difference between the two nanoclusters (as presented in Figs. 3C – 3F), although the two nanoclusters with similar size may have almost identical energy landscapes.

4.2 in-situ TEM under various e-beam conditions

We performed the in-situ TEM imaging under various e-beam conditions (fig. S15) using multiple aberration-corrected TEMs (see Supplementary section 1.2). The lowest current density at which we were able to perform the in-situ TEM observation was 6.6×10^2 A/m^2 at 200 kV, which was ~10^{-5} times of the maximum current density (6.1×10^7 A/m^2 at 200 kV) used in this work. While the temporal resolution (40 ms) and S/N ratio of the low-dose movies were moderately degraded compared to the original observations, the reduced reaction speed under this condition enabled us to properly analyze the in-situ movies. Using a current density lower than this value stopped the decomposition of AuCN to Au atoms and thus no nucleation process could be initiated. Detailed experimental procedures and results (including bright-field TEM and selected area electron diffraction (SAED) analyses) for minimizing the current density in the in-situ TEM imaging are presented in fig. S16.

The D-C fluctuations of Au nanoclusters were consistently observed in all nucleation paths investigated in this work (fig. S15). Figure S29, A and B, shows a typical example observed under our minimum dose, and additional results observed in other conditions indicated in fig. S15 are presented in Fig. 2 and figs. S25 to S28. While the speed of the nucleation and growth process (essentially the supply of Au atoms) was influenced by the e-beam conditions, all of the nucleation processes investigated with various e-beam conditions show identical characteristics: the recurrent structural transformations between disordered and crystalline states were observed during the nucleation process at much lower dose rates and then a stable crystalline structure was formed in the final stage of nucleation. The consistency in this qualitative analysis supports that the observed fluctuations are not an artifact of the e-beam irradiation.

The most noticeable point in the experiments under various electron-beam conditions is the high speed of AuCN decomposition under the accelerating voltage of 80 kV (fig. S30). Because it is well known that radiolytic damage to TEM samples increases as the accelerating voltage is reduced (*43, 44*), this observation is consistent with radiolysis being the major pathway to decompose AuCN to generate Au atoms. This high radiation-sensitivity at 80 kV is one of the major bottlenecks to observe crystal nucleation from the very beginning of the process. The original purpose for imaging at 80 kV was to reduce or minimize possible effects from the electron beam during in-situ observations of the nucleation process, but we found that this condition led to the opposite effect and is not suitable for improving the in-situ TEM image's quality.

We quantitatively compared the low-dose TEM observations of the nucleation process with the original in-situ TEM results, and also compared all of them with control TEM imaging results using pre-synthesized Au nanoclusters. In each case, multiple nanoclusters undergoing the nucleation process or pre-synthesized nanoparticles were analyzed statistically to obtain temporal fractions of the crystalline state depending on the sizes of nanocrystals (Fig. 3A). This graph indicates a size-dependent stability of the crystalline state in Au nanoclusters under certain conditions. In Fig. 3A, the three results observed during the nucleation process (solid symbols) have scattered data points that are overlapped to each other, although the current density is reduced ~1,000 times in the two low-dose TEM results (orange triangles and green squares) compared to the original in-situ TEM data (magenta dots). The fitting curves (dashed lines) indicate that the case of 200 kV and 5.6×10^3 A/m^2 (350 e$^-$/Å^{2}s) have improved stability compared to the other two cases, but the difference is relatively small as seen in large scattering of the data points. On the other hand, the stability difference is clear in pre-synthesized nanoclusters observed at 300 kV and 7.0×10^6 A/m^2 (gray open circles; the imaging condition is identical to the magenta-dot case) compared to the other three cases of the nucleation process. If the e-beam irradiation is a dominant

and direct reason for the dynamic and reversible transformations, the gray-circle and magenta-dot cases should have very similar characteristics. Instead, pre-synthesized nanoparticles mostly stay in the crystalline state throughout the imaging for particle sizes > ~1 nm. Comparing the 200 kV and 80 kV cases that have an identical current density is also informative in showing that the direct energy transfer through elastic scattering of electrons is not a dominant source for the structural transitions. (The stability difference between the two cases is presumably because the radiolysis of AuCN at 80 kV is faster that at 200 kV, as investigated in fig. S30.) Quantitative comparisons based on low-dose TEM imaging and control imaging suggest that the e-beam is not a dominant and direct cause of the dynamic and reversible transitions of Au nanoclusters during the nucleation process.

Another way for the quantitative comparison is to calculate average transition frequencies of Au nanoclusters depending on their sizes for the three different beam conditions (fig. S33). In-situ TEM movies captured at the three different conditions (Figs. 2A to 2C) were frame-averaged to have an identical temporal resolution (40 ms), and then both disordered-to-crystalline and crystalline-to-disordered transition events were counted from the movies (time period: 5 s) to obtain transition frequencies. All three results in fig. S33 show that the transition frequencies are high in the range from ~1.0 to ~3.0 nm^2 while transition events are relatively suppressed in the smaller (< ~1.0 nm^2) and larger (> ~3.0 nm^2) ranges, which coincides well with the above analysis based on Fig. 3A. In addition, the three cases have similar levels of the transition frequencies despite large differences in their current densities (3 orders of magnitude difference). Therefore, fig. S33 also supports that the electron beam is not a dominant reason to generate the structural transition of Au nanoclusters. However, we note that the temporal resolution of our in-situ TEM observations (maximum 1.6 ms in our study and 40 ms in the analysis of fig. S33) may not be high (fast) enough to capture every transition event in the nucleation process. In regard to the temporal fractions (Fig. 3A), as their calculation is relatively robust to observation errors from the limited temporal resolution compared to counting the transition events, we derived the main claims of this study from Fig. 3A.

4.3 in-situ TEM of the nucleation process with periodic switching off the e-beam

As an additional control experiment, we observed the nucleation process using high-speed in-situ TEM with periodic switching off of the e-beam. The process that occurs during the period the e-beam is blanked cannot be captured, but we were able to compare the structural states of an Au nanocluster right before and after the blanking periods. Figure S34, A to C, illustrates a typical example of the experimental results, and fig. S34D summarizes changes of the structural states before and after the beam blanking observed in the 22 cases of e-beam blanking. If the e-beam irradiation mainly induces the structural fluctuations of Au nanoclusters, the most plausible model for the process would be that the e-beam drives crystalline-to-disordered transitions and the energy dissipation drives disordered-to-crystalline transitions. Then, it is expected that the disordered-to-crystalline transitions are most likely to occur through the blanking period, because the system can relax back to a crystalline state. The result in fig. S34D shows that this is not the case. Most of nanoclusters maintained their structural states (17 cases), while disordered-to-crystalline and crystalline-to-disordered transitions were observed in 3 and 2 cases, respectively. This phenomenon is reasonable because adatom generation from AuCN was suppressed during the periods without the e-beam irradiation.

4.4 Energy transfer from irradiated electrons to nanoclusters

This paragraph aims to examine whether or not the energy transfer pathways from electrons to inorganic materials can generate structural fluctuations that have the observed characteristics. Our study provides experimental findings opposite to the assumption that the e-beam irradiation primarily drives the observed structural fluctuations in Au nanoclusters. Under this assumption, a typical movie such as Fig. 2D indicates that the stable dose delivered to a nanocluster by the e-beam drives it back and forth between disordered and crystalline states. This analysis can already surprise one who imagines that nanoparticles would prefer one structure if the applied electron dose is stable. Figure 2D also demonstrates that, under the constant flux of the e-beam, two neighboring nanoclusters with similar sizes show structural fluctuations that are not synchronized. These two observations from Fig. 2D underline that structural fluctuations during the nucleation process have a stochastic nature. It is well known that scattering events of individual electrons occur stochastically under the e-beam irradiation and each event (regardless of elastic / inelastic scattering) transfers energy to the specimen.

Therefore, we need to examine whether or not stochastic energy deposition produced by electron scattering can induce the observed structural fluctuations. If this were to be true, we should expect the time scale and/or magnitude of the fluctuations to be strongly dependent on the electron irradiation conditions, i.e., the accelerating voltage and current density. However, counterevidence is shown from the comparison between Figs. 2D and 2E, which have 4 orders of magnitude difference in current density during the imaging. Because current density is linearly proportional to the number of total electrons in the e-beam as well as the number of scattering events of electrons (*44*), one can expect that the driving force of structural fluctuations (stochastic electron scattering) should be strongly suppressed in the case of Fig. 2E compared to the case of Fig. 2D, and thus also expect that the crystalline state should be maintained (without any disordered state) in the nanoclusters 3 and 4 whose sizes are similar to those of the nanoclusters 1 and 2. However, the two cases show similar behaviors, which support the interpretation that the dynamic and reversible transformations are not primarily driven or modified by the e-beam. Steady-state local heating, one of representative effects produced by the e-beam, is less worrisome for the conclusions of the present work. It is because local heating (temporally uniform on the millisecond scale of the measurements) is marginal (only a few degrees) for inorganic samples imaged on a highly conductive material like graphene.

4.5 E-beam induced phenomena: Au adatom diffusion and D-to-C transitions of nanomaterials

Possible concerns about the electron beam effect could be not only that the beam directly transfers energy into Au clusters to transform them from crystalline to disordered states, but also that adatom diffusion promoted by the beam may induce the transformations to Au clusters. This possibility could be supported by the previously investigated systems where the e-beam induced crystallization from amorphous materials, whose states are largely changed by atomic diffusion induced by the e-beam. Our discussion on this matter is as follows.

E-beam induced motions of metal atoms on a surface during TEM imaging have been thoroughly investigated by Egerton (*43-45*), and he concluded that, compared to e-beam induced motion, thermal motion predominates for Au atoms absorbed onto graphene at room temperature in conventional TEM imaging (*43*). In detail, the adatom displacement rate generated by the 200 keV e-beam with a current density of 10^9 A/m^2 (~10 times higher than the maximum current density of our observation) is orders of magnitude smaller than the thermal displacement rate at room temperature, when the activation energy for surface diffusion, E_{sd}, is smaller than ~0.5 eV

(E_{sd} for Au adatoms on graphene has been previously estimated as 0.007 eV (*43*)). This analysis means that thermal diffusion of Au atoms on graphene is predominantly large and the addition of e-beam induced diffusion does not induce a significant change to our system. The large thermal diffusion of Au atoms on graphene can be also confirmed by another previous work (*46*), which observed sub-monolayer deposition of metals on graphene using ex-situ STM. Sub-monolayer deposition (0.25 monolayer) of Au on graphene at room temperature does not form scattered Au atoms on the graphene surface but forms relatively large Au clusters (~4 nm in diameter) due to high thermal diffusion of Au adatoms. Lowering the deposition temperature to 90 K resulted in moderately scattered Au atoms on graphene but increasing the temperature to 220 K after the deposition at 80 K changes the sample to relatively large Au clusters, which means that thermal diffusion of Au adatoms at 220 K is already significant. Therefore, it is hard to say that e-beam induced diffusion of Au adatoms significantly changes our system observed at room temperature.

Since our system belongs to e-beam induced crystallization (reviewed in (*47-49*)), comparing our system to other e-beam induced reactions can be valuable to understand its characteristics. The e-beam induced crystallization can be classified as two types depending on the initial form of monomers (atoms). In the first type, the chemical form of monomers in the initial state is the same as that in final crystals. A typical example is e-beam induced crystallization in an amorphous film. In this example, zerovalent atoms have disordered arrangements and low mobility in the initial amorphous film, and then atomic diffusion promoted by the e-beam enables atoms to find ordered positions in a crystalline structure. Therefore, the e-beam is strongly involved to the transformation process from disordered monomers to a crystalline structure in this type of crystallization. In the second type, monomers initially have different chemical forms such as ions or compounds, and the e-beam induces chemical changes (such as reduction) into these materials to generate monomers. Once the monomers (such as zerovalent metal atoms) are produced by the e-beam, the monomers spontaneously form crystals to minimize the surface energy mainly driven by their high mobility even without the e-beam. Therefore, except for the initial stage where the precursors are transformed to monomers, the e-beam is not strongly involved in the following crystallization process. Our system is similar to this, because Au atoms are produced by radiolysis of AuCN and the mobility of Au atoms on graphene is significantly high without the e-beam (as discussed in the previous paragraph). Au adatom diffusion that initiates crystal nucleation in our system originates mostly from thermal energy and not from the e-beam, thus we expect that the e-beam effect on the observed nucleation process is minor.

4. Energy calculation of binding reactions and phase transitions in Au nanocrystals

5.1 Calculation of the binding energies between the model Au_n nanocrystals and an Au atom

We calculated the binding energies between the model Au_n nanocrystals (n = 19, 26, 37, 49, 58, 69) and an Au atom by density functional theory calculations. For each nanocrystal, we calculated the corresponding binding energy by

$$(\text{binding energy of } Au_n + Au) = E(Au_{n+1}/G) - E(Au_n/G) - E(Au/G) + E(G),$$

where E denotes the total energy, and G denotes the supporting graphene layer. We performed all the simulations under periodic boundary conditions, and the system structures were prepared and optimized as follows.

To prepare stable initial structures of the dome-shaped nanocrystals, we selected FCC Au nanocrystals having the global minimum total energies searched by Schebarchov *et al.* (*50*) and bisected them to make dome-shaped fragments. The chosen source nanocrystals were Au_{39}, Au_{54}, Au_{79}, and Au_{89}, from which the model Au_{19}, Au_{26}, Au_{49}, and Au_{58} were generated. The bisection was done through the middle (111) plane of each source crystal, leaving two or three (111) layers to form a dome shape. The Au_{37} model was generated in the same way, except that the source nanocrystal was a cuboctahedron Au_{55}. The source nanocrystal of the Au_{69} model was an FCC Au_{109} nanocrystal, which we derived from a cuboctahedron Au_{147} by cutting out a few facets.

For the geometry optimization of Au_n/G systems, we prepared a single-layer-graphene supercell and laid each Au_n model in the middle of the graphene layer. The base (111) layer of the nanocrystals was in contact with the graphene layer, with a gap of ~0.25 nm between the nanocrystal bottom and the graphene. The graphene supercell size was 9x9 for Au_{19}, 12x12 for Au_{26}, Au_{37}, and Au_{49}, and 14x14 for Au_{58} and Au_{69}. These sizes allowed the nanocrystals in repeated unit cells to be apart from one another by ~1.5 nm (note that a "unit cell" here means a simulation cell composed of a graphene supercell and a laid nanocrystal). The height of the unit cell was 2.5 nm for Au_{19} and 3.0 nm for the others, making ~2.0 nm vacuum above the nanocrystals. When positioning a nanocrystal on the graphene plane, we first positioned the nanocrystal to the center of the graphene plane and made a few translations (to put the center of the nanocrystal above a carbon atom or a carbon-ring center) and/or rotations (to make the top view of the nanocrystal and the underlying carbon atoms eclipsed or staggered) of the nanocrystal to prepare a maximum of four candidate positions. Then we fully optimized the prepared initial geometries. From the optimized geometries, we picked the most stable one for each n and obtained $E(Au_n/G)$. The picked structures were then used in the following Au_{n+1}/G simulations. For Au_{69}/G, we obtained one optimized geometry owing to the high load of computation. As an example, we depicted the optimized geometry of Au_{37}/G in the left part of fig. S36.

Given a structure of Au_n/G, an additional Au atom can bind to various sites on the nanocrystal surface, each of which results in a candidate initial geometry of Au_{n+1}/G. To sample the most probable cases needed in estimating the binding energy, we made the following two assumptions. First, because a new Au atom, once generated from the AuCN wire, will propagate on the graphene surface before encountering a nanocrystal, we assumed the possible binding sites to be confined to the edge of the lowest layer of the nanocrystal. On such sites, the new atom becomes bound to the graphene surface as well as the nanocrystal edge. Second, because a new atom will stabilize itself by maximizing its coordination to the nanocrystal atoms, we only chose the sites where the new atom can contact two neighboring atoms in the nanocrystal edge simultaneously. One example of such binding modes satisfying the two assumptions is depicted in the middle part of fig. S36. Consequently, the number of binding sites, i.e., the initial geometries of Au_{n+1}/G, ranged from 2 to 13 depending on the nanocrystal's symmetry (fig. S37). All the initial geometries were then optimized, giving a set of $E(Au_{n+1}/G)$ for each n. These different energy values were the source of the error bars in Fig. 3C. Note that when optimizing the Au_{n+1}/G geometries, we froze the previously optimized Au_n nanocrystal part and only relaxed the new Au atom and the graphene layer. This was to prevent overestimation of the binding energy: if the An_{n+1} part is fully relaxed, the structure can get severely distorted (following the optimization process), resulting in an unnecessarily lower $E(Au_{n+1}/G)$ value.

Finally, we obtained E(G) by simulating a bare graphene layer with the previously set supercell settings. For Au/G, we placed an Au atom ~0.25 nm above a carbon atom and optimized the geometry. This gave a lower E(Au/G) than the one where the Au atom was placed above the

center of a carbon ring. We depicted in the right part of fig. S36 the optimized geometry of Au/G for the case of 12x12 graphene. Inserting the obtained energies into the above equation gave the binding energies, as listed in Table S1.

For all the calculations we used the periodic calculation module BAND (*51*) in the Amsterdam Density Functional (ADF) program (*52*) (revision r70630 of release 2018.105). We performed spin-polarized calculations using the double-zeta basis sets and the Perdew-Burke-Ernzerhof (PBE) exchange-correlation functional (*53*) for the geometry optimizations, and using the triple-zeta plus polarization basis sets, the PBE functional, and Grimme *et al.*'s dispersion correction with Becke–Johnson damping (D3(BJ)) (*54*) for the final single-point calculations. The zeroth-order regular approximation was applied for scalar relativistic effects (*55, 56*). The frozen core approximation was applied up to 1s for carbon atoms and 4f for gold atoms. The overall numerical quality was set to the normal level of the program, and only the gamma point was set for the periodic calculations. Note that ADF normally calculates the total bonding energy of atomic fragments, not the total energy; the above expression of the binding energy still holds but E should be understood as the total bonding energy instead.

5.2 Calculation of the energies required to reach the melting points

To calculate the melting temperature of a metal nanocrystal, we need to estimate its surface-to-volume ratio (*30*). The surface-to-volume ratio is determined by the size and shape of the nanocrystal, causing the particle size and shape dependence of the melting temperature. In estimating the surface-to-volume ratios of our Au_{n+1} nanocrystals, we approximated our dome-shaped models as having a hemispherical shape. A more detailed characterization of the nanocrystals' shapes is possible, and this will lower the calculated melting temperatures. However, our purpose is to provide an upper bound of the melting temperature of each Au_{n+1}, without bearing the arbitrariness in characterizing the morphology of a 1–2 nm-sized particle. Note that the bottom surfaces of our nanocrystals are covered by graphene support. A hemisphere whose cap area is its only surface has the same surface-to-volume ratio (6/diameter) as that of a sphere of the same diameter. In this regard, we approximated each of the source nanocrystals Au_{39}, Au_{54}, Au_{55}, Au_{79}, Au_{89}, and Au_{109}, which we used in generating the Au_n models, as a spherical particle and regarded the resulting diameter as the diameter of the corresponding Au_{n+1}. The hypothesized spherical particle was such that it has the same volume as that of the original source nanocrystal. Here we used the fact that the source nanocrystals are mostly symmetric and ball-shaped. Also, we assumed that the surface-to-volume ratio of an Au_{n+1} nanocrystal can be approximated by the surface-to-volume ratio of Au_n. For the volumes of the source nanocrystals, we first prepared an atomic model of each source nanocrystal, where the constituent atomic spheres had the radius of half the average Au–Au bond length of the nanocrystal. Then we computed a convex hull enclosing the atomic model and obtained the hull's volume, which we regarded as the volume of the source nanocrystal.

Table S2 lists the calculated diameters, which we used in applying the size-dependent melting temperature expressions in (*29-31*). Table S2 also lists the obtained melting temperatures and specifies the equations and parameters we used in the calculations.

To calculate the energies required to reach the melting temperatures, we needed to obtain the heat capacities of the Au_{n+1} nanocrystals. Assuming the independence of the heat capacity on particle shape, we isolated the Au_{n+1} part from one of the optimized Au_{n+1}/G geometries and then fully relaxed the isolated nanocrystal in gas phase to obtain the harmonic vibrational frequencies. From the frequencies, we can compute the temperature-dependent constant-volume vibrational heat capacity, which we used to approximate the constant-pressure vibrational heat capacity $C(T)$

of the nanocrystal. Then, the energy required for the nanocrystal in temperature T_0 to reach its melting temperature T_{melt} can be calculated as (*57*):

$$\int_{T_0}^{T_{\mathrm{melt}}} C(T)\mathrm{d}T = \sum_j h\nu_j \left(\frac{1}{e^{h\nu_j/k_{\mathrm{B}}T_{\mathrm{melt}}} - 1} - \frac{1}{e^{h\nu_j/k_{\mathrm{B}}T_0} - 1}\right),$$

where ν_j are the vibrational frequencies, h the Planck constant, and k_{B} the Boltzmann constant.

We assumed 300 K for the initial temperature T_0. The calculated energies are listed in Table S3; different estimations of T_{melt} resulted in different values of energy for each Au_{n+1}. For the gas-phase Au_{n+1} simulations, we used the ADF program with the same setup as described above. We used the triple-zeta plus polarization basis sets and the PBE-D3(BJ) functional for the geometry optimizations. All the nanocrystals were set to neutral, and we always set the lowest spin multiplicity, i.e., singlet or doublet, depending on n.

5. Comparison of the observed model system to other cases of atomic crystallization

The nucleation process in this study starts from concentrated adatoms released from the solid precursor (AuCN nanoribbons), while crystal nucleation generally starts from free atoms in the vapor/liquid phase or adatoms scattered on a surface. We do not claim that our system universally reproduces the entire scope of crystal nucleation, but our study addresses a critical step that determines the nucleation pathway in many different types of crystallization processes. Regardless of the method that initiates the crystallization process, the nucleation is followed by concentrating monomers over a certain level in a local region. In this high atomic density state, nuclei are generated and grow to a larger size by continuous monomer flux. The model system we used in this study reproduces this early stage that satisfies monomer conditions for nucleation to occur. The initial atomic density and characteristics in general systems can be checked from previous investigations of the metal deposition process. The most relevant study is in-situ observations of Au sputter deposition on silicon using synchrotron-based SAXS (small-angle X-ray scattering) (*58*). Both this and our system are for heterogeneous Au growth in the Volmer-Weber mode (both silicon and graphene have low affinity to Au). In the nucleation stage of the Au sputter deposition, Au nuclei with an average diameter of 0.9 nm and a mean distance of 3 nm are detected, which means that more than 1.5 Au atoms exist in a 1 nm^2 area in the early stage of nucleation. Our system also shows Au nuclei (nascent nanoclusters) with similar characteristics (an average diameter of ~1 nm and a mean distance of ~4 nm), and the initial atomic density in our system (which can be estimated from the Au fraction and the decomposition rate in/of AuCN) can be similar to that of the sputter deposition case. Therefore, our model system can reproduce nucleation dynamics after the concentration process of atoms generally observed in many systems. As shown in our results, the major experimental finding of this study is based on the in-situ observation of the event that occurs after the formation of the first nanocrystal. For example, the nucleation process presented in Fig. 1 shows the formation of the first nanocrystal at 150 ms, and after that time the reversible and dynamic structural transformations are observed before the formation of a stable nanocrystal at 5030 ms (the end of the nucleation process). Therefore, the main finding of this study (the reversible and dynamic transformations) can explain the important step in general cases of crystal nucleation such as the early stages of thin-film deposition.

It is important to examine whether such structural fluctuations can occur generally during the early stage of diverse crystallizations. In atomic crystallization, roughly assuming initial nuclei are

in a size of ~1 nm, melting temperature of them significantly decreases (for example, lower than ~500 K for gold nanoparticles with a size of ~1 nm was estimated (*29-31*) and 473 K for aluminum nanoparticles with a size of 2 nm was measured (*59*)) and can be comparable to the temperature set by the reaction condition. For example, substrate temperature generally ranges from ~500 K to ~800 K in the thin-film deposition process, and high solvent temperature above ~500 K is typically used in colloidal nanoparticle synthesis (*60*). This fact indicates that a non-crystalline phase (even a molten phase) for small nuclei is not a surprising state in many types of crystallization. Then, the growth of nuclei increases their melting temperature (fig. S44B), thus the nuclei change their state to a crystalline phase at some point of the early-stage growth (fig. S44C). Most importantly, it was theoretically (*61, 62*) and experimentally (*63*) confirmed that, when the size of a nanomaterial is in a regime where thermal energy is comparable to the energy barrier for phase transformation (for example, in a small nanocrystal (*63*)), fluctuations between two phases occur at the transition point. Therefore, it is logically true that structural fluctuations between disordered (molten) and crystalline states can appear in many cases of crystal formation (fig. S44D). In actual processes of crystallization, the phase transition through structural fluctuations would be strongly coupled to the nucleus formation through the aggregation of atoms, because size regimes of the two phenomena are similar.

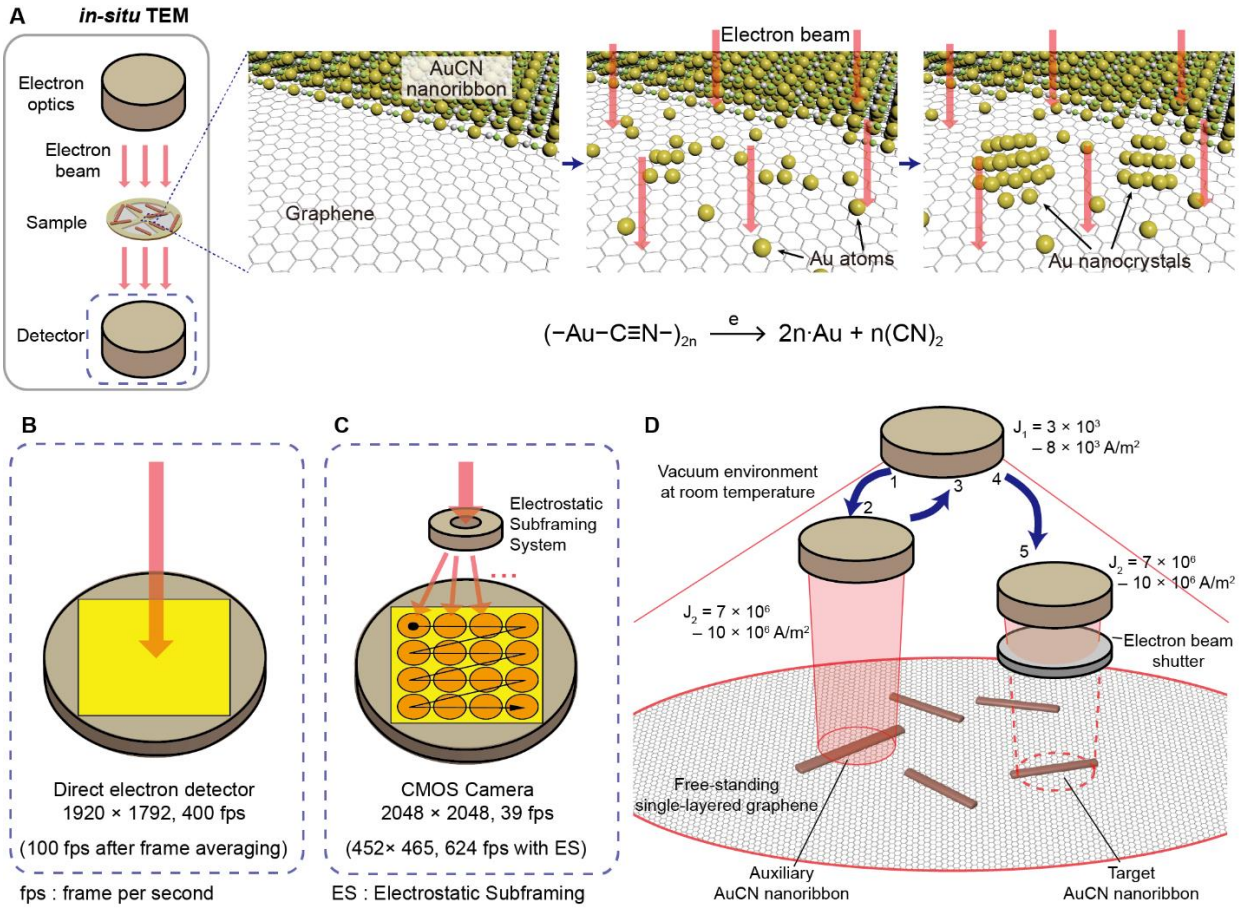

Fig. S1. The concept for capturing early-stage nucleation and growth process of gold nanoparticles. (**A**) Schematics to describe the concept: The electron beam for TEM imaging acts as a reducing agent to decompose the AuCN nanoribbons to zerovalent Au atoms and $(CN)_2$ gas. Then, the density of Au adatoms increases locally near the imaged nanoribbon, and the adatoms aggregate to form Au nanocrystals. These sequential events were captured by three types of electron microscopes, and two of them are described here: 1. TEAM I, an HRTEM with a double aberration corrector and (**B**) Gatan K2 IS direct electron detector, 2. ThemIS with an image aberration corrector and (**C**) high-speed Ceta 2 camera. ThemIS has an added electrostatic beam deflector to deflect the image to 16 different subframes on the camera in sequence during each camera frame, allowing a 16:1 tradeoff of frame rate against pixel count. As a result, the lateral and temporal resolution of the images used in this work were 1920 × 1792 and 10 ms for TEAM I, 452 × 465 and ~1.6 ms for the ThemIS. We also devised (**D**) a method to minimize the electron dose to the AuCN nanoribbon before the observation: (1) Searching for the AuCN nanoribbon under low current density (J_1). (2) Focusing on auxiliary AuCN after beam convergence (corresponding current density: J_2) and saving parameters including focus, beam convergence, etc. (3) Dispersing the electron beam, placing the target AuCN to the center of the electron beam. (4) Closing the shutter and loading the parameters to recover the high-current-density focused image condition, and (5) Opening the shutter and starting observation. The current density values are shown in the figure.

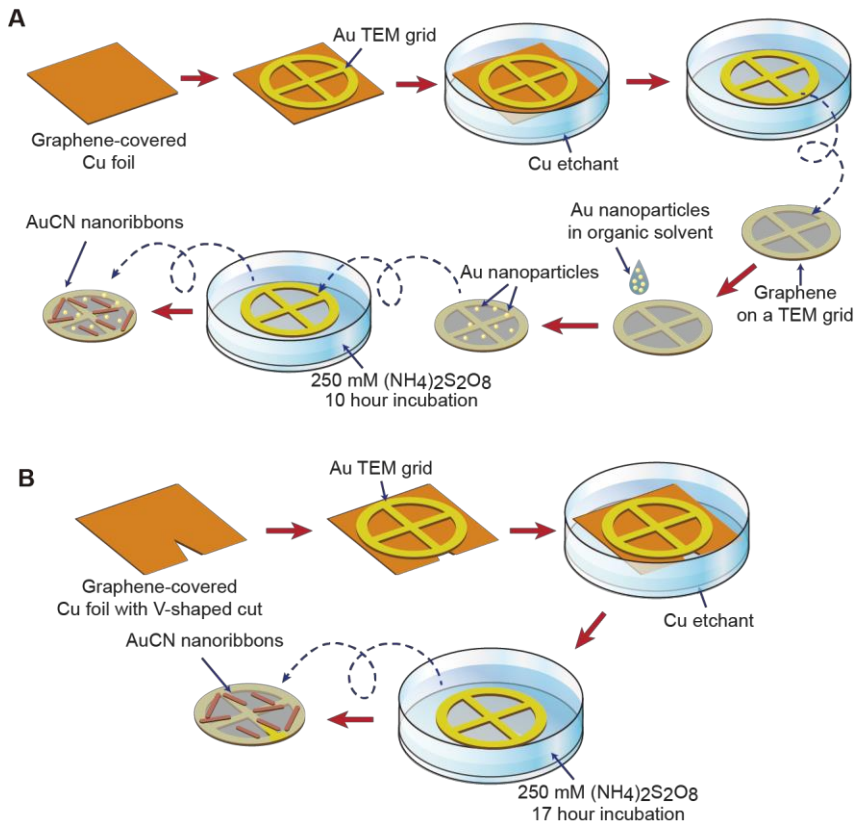

Fig. S2. Preparation of the AuCN nanoribbon for in-situ TEM observation. AuCN nanoribbons are synthesized by putting gold precursors and graphene together in an ammonium persulfate solution. Either (**A**) Au nanoparticles or (**B**) TEM grid mesh made of gold can be used for the gold precursor.

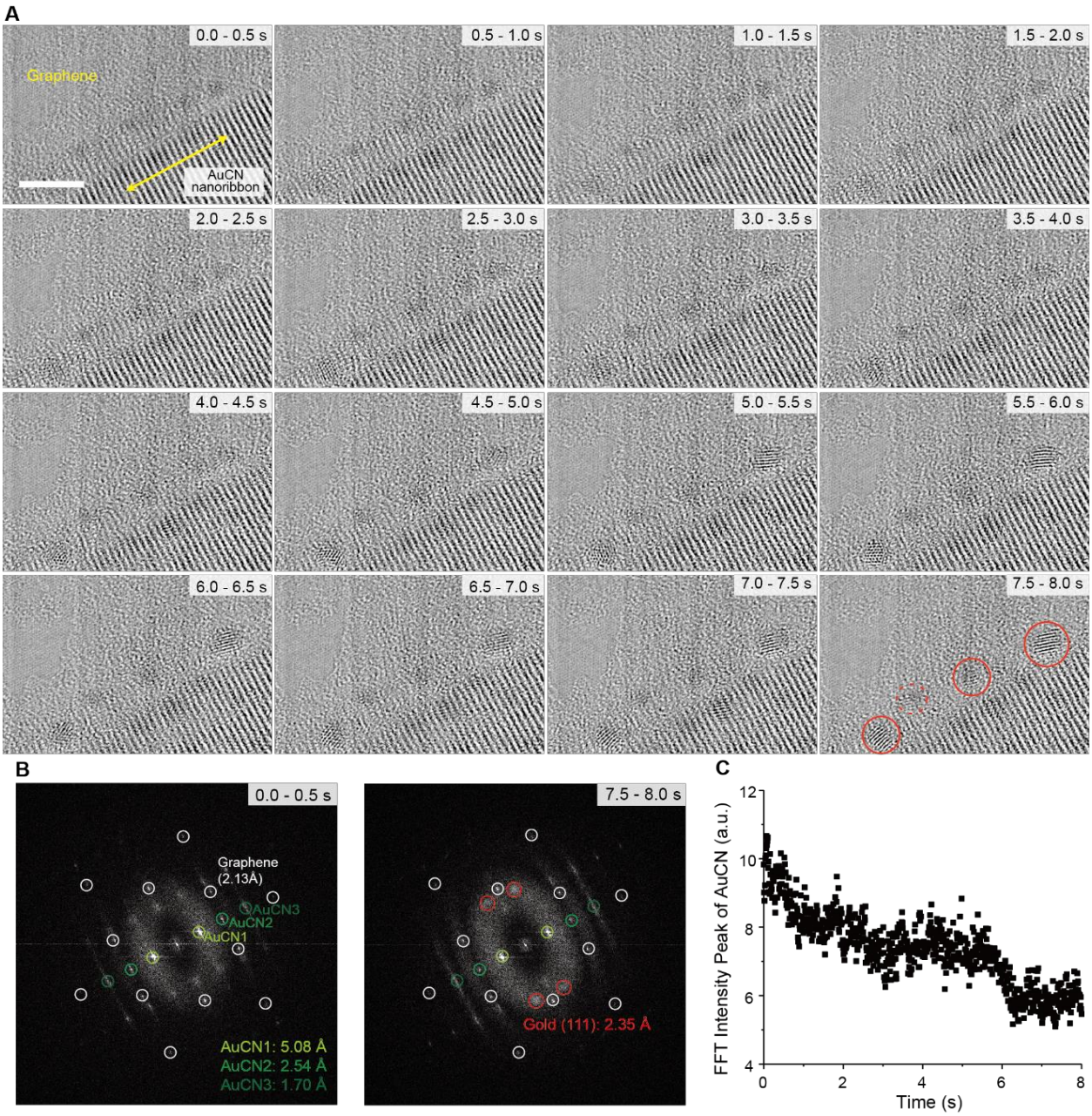

Fig. S3. General characteristics of the nucleation sites shown in Fig. 1A. (**A**) Snapshots of the in-situ TEM movie with deliberately reduced temporal resolution (effective temporal resolution of 0.5 s). Au nanocrystals in the final image are marked with red circles. Scale bar: 5nm. (**B**) Fourier transformed images of the nucleation sites. Together with the diffraction made from graphene and AuCN nanoribbon which is also shown in the first frame (left), cloudy peaks of gold nanoparticles have emerged in the last frame (right) (**C**) Decrease of FFT intensity peak of the AuCN nanoribbon showing the decomposition of the nanoribbon.

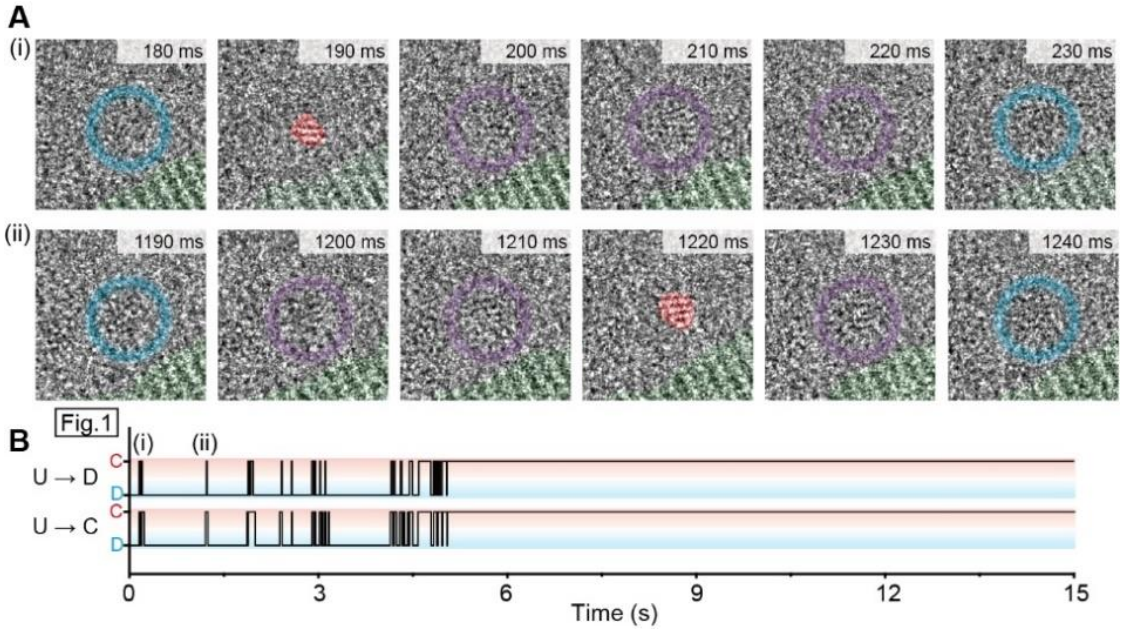

Fig. S4. Undefinable (U) states in the nucleation path in Fig. 1. (**A**) Individual frames near the peaks (i) and (ii). Scale bar: 1 nm. (**B**) Trajectories of structural transitions in the nucleation path (Fig. 1). In the upper and lower trajectories, all undefinable frames (38 out of 1,500 frames) are assigned as disordered (D) and crystalline (C) states, respectively.

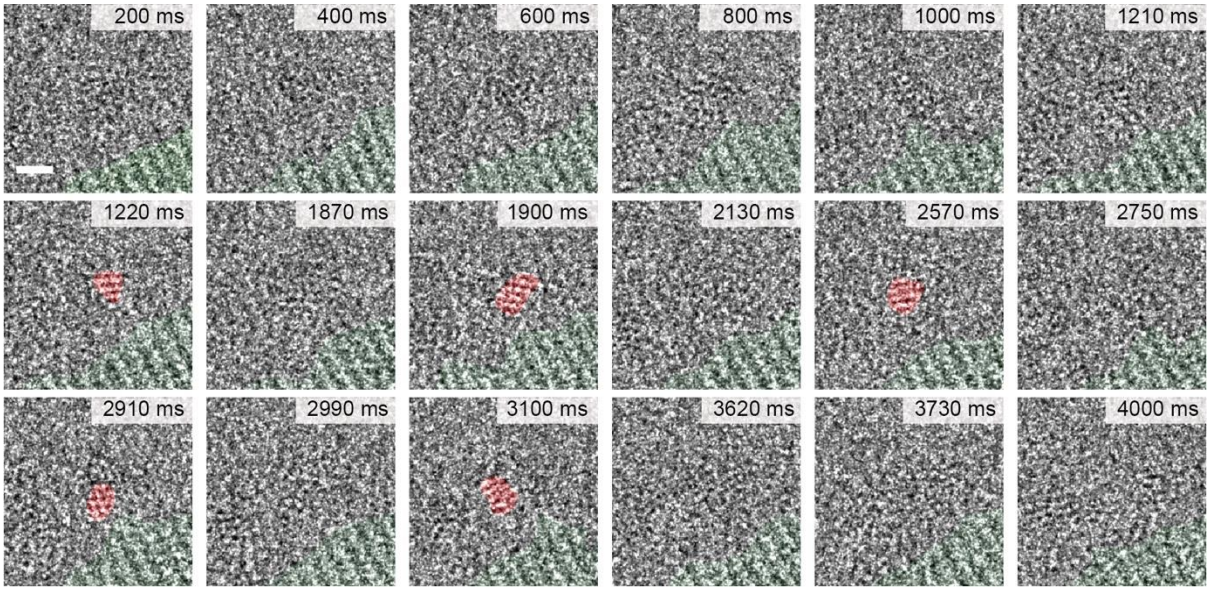

Fig. S5. Supplementary frames of the nucleation site shown in Fig. 1B. After the two transient appearances (160 ms and 190 ms in Fig. 1B), lattice fringes did not appear from 230 ms to 1190 ms. After this, the appearance and disappearance of the lattice fringes were repeated about ten times. Scale bar: 1 nm.

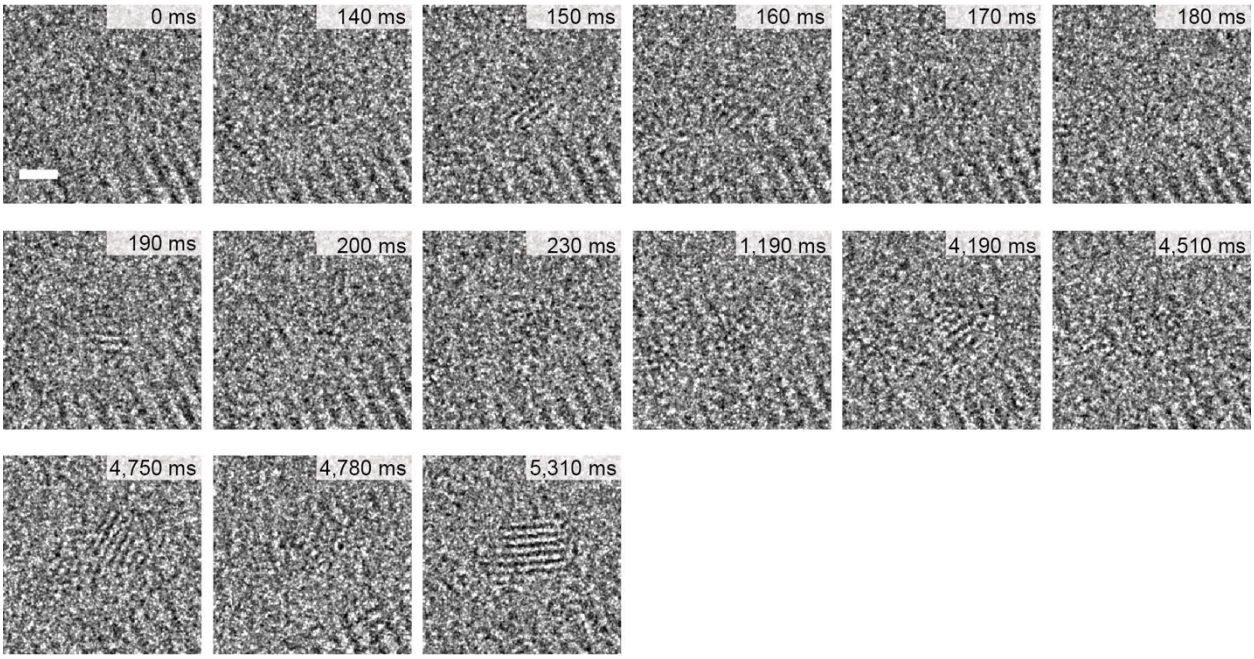

Fig. S6. The uncolored version of the in-situ TEM images of the nucleation site #1 (Images in Fig. 1B). The lattice fringes (in 150 ms, 160 ms, 190 ms, 4190 ms, 4750 ms, and 5310 ms) are also observable from the uncolored snapshots of in-situ TEM movies. Scale bar: 1 nm.

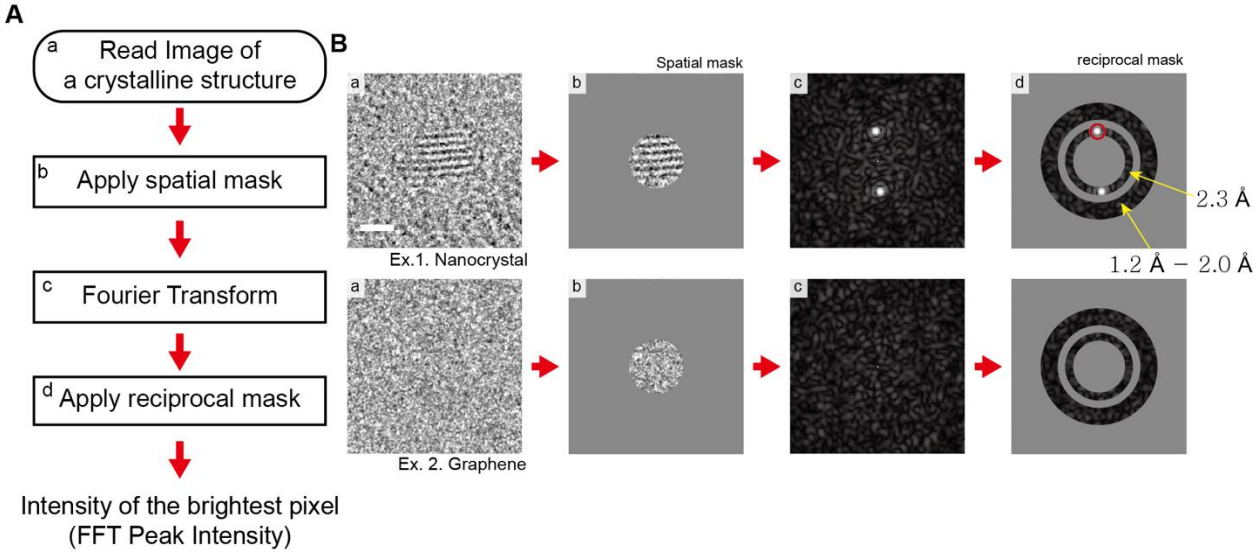

Fig. S7. Method for the calculation of the FFT intensity peak from a TEM image. (**A**) Flow chart. (**B**) Examples using a nanocrystal image (experiment group) and graphene image (control group). After reading an image, it is cropped with a circular mask of 40 pixels (0.8 nm) in radius to remove noise around the particle. After that, the image is Fourier transformed, and a reciprocal mask is applied to select peaks corresponding to the gold nanoparticles. Finally, intensity of the brightest pixel is recorded. The analogous process is applied to other frames to generate the plot shown in Fig. 1C. Scale bar: 1nm.

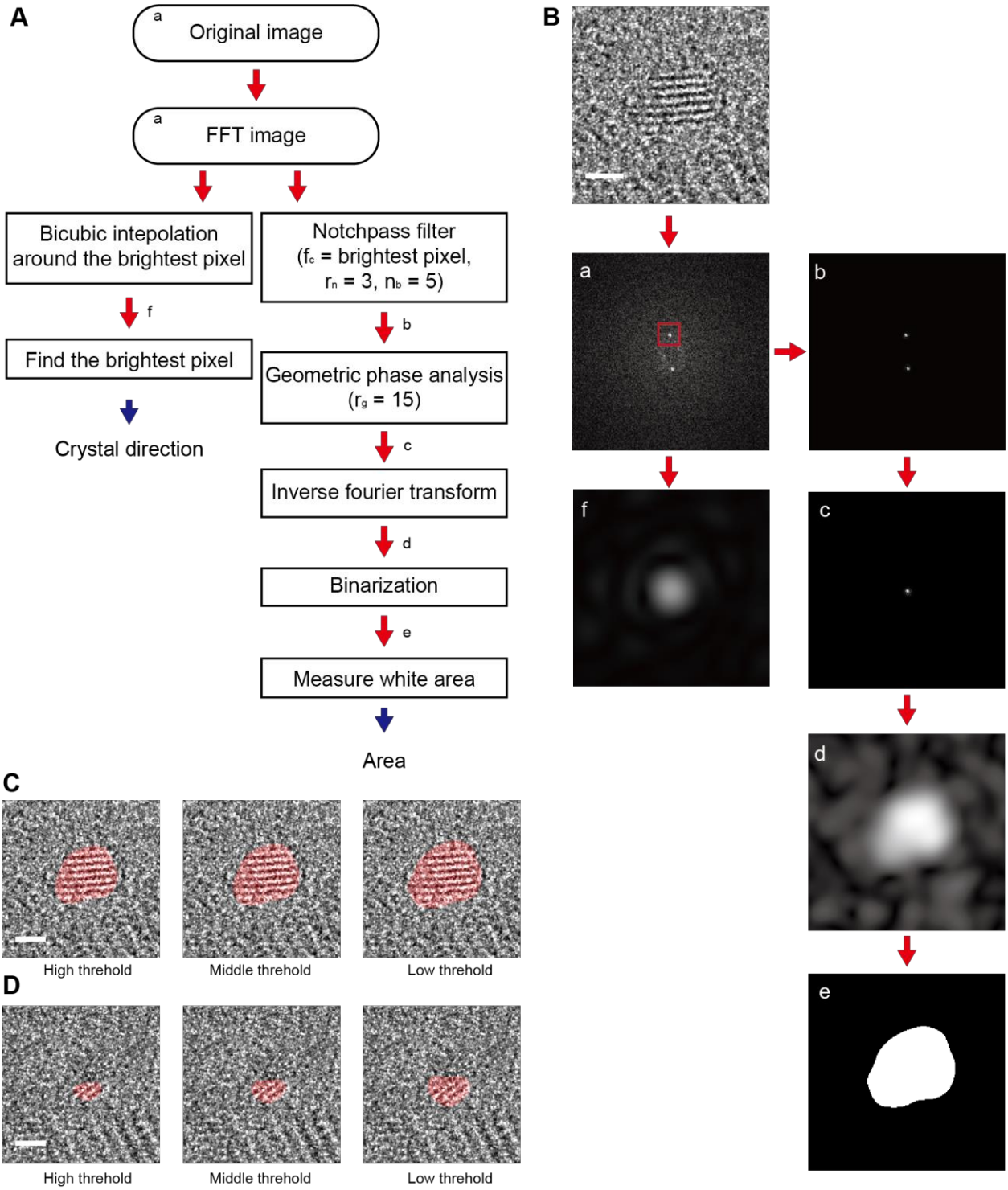

Fig. S8. Method for defining the area and the crystal direction of a nanocrystal. (**A**) Flow chart (**B**) An example of the calculation. (**C**, **D**) Areal change depending on the threshold value for the binarization. The area of the nanocrystal was defined by applying geometric phase analysis to deduce the area corresponds to the selected FFT intensity peak. A crystal direction of a nanocrystal is measured from the angle of the FFT intensity peak. Scale bars: 1nm.

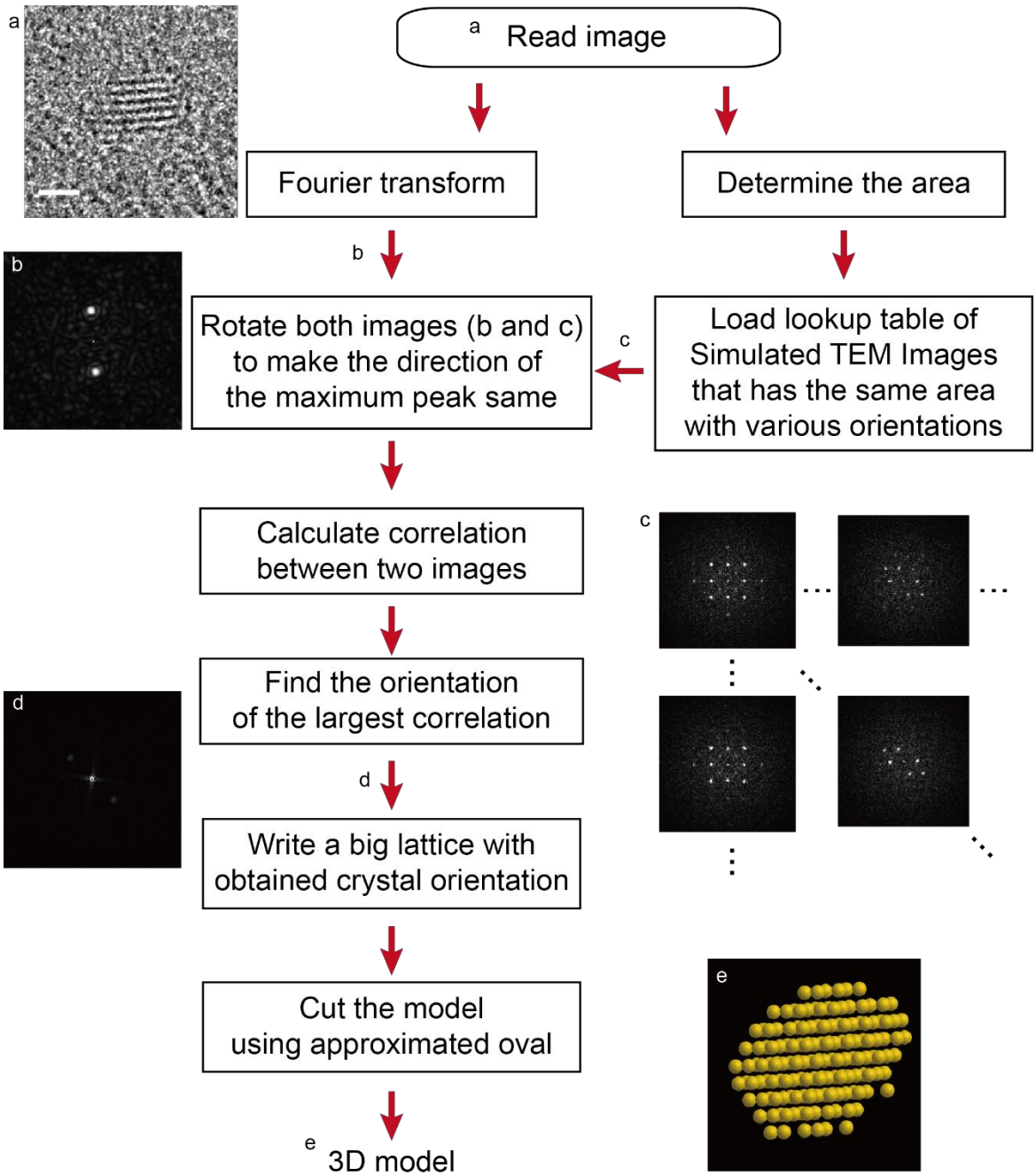

Fig. S9. Method for drawing a 3D model of a nanocrystal image. The flow chart and exemplary images are shown here. The 3D model is drawn by simulating reciprocal images of a nanocrystal in various orientation and finding the most correlated one with the target image. Scale bar: 1nm.

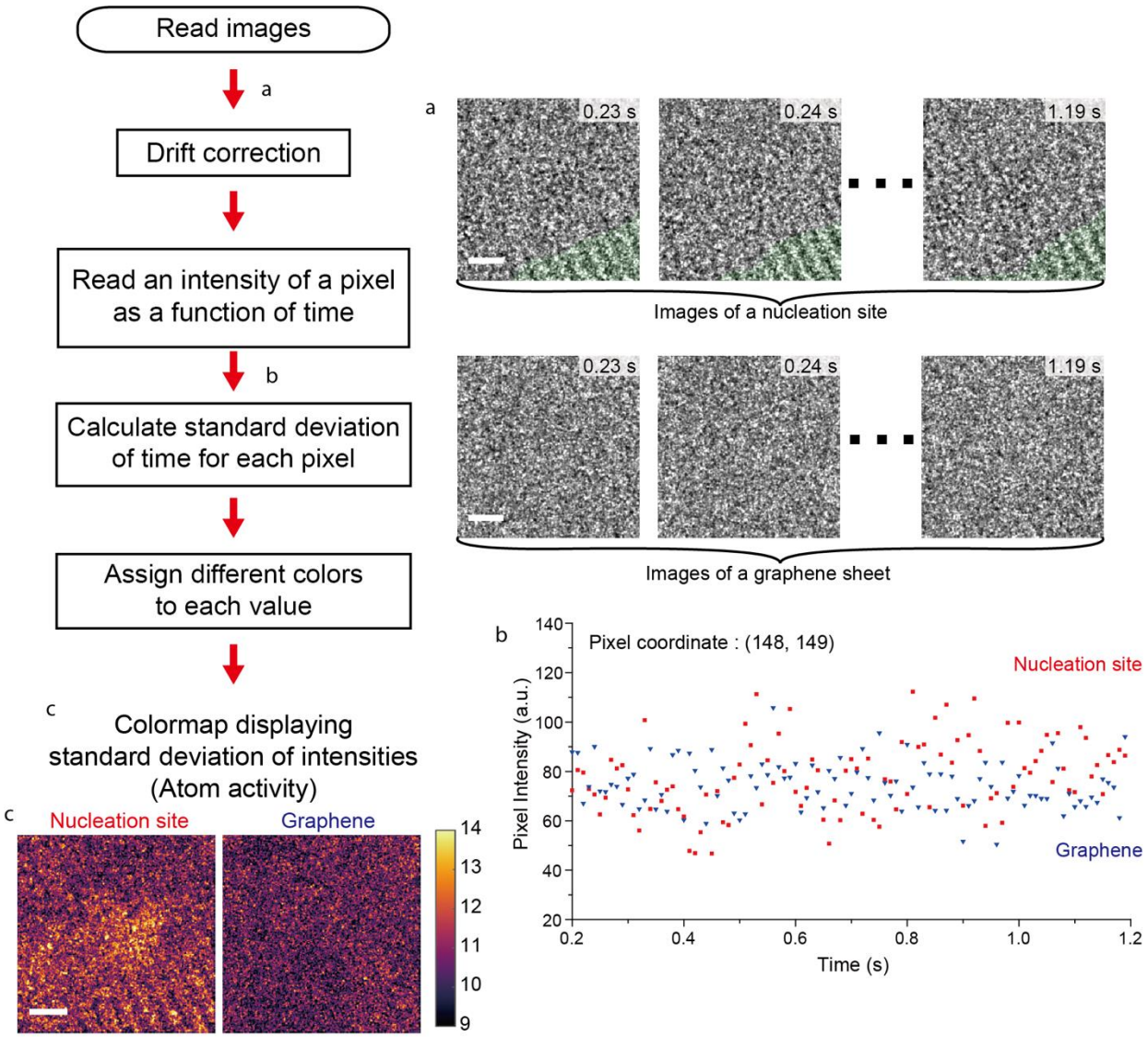

Fig. S10. Method for visualization of the dynamics of the gold atoms. The dynamics of the gold atoms are expected to correlate with the standard deviation of the intensity at the corresponding pixel. (a) Images from 0.23 to 1.19 s show no lattice fringes. (b) For each pixel, the intensity is recorded over the entire set of frames (from 0.23 to 1.19 s), and the standard deviation of these points is calculated. (c) Identical analyses are conducted for every pixel for the resultant standard deviation mapping. Meanwhile, the erroneous intensity deviation from the drift is removed before the analysis by drift correction. The left image in (c) is presented in Fig. 1D. Scale bars: 1nm.

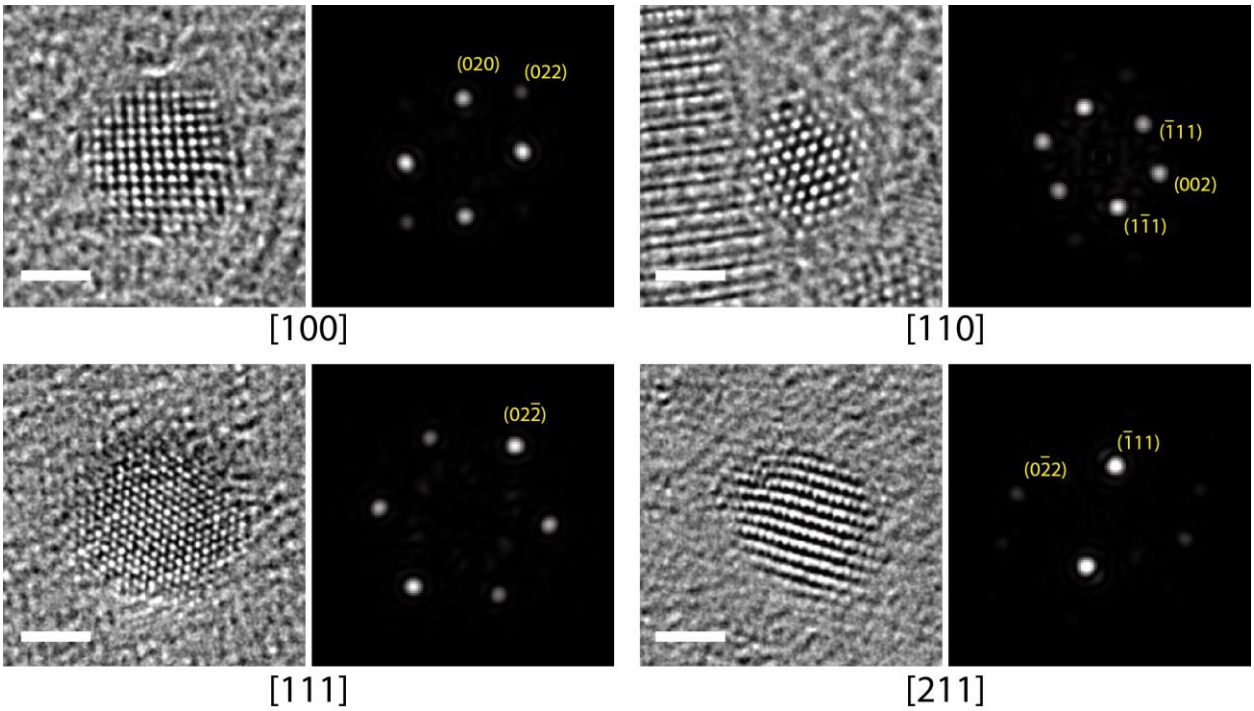

Fig. S11. TEM images of the gold nanoparticles in the later stage of growth. Nanoparticles observed in this study have various appearances depending in part on their orientation, but all crystalline particles appear consistent with the standard gold FCC structure. (Twin boundaries appear sometimes in the FCC-structured nanoparticles.) Scale bars: 1 nm.

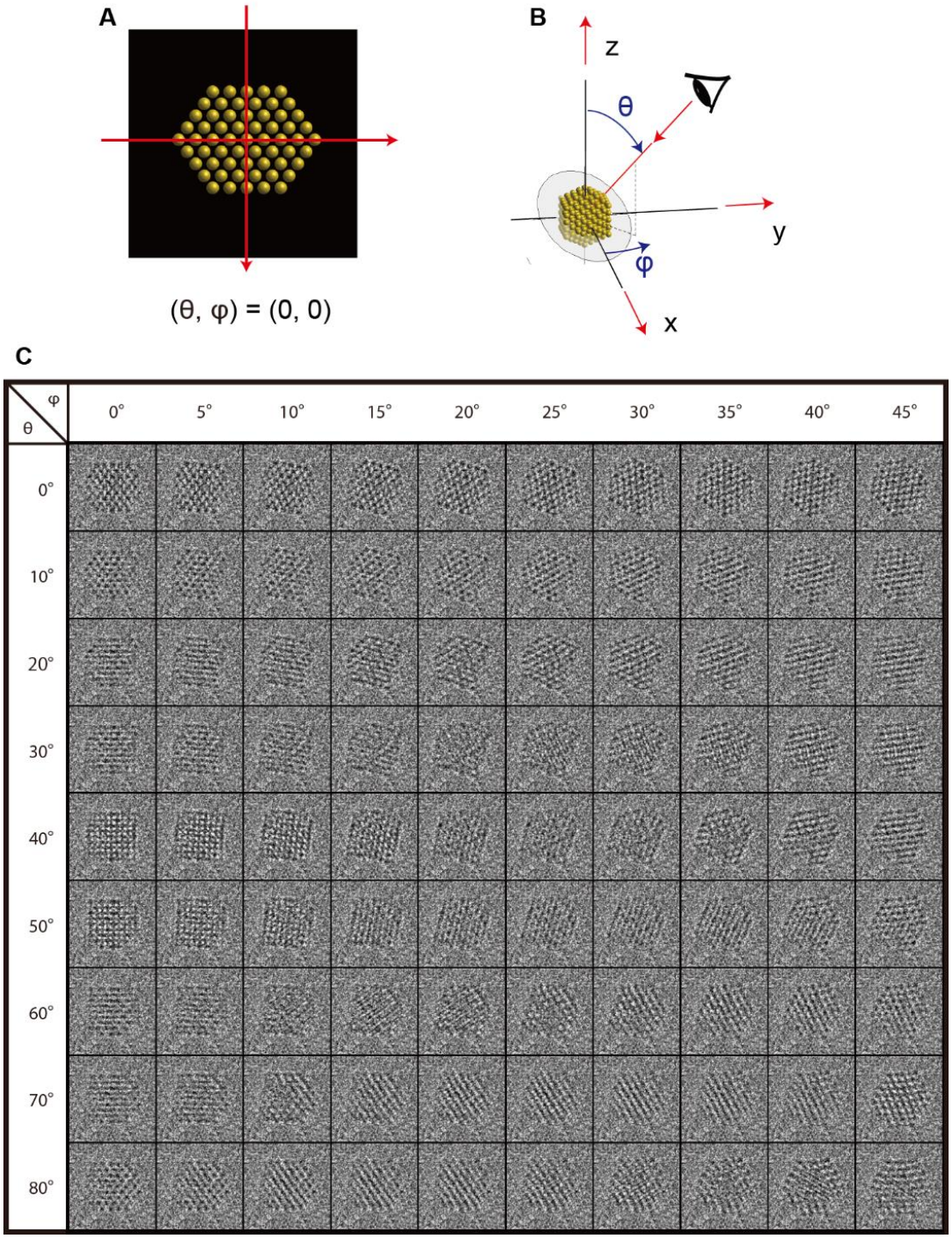

Fig. S12. Simulated TEM images of a hemispherical Au nanocrystal composed of 309 atoms (2.3 nm in diameter) observed from various viewpoints. (FCC structure) (A) The three-dimensional models of the simulated Au nanocrystal seen from (θ, φ) = (0, 0). (B) The Au nanocrystal model and the coordinates to indicate the direction of the observation. (C) The simulated images of the nanocrystal in various orientations.

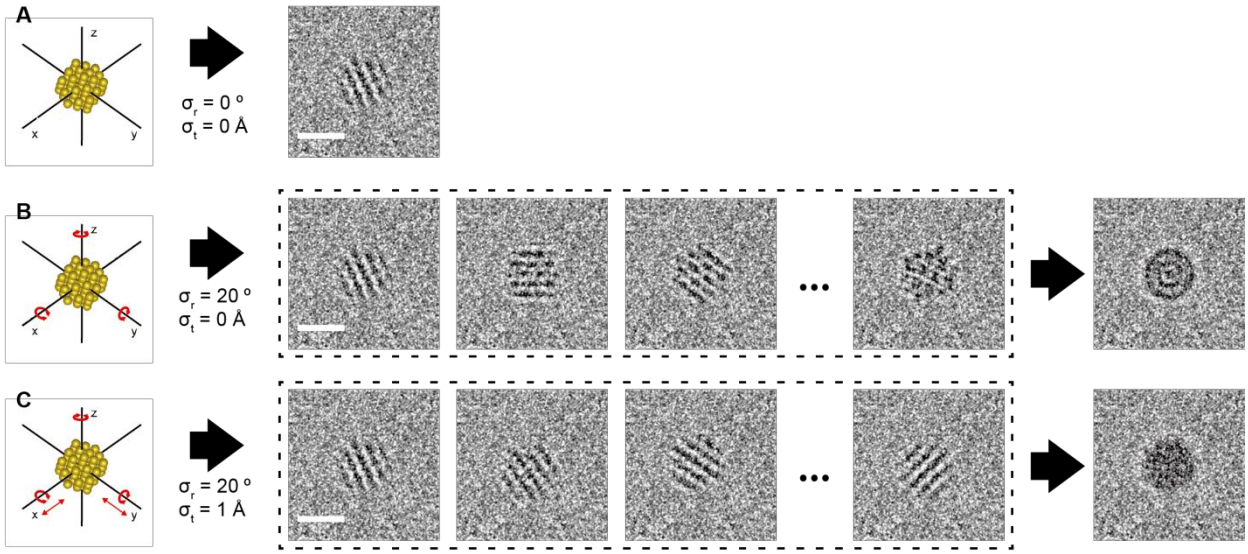

Fig. S13. Method and result of the simulation of the fast-rotating nanocrystal. If the rotating speed is too fast to be captured by the image detector, the acquired image might be shown as an averaged image of many snapshots taken at different angles. To simulate the situation, we rotated the particle at each step following the Gaussian distribution (μ = 0 degrees, σ = 20 degrees) for 200 steps, and averaged them. The resulting image appeared as concentric circles which we never observed in the in-situ TEM images, so we added a normally distributed translational movement (μ = 0 Å, σ = 1 Å) for further investigation. With the severe translational motion, the concentric circle was deleted but the image became a big gray spot, rather than fluctuating dots shown in Fig. 1B. Therefore, the TEM images that appear to show disordered nanoparticles do not appear to be consistent with motion-blurred crystalline nanoparticles. Scale bar: 1nm.

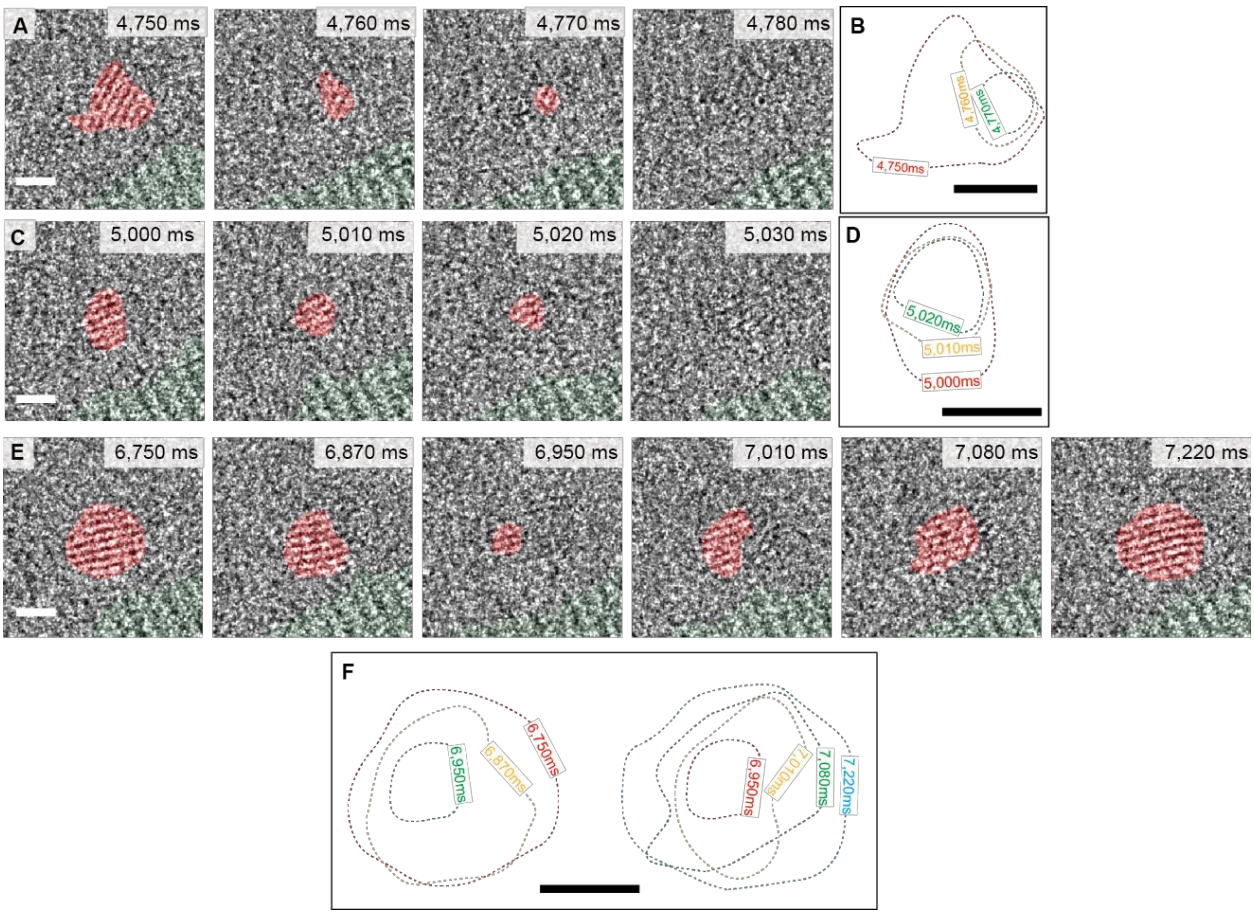

Fig. S14. The change in the shape and size of the lattice fringes during disorganization and recovery. (**A, C**) Consecutive images of in-situ TEM images from shrinkage to disappearance. (**B, D**) Time-labeled contour plots of crystalline areas in the process of disorganization. (**E**) Selected images showing shrinkage and recovery of the nanocrystal. (**F**) Time-labeled contour plots of crystalline areas during the shrinkage (left) and the recovery (right). All scale bars: 1 nm.

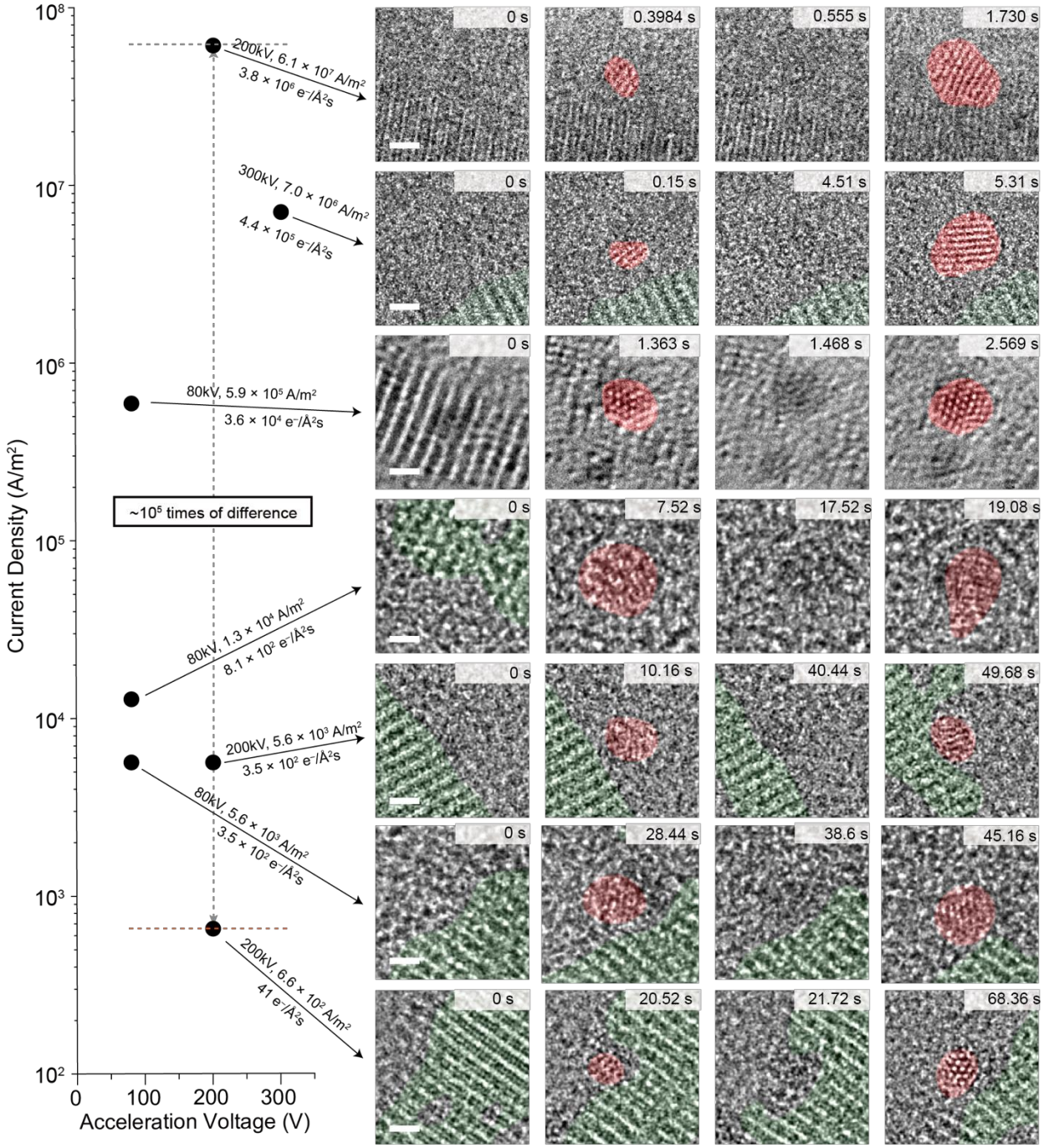

Fig. S15. The electron beam conditions that we used for the TEM observation of the nucleation sites and selected frames showing the transition between crystal and disordered state. The disorder – order transition was observed from all 7 conditions. The growth speed tends to be proportional to the dose rate but not to acceleration voltage. Growth speed at 80 kV was higher than the speed at 200 kV, when the dose rate is fixed. Scale bars: 1nm.

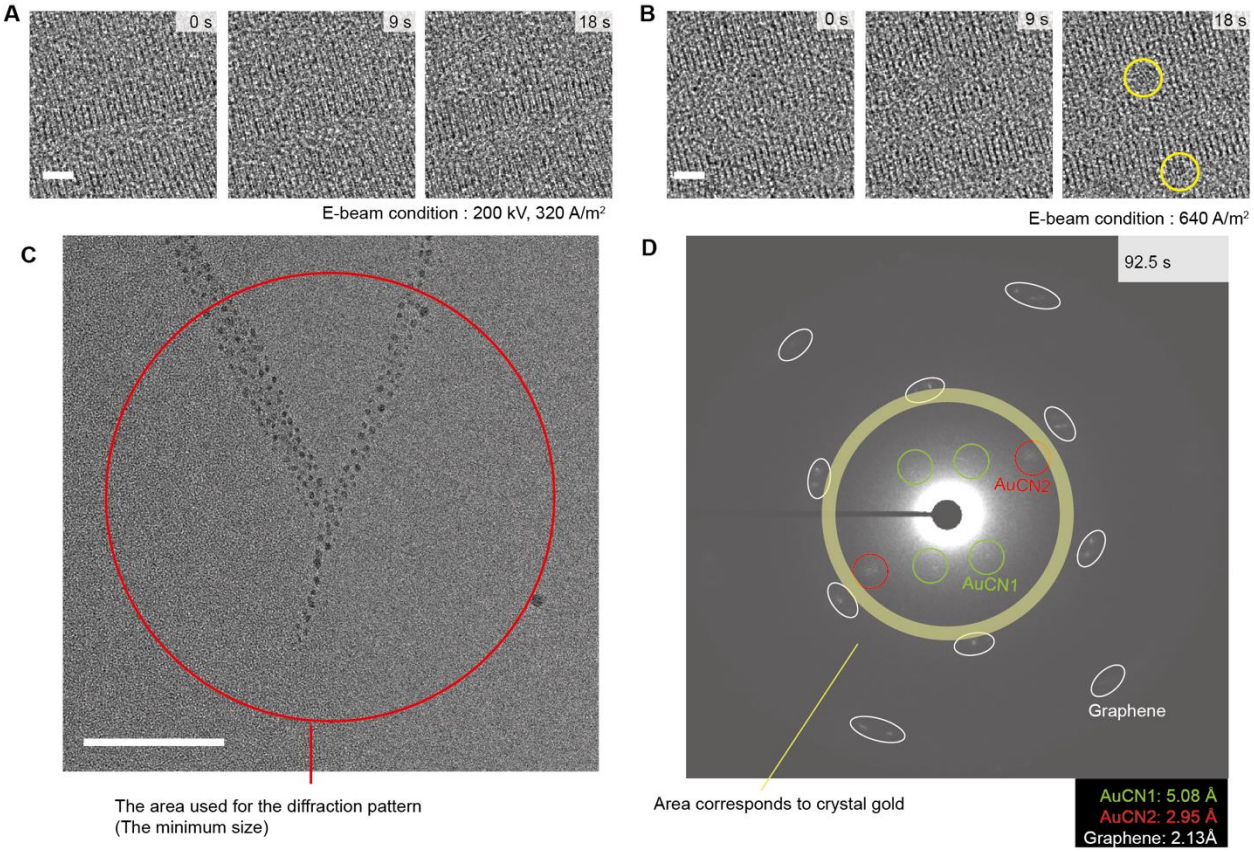

Fig. S16. Minimum dose-rate for imaging the Au nanocrystal nucleation in the current system. (**A**) AuCN nanoribbon observed at 200 kV and 320 A/m^2 (20 e$^-$/Å^{2}s). Scale bar: 1 nm. (**B**) AuCN nanoribbon observed at 200 kV and 640 A/m^2 (40 e$^-$/Å^{2}s). Scale bar: 1 nm. The minimum current density (electron dose-rate) at which AuCN nanoribbons were stably decomposed was 640 A/m^2 (40 e$^-$/ Å^{2}s) at 200 kV. (**C**) AuCN nanoribbon used for SAED (selected area electron diffraction) imaging. Scale bar: 50 nm. (**D**) SAED pattern imaged from the red-circled area in (C). Signals from tiny Au nanocrystals were not observed from the SAED pattern, because the target area used for the SAED imaging was too large (minimum 170 nm in diameter).

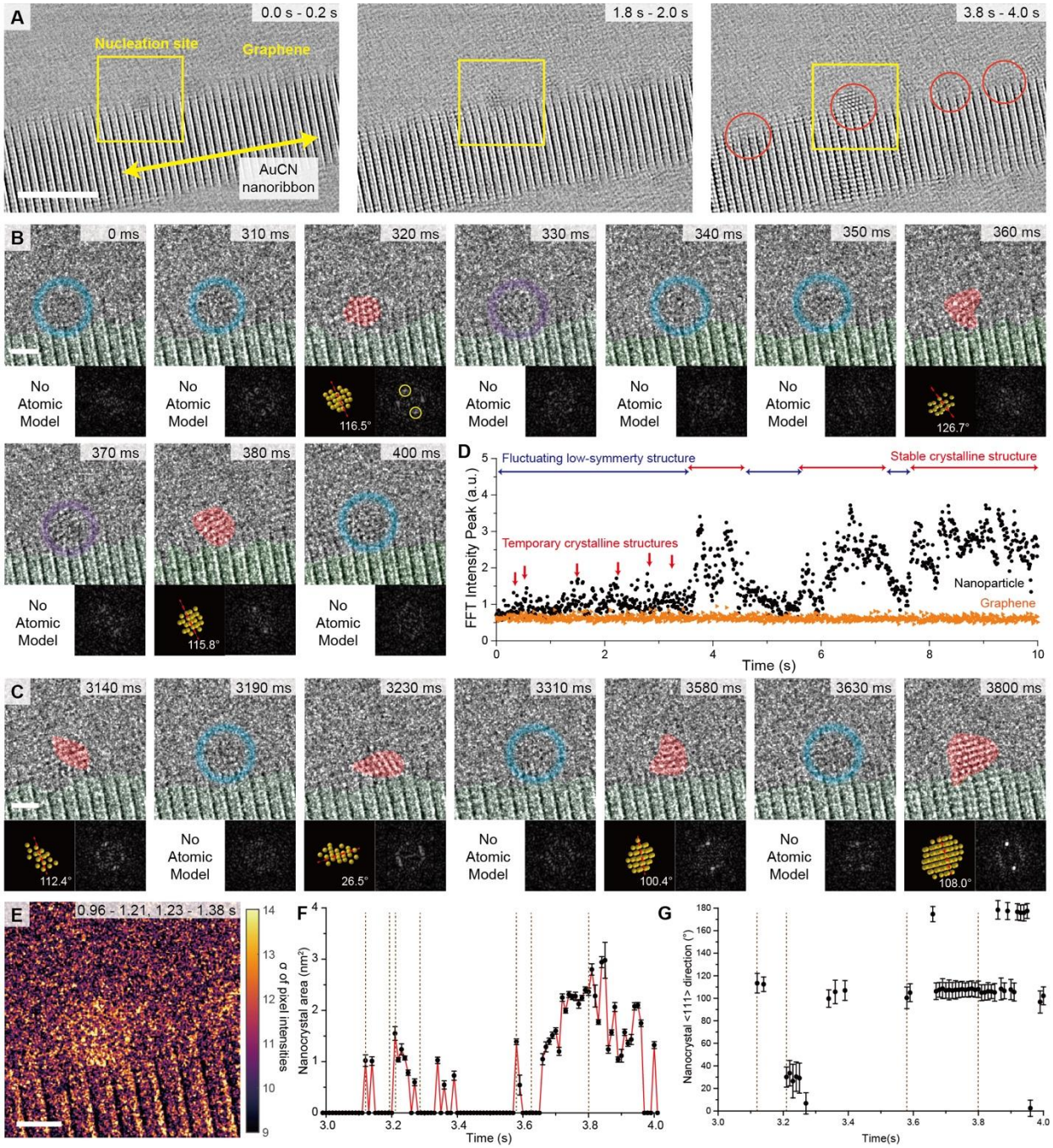

Fig. S17. Direct observation of the formation of Au nanocrystal #5 (Current density: 7.0×10^6 A/m^2, Accelerating voltage: 300 kV, Temporal resolution: 10 ms). (**A**) Sequential TEM images obtained by frame averaging. Scale bar: 5 nm. (**B**, **C**) Individual frames showing a nucleation process. Scale bar: 1 nm. Red areas, light-green areas, blue circles, and purple circles indicate Au crystal lattices, AuCN nanowires, nanoclusters in the disordered state, and nanoclusters in the undefinable state (the crystalline/disordered classification is unclear), respectively. (**D**) The maximum intensity of the FFT image. (**E**) A color map obtained from standard deviations of intensities for each pixel. Scale bar: 1 nm. (**F**) Nanocrystal area. (**G**) Direction of <111> lattices. Vertical dotted lines in (F) and (G) correspond to the time-labeled images in (C).

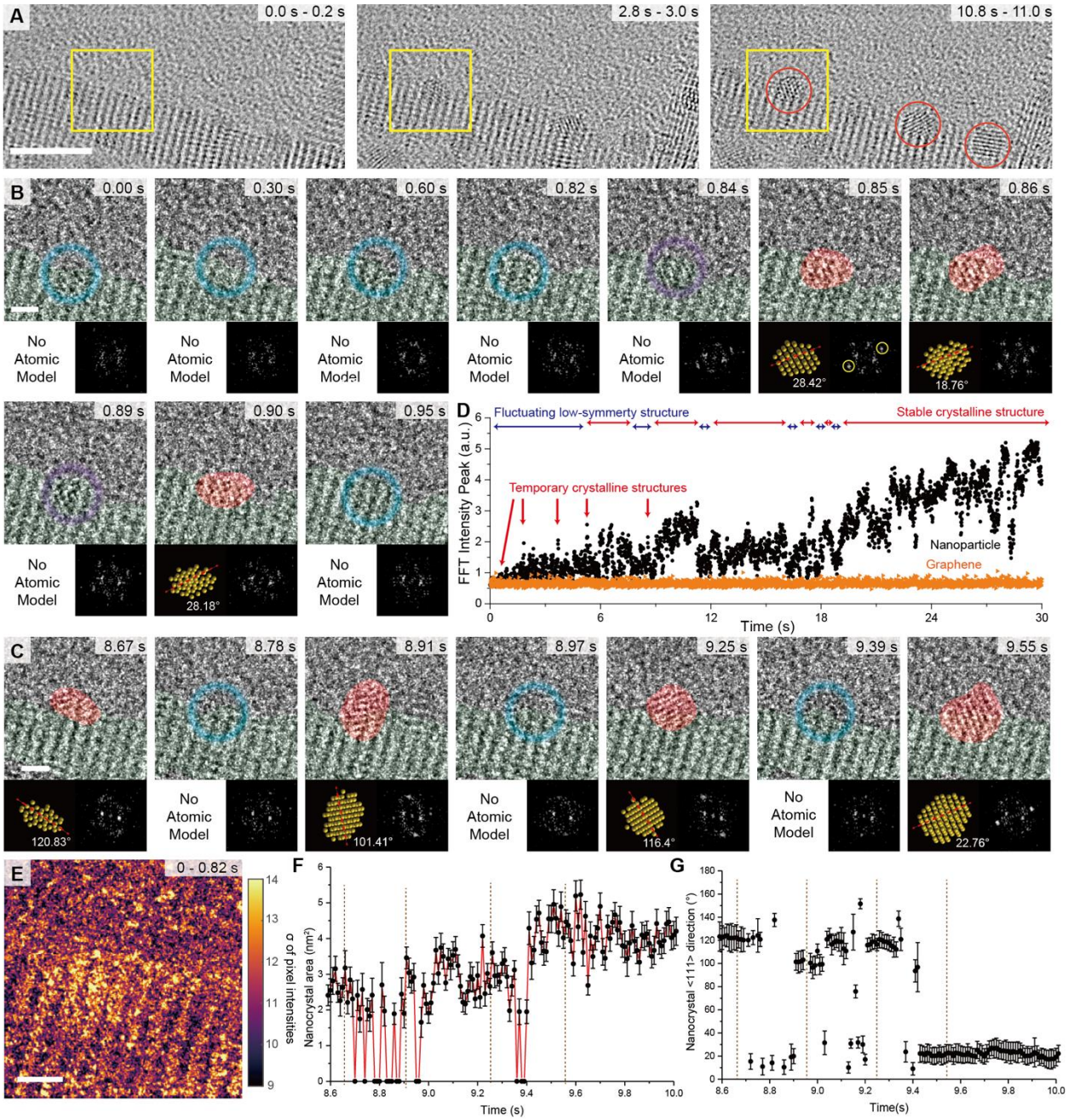

Fig. S18. Direct observation of the formation of Au nanocrystal #7 (Current density: 7.0×10^6 A/m^2, Accelerating voltage: 300 kV, Temporal resolution: 10 ms). (**A**) Sequential TEM images obtained by frame averaging. Scale bar: 5 nm. (**B**, **C**) Individual frames showing a nucleation process. Scale bar: 1 nm. Red areas, light-green areas, blue circles, and purple circles indicate Au crystal lattices, AuCN nanowires, nanoclusters in the disordered state, and nanoclusters in the undefinable state (the crystalline/disordered classification is unclear), respectively. (**D**) The maximum intensity of the FFT image. (**E**) A color map obtained from standard deviations of intensities for each pixel. Scale bar: 1 nm. (**F**) Nanocrystal area. (**G**) Direction of <111> lattices. Vertical dotted lines in (F) and (G) correspond to the time-labeled images in (C).

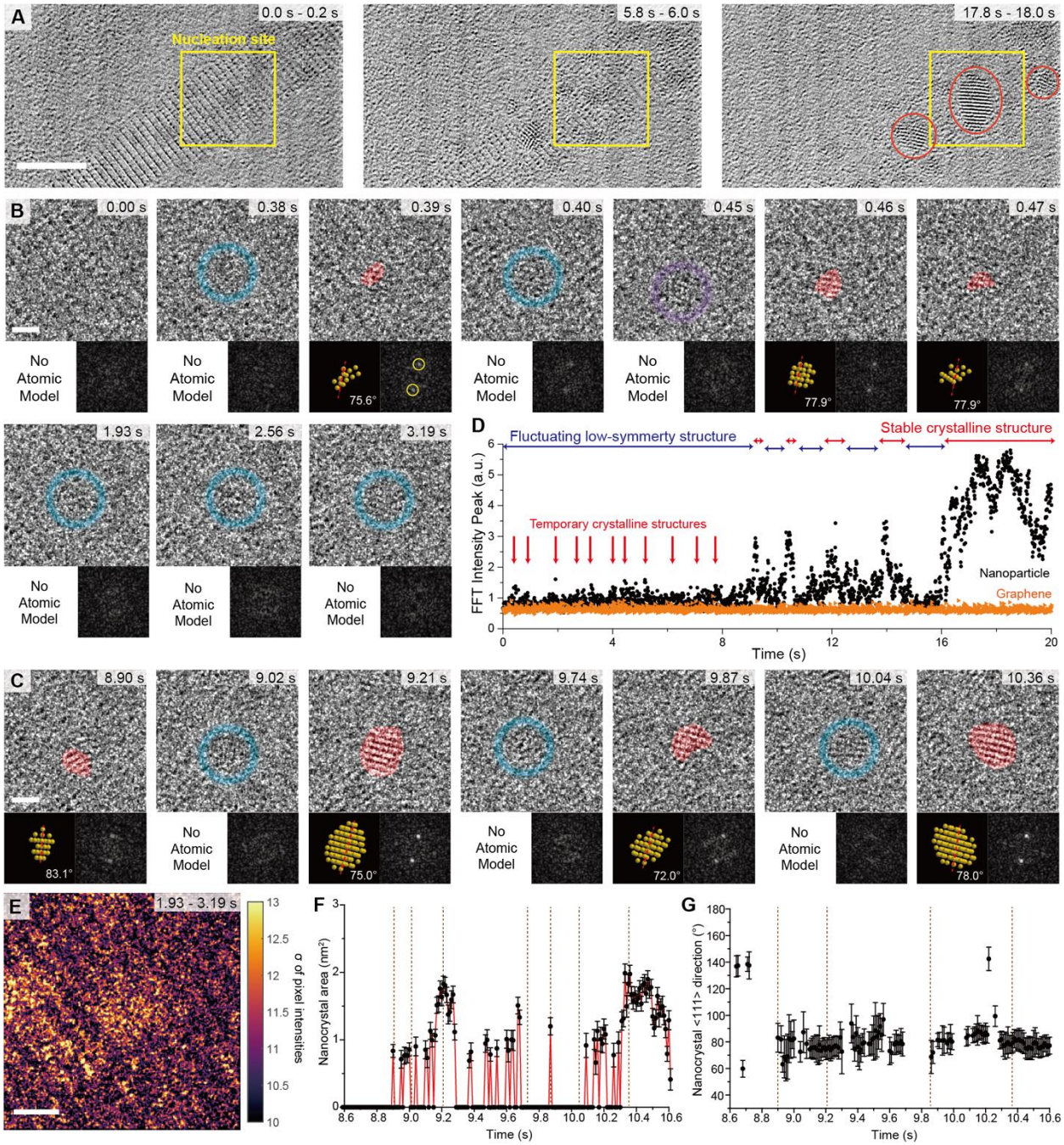

Fig. S19. Direct observation of the formation of Au nanocrystal #10 (Current density: 7.0×10^6 A/m^2, Accelerating voltage: 300 kV, Temporal resolution: 10 ms). (**A**) Sequential TEM images obtained by frame averaging. Scale bar: 5 nm. (**B**, **C**) Individual frames showing a nucleation process. Scale bar: 1 nm. Red areas, light-green areas, blue circles, and purple circles indicate Au crystal lattices, AuCN nanowires, nanoclusters in the disordered state, and nanoclusters in the undefinable state (the crystalline/disordered classification is unclear), respectively. (**D**) The maximum intensity of the FFT image. (**E**) A color map obtained from standard deviations of intensities for each pixel. Scale bar: 1 nm. (**F**) Nanocrystal area. (**G**) Direction of <111> lattices. Vertical dotted lines in (F) and (G) correspond to the time-labeled images in (C).

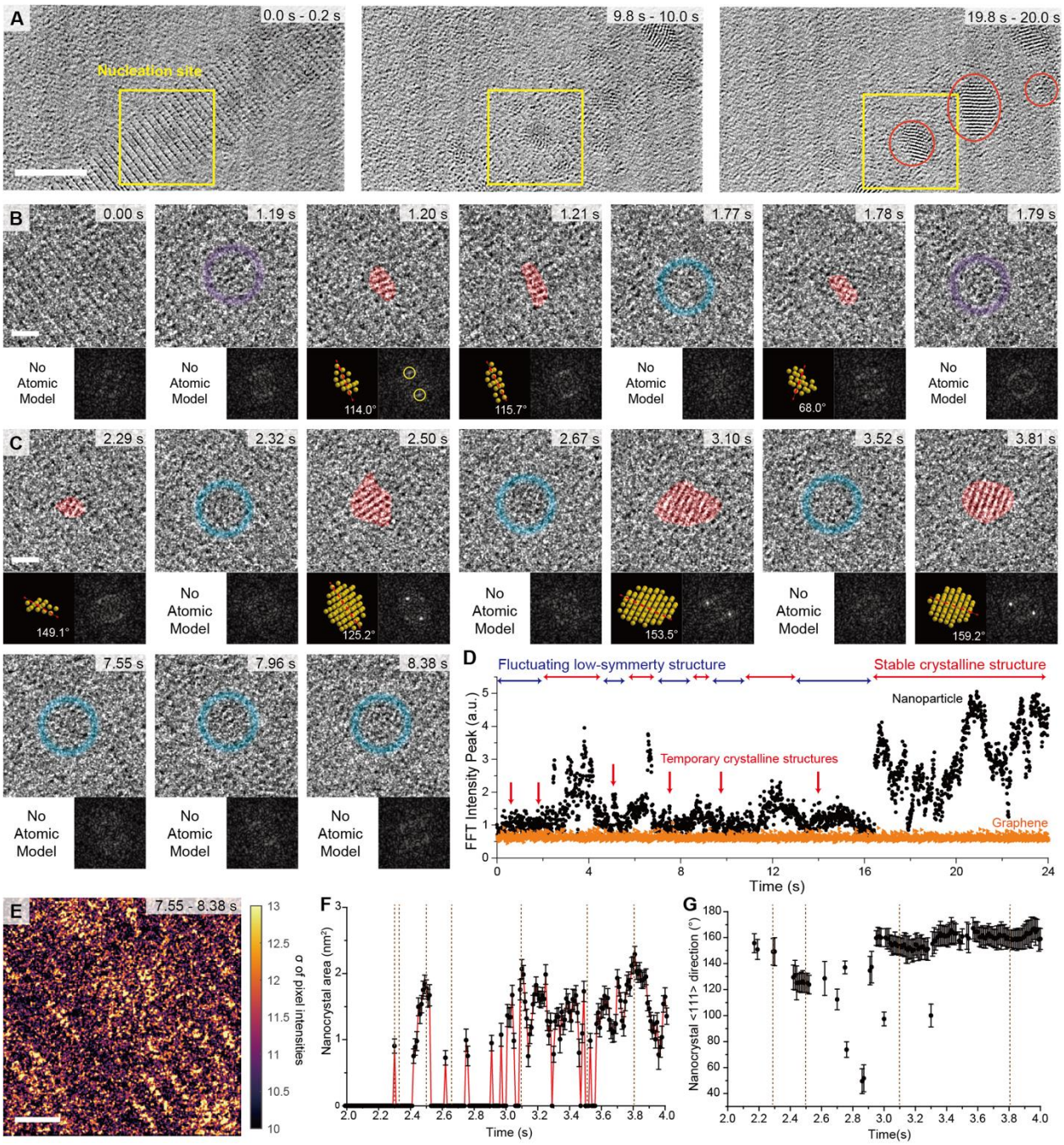

Fig. S20. Direct observation of the formation of Au nanocrystal #12 (Current density: 7.0×10^6 A/m^2, Accelerating voltage: 300 kV, Temporal resolution: 10 ms). (**A**) Sequential TEM images obtained by frame averaging. Scale bar: 5 nm. (**B**, **C**) Individual frames showing a nucleation process. Scale bar: 1 nm. Red areas, light-green areas, blue circles, and purple circles indicate Au crystal lattices, AuCN nanowires, nanoclusters in the disordered state, and nanoclusters in the undefinable state (the crystalline/disordered classification is unclear), respectively. (**D**) The maximum intensity of the FFT image. (**E**) A color map obtained from standard deviations of intensities for each pixel. Scale bar: 1 nm. (**F**) Nanocrystal area. (**G**) Direction of <111> lattices. Vertical dotted lines in (F) and (G) correspond to the time-labeled images in (C).

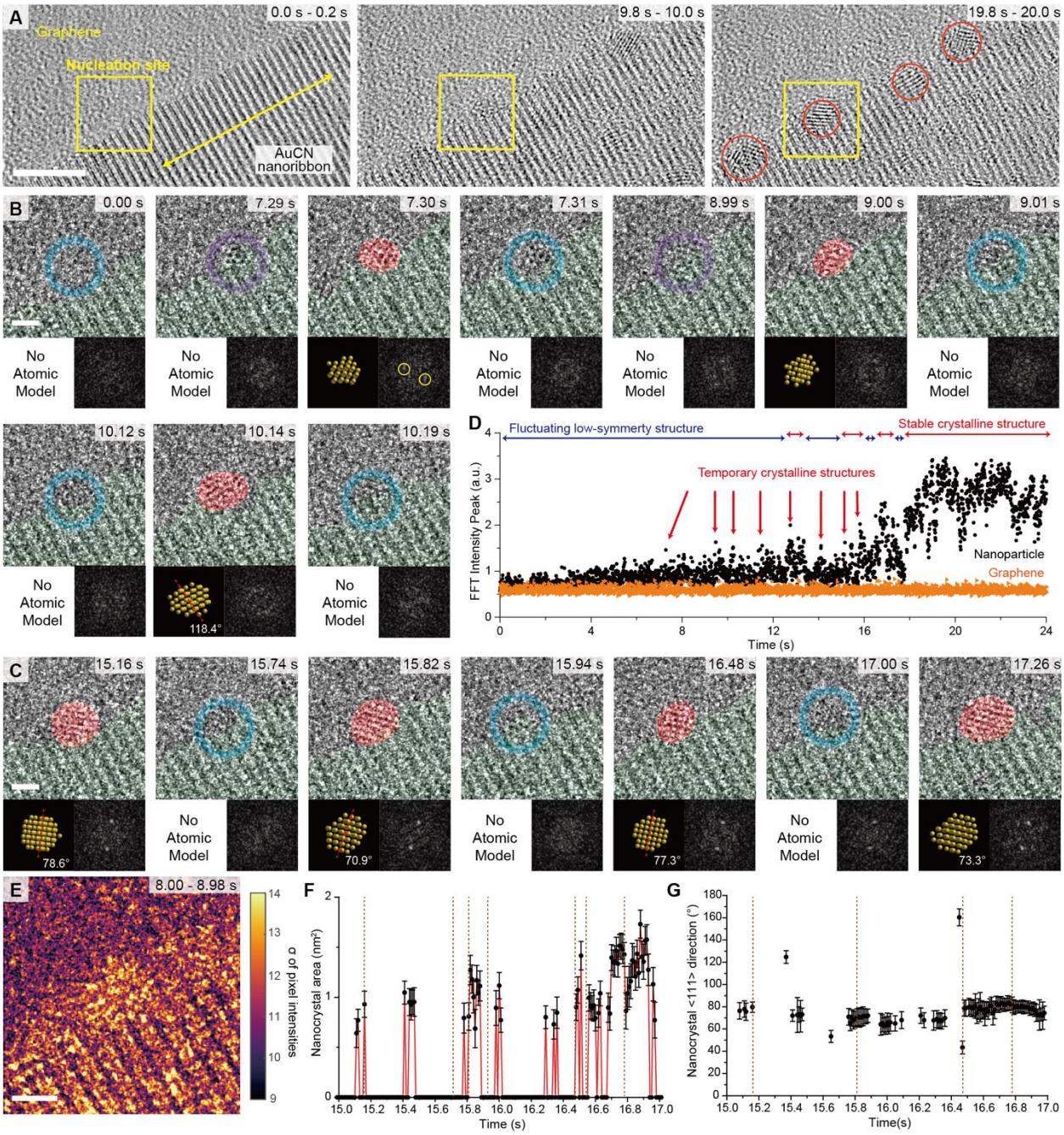

Fig. S21. Direct observation of the formation of Au nanocrystal #20 (Current density: 7.0×10^6 A/m^2, Accelerating voltage: 300 kV, Temporal resolution: 10 ms). (**A**) Sequential TEM images obtained by frame averaging. Scale bar: 5 nm. (**B**, **C**) Individual frames showing a nucleation process. Scale bar: 1 nm. Red areas, light-green areas, blue circles, and purple circles indicate Au crystal lattices, AuCN nanowires, nanoclusters in the disordered state, and nanoclusters in the undefinable state (the crystalline/disordered classification is unclear), respectively. (**D**) The maximum intensity of the FFT image. (**E**) A color map obtained from standard deviations of intensities for each pixel. Scale bar: 1 nm. (**F**) Nanocrystal area. (**G**) Direction of <111> lattices. Vertical dotted lines in (F) and (G) correspond to the time-labeled images in (C).

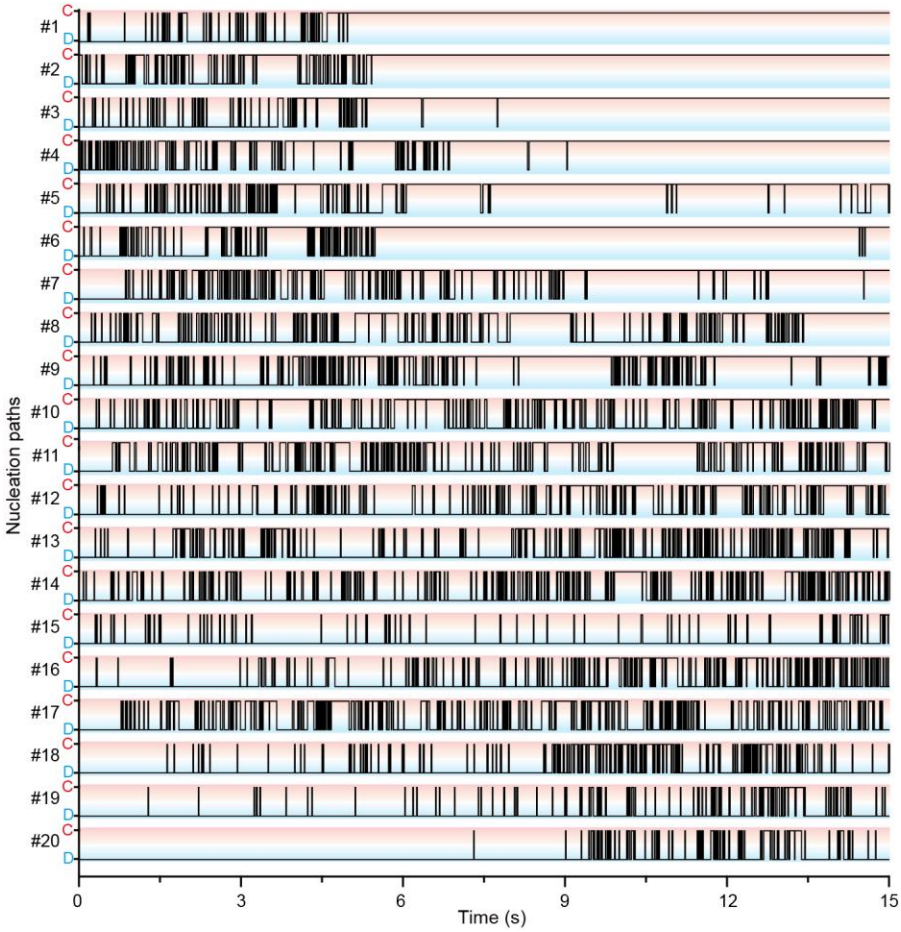

Fig. S22. Trajectories of structural transitions between disordered and crystalline states in 20 nucleation paths (Current density: 7.0×10^6 A/m^2, Accelerating voltage: 300 kV, Temporal resolution: 10 ms). Red and blue shadings are visual guides for indicating crystalline (labeled C) and disordered (labeled D) states, respectively. The nucleation path #1 is the data set in Fig. 1 and a summarized version of this figure is presented in Fig. 2A.

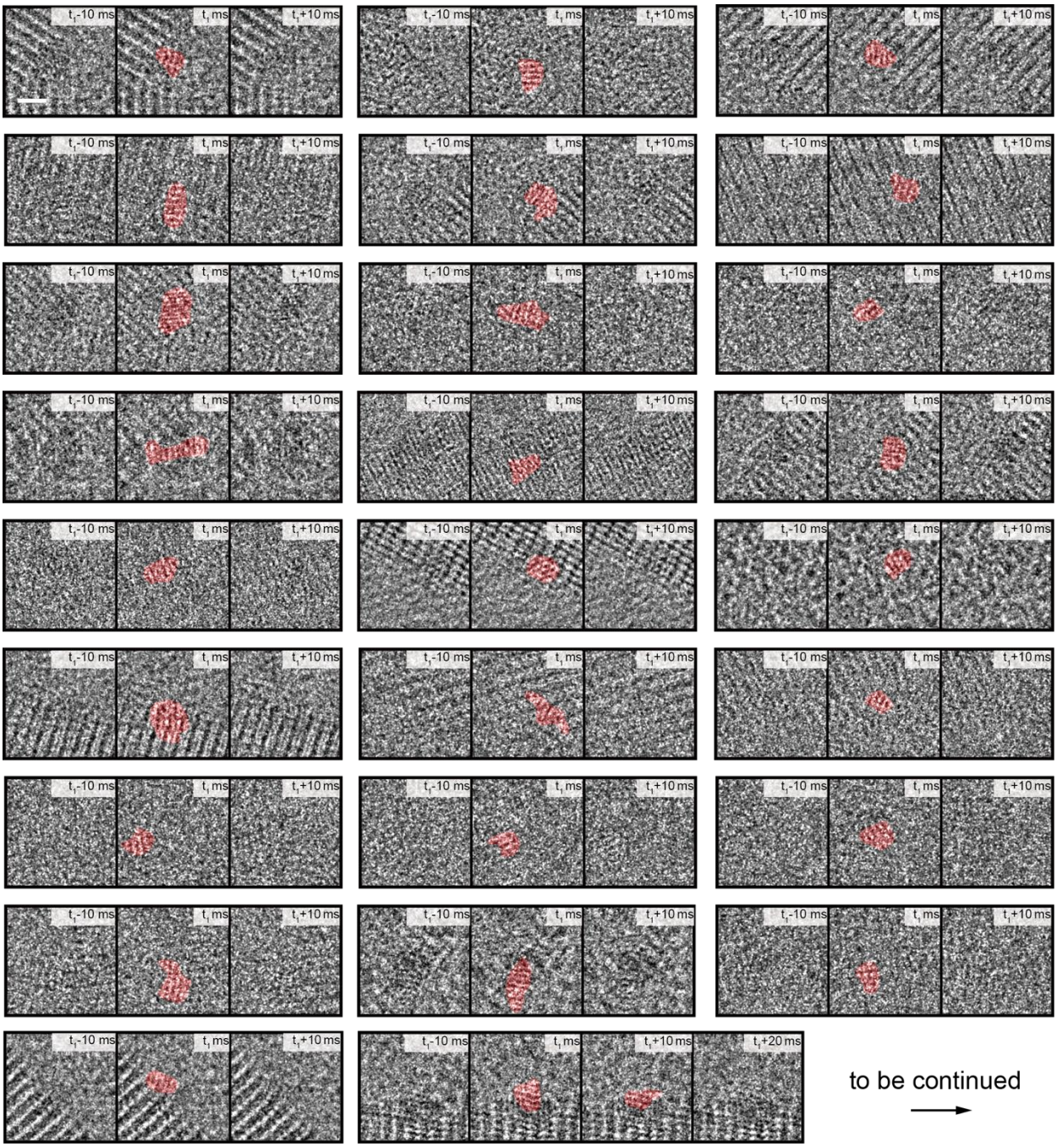

to be continued →

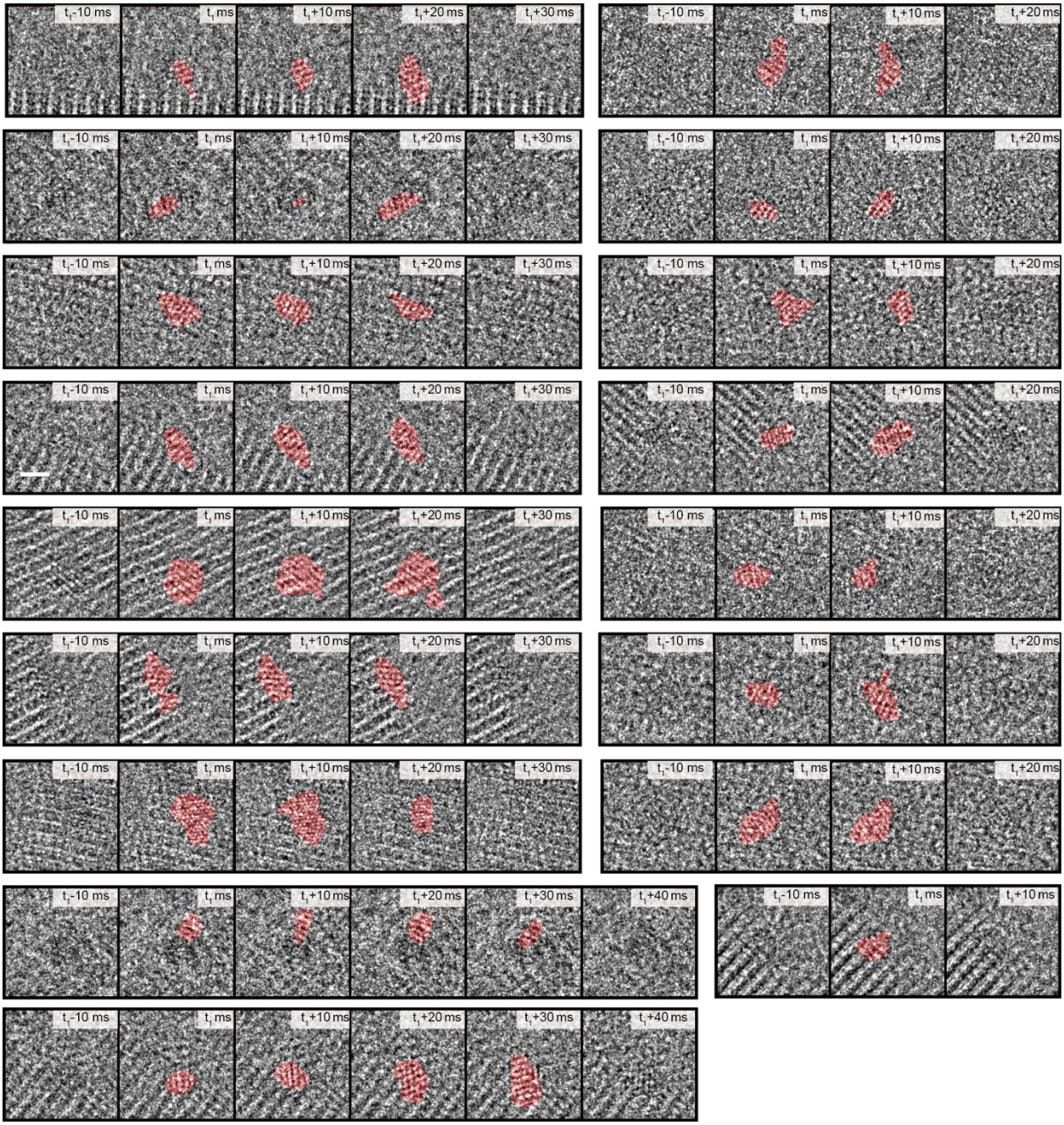

Fig. S23. The first short-lived lattice fringes observed from 44 different nucleation paths (Current density: 7.0×10^6 A/m^2, Accelerating voltage: 300 kV, Temporal resolution: 10 ms). We have observed short-lived lattice fringes from all 50 nucleation paths which are shown here (44 paths), in Fig. 1(1 path), and in fig. S17-S21 (5 paths).

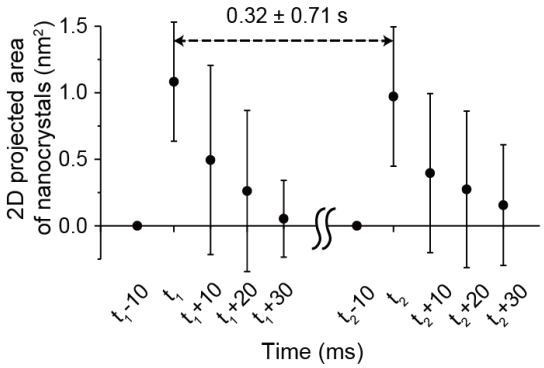

Fig. S24. Averaged areas of the first (at t_1) and the second (at t_2) lattice fringes in 50 nucleation paths (Current density: 7.0×10^6 A/m^2, Accelerating voltage: 300 kV, Temporal resolution: 10 ms). The average of the first and the second nanocrystals were ~1.1 nm^2. Most of the first and the second nanocrystals disappeared in ~30 ms.

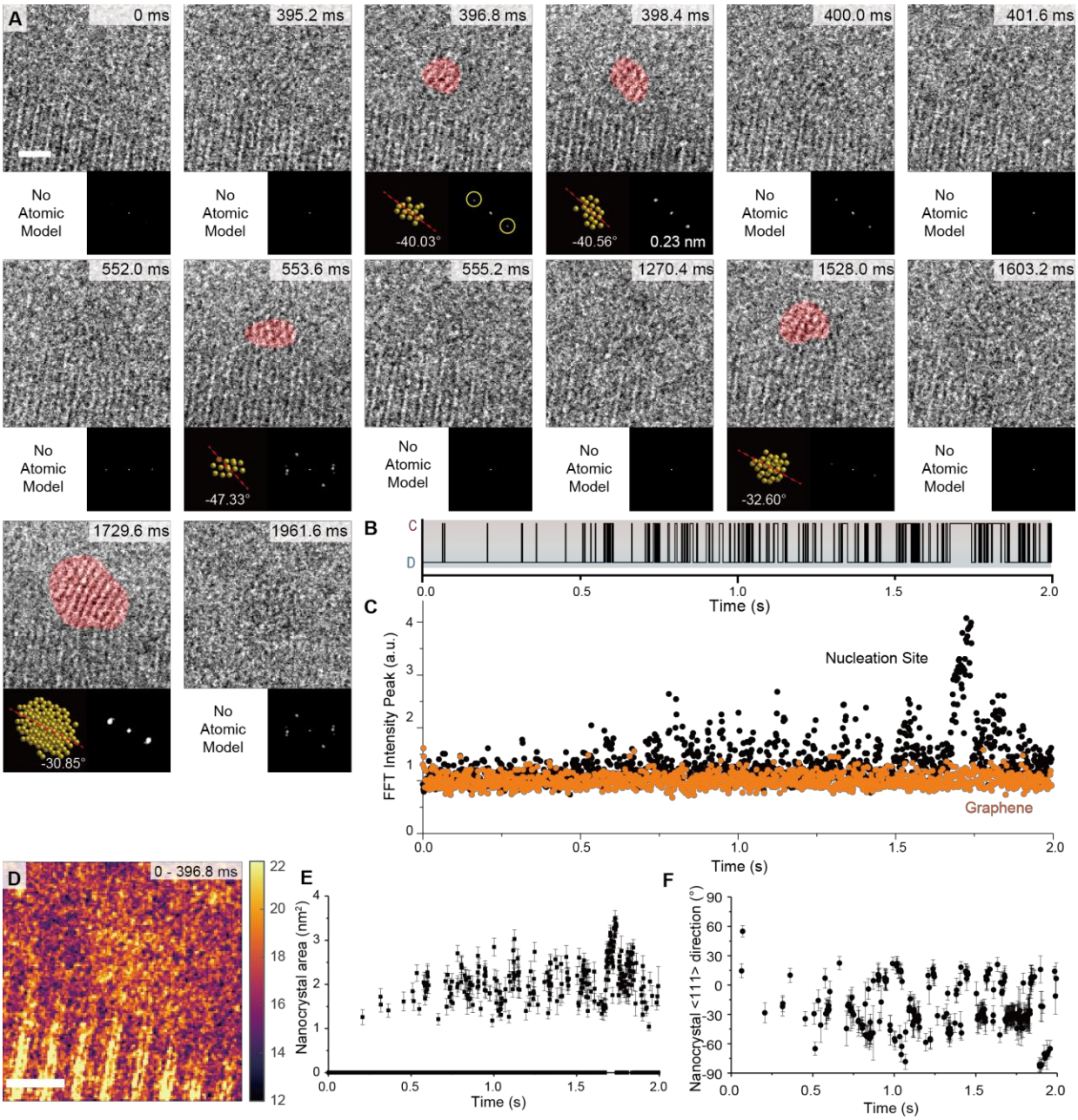

Fig. S25. Direct observation of the formation of an Au nanocrystal at higher temporal resolution (Current density: 6.1×10^7 A/m^2, Accelerating voltage: 200 kV, Temporal resolution: 1.6 ms). (**A**) Individual frames from movie S3 showing nucleation. Lower left: the atomic model of the nanocrystal. Red dashed lines indicate nanocrystal <111> directions. Lower right: FFT (Fast Fourier Transform) image. Scale bar: 1 nm. The areas of Au lattices are pseudo-colored in red. (**B**) Trajectories of structural transitions between disordered and crystalline states. (**C**) The maximum intensity of the FFT image as a function of time. The signals from a graphene area represent ground noise levels (negative control) of this analysis. (**D**) A color map obtained from standard deviations of intensities for each pixel from 0 to 396.8 ms. Scale bar: 1 nm. (**E**) Nanocrystal area and (**F**) direction of <111> lattices from 0.0 to 2.0 s.

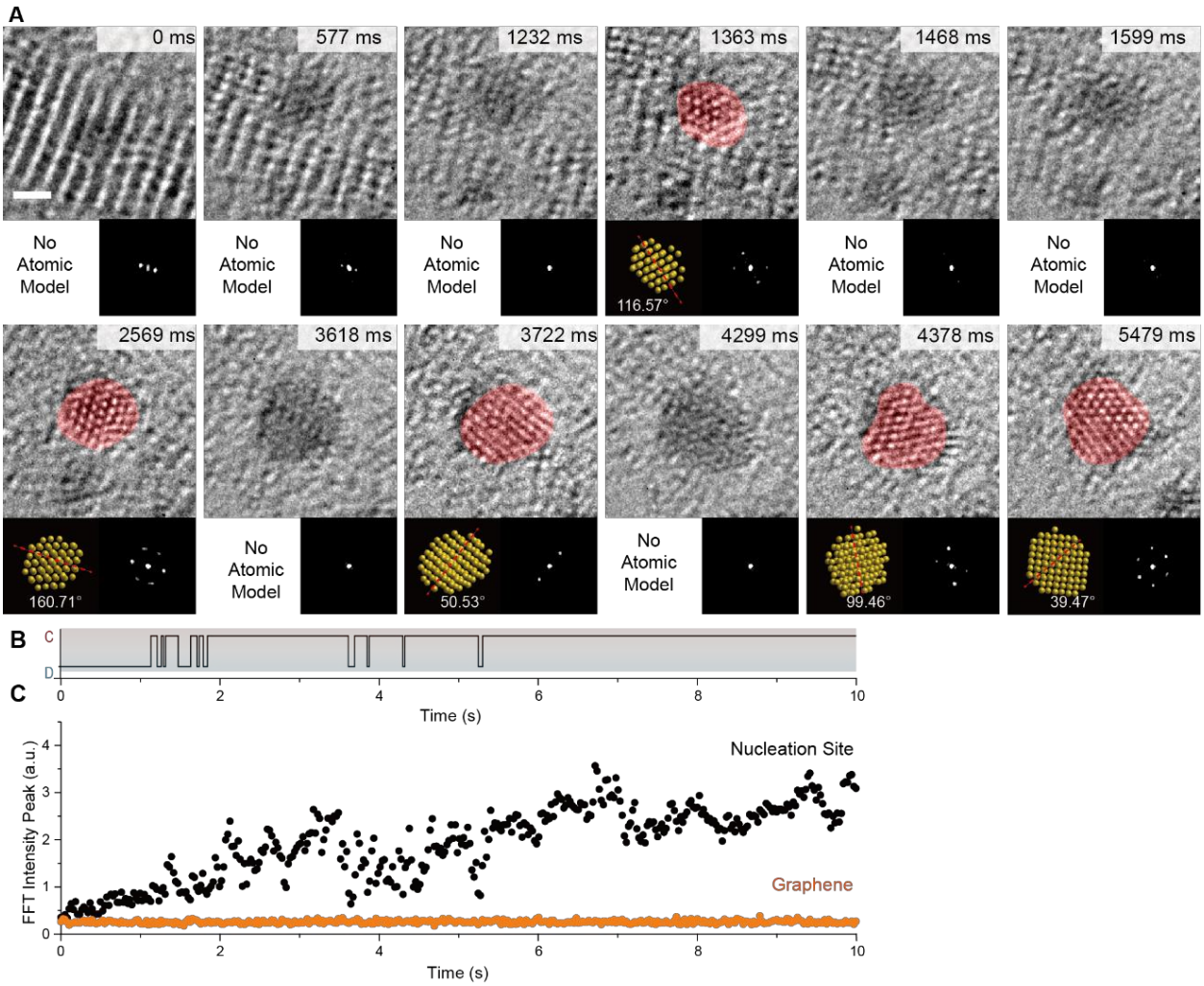

Fig. S26. Direct observation of the formation of an Au nanocrystal (Current density: 5.9×10^5 A/m^2, Accelerating voltage: 80 kV, Temporal resolution: 26.2 ms). (**A**) Individual frames from movie S4 showing nucleation. Lower left: the atomic model of the nanocrystal. Lower right: FFT (Fast Fourier Transform) image. Scale bar: 1 nm. The areas of Au lattices are pseudo-colored in red. (**B**) Trajectories of structural transitions between disordered and crystalline states. (**C**) The maximum intensity of the FFT image as a function of time. The signals from a graphene area represent ground noise levels (negative control) of this analysis.

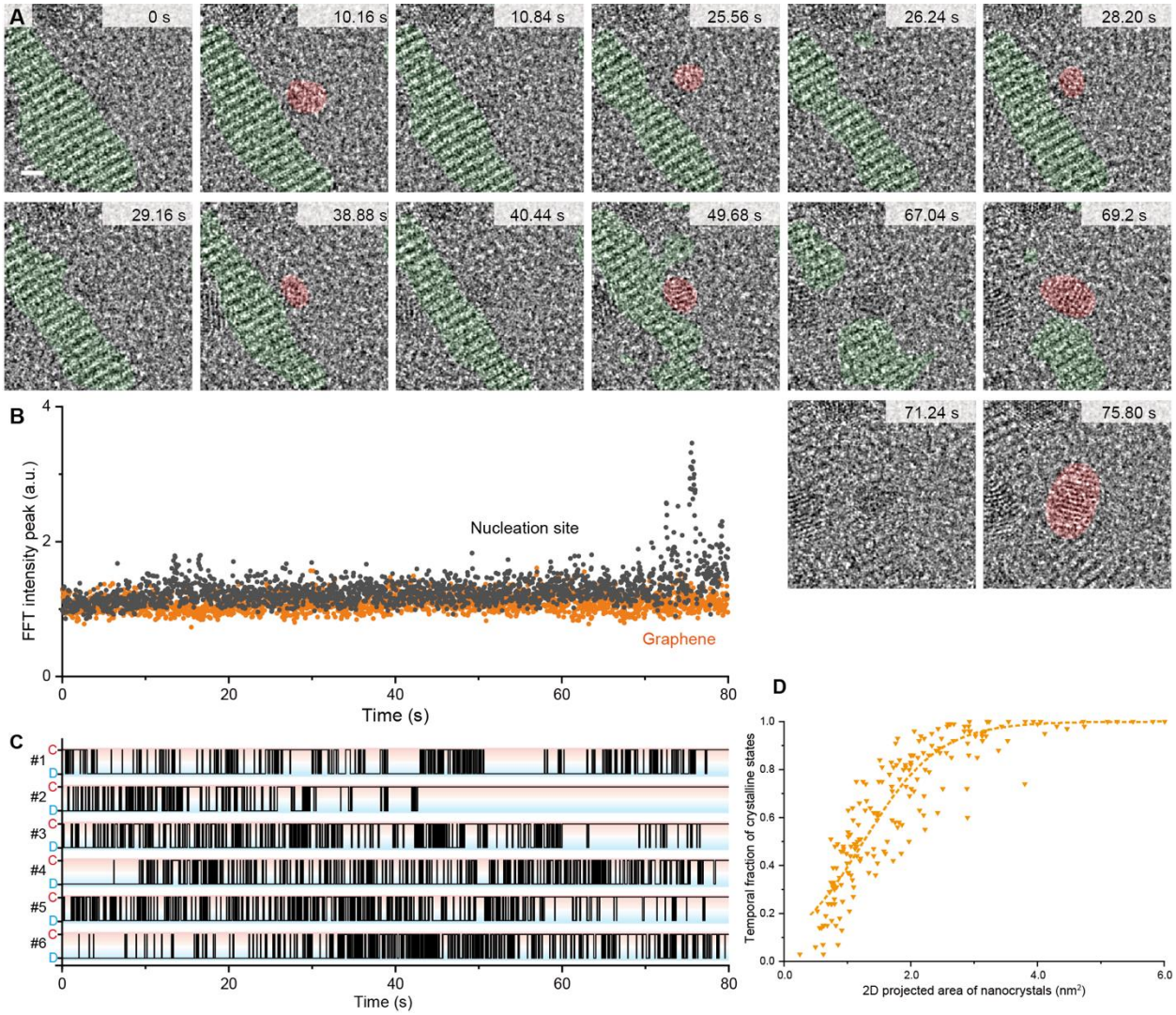

Fig. S27. Direct observation of the formation of an Au nanocrystal under a low electron-dose condition (Current density: 5.6×10^3 A/m^2, Accelerating voltage: 200 kV, Temporal resolution: 40 ms). (**A**) Individual frames obtained by frame averaging showing nucleation process. Scale bar: 1 nm. The areas of Au lattices are pseudo-colored in red. (**B**) The maximum intensity of the FFT image as a function of time. The signals from a graphene area represent ground noise levels (negative control) of this analysis. (**C**) Trajectories of structural transitions between disordered and crystalline states. (**D**) Temporal fraction of crystalline states versus 2D projected area of Au nanocrystals during the nucleation process. The dashed line represents a fitting curve to the data with a sigmoid (logistic) function. This graph is compared to results obtained from other electron beam conditions in Fig. 3A.

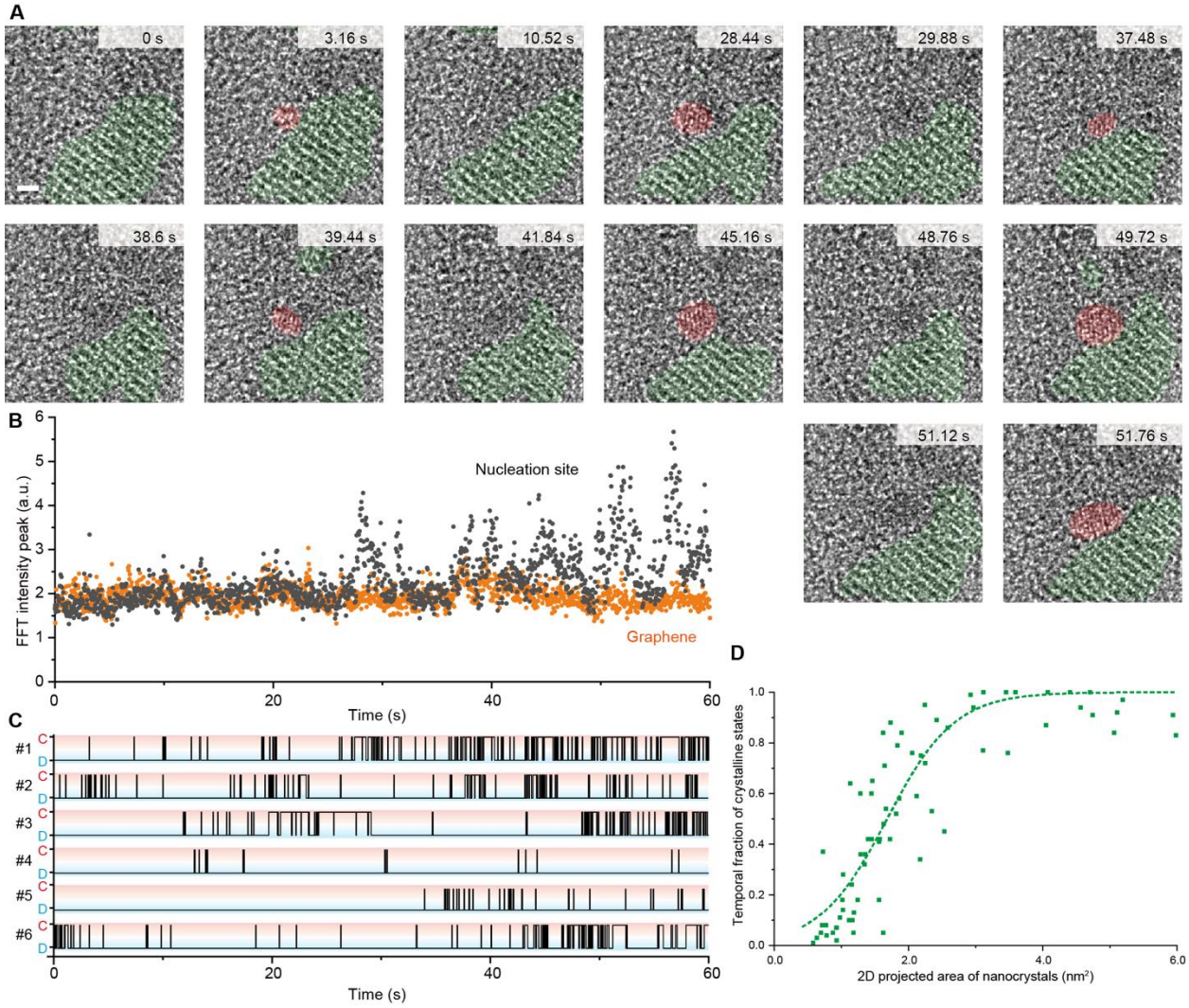

Fig. S28. Direct observation of the formation of an Au nanocrystal under a low electron-dose condition (Current density: 5.6×10^3 A/m^2, Accelerating voltage: 80 kV, Temporal resolution: 40 ms). (**A**) Individual frames obtained by frame averaging showing nucleation process. Scale bar: 1 nm. The areas of Au lattices are pseudo-colored in red. (**B**) The maximum intensity of the FFT image as a function of time. The signals from a graphene area represent ground noise levels (negative control) of this analysis. (**C**) Trajectories of structural transitions between disordered and crystalline states. (**D**) Temporal fraction of crystalline states versus 2D projected area of Au nanocrystals during the nucleation process. The dashed line represents a fitting curve to the data with a sigmoid (logistic) function. This graph is compared to results obtained from other electron beam conditions in Fig. 3A.

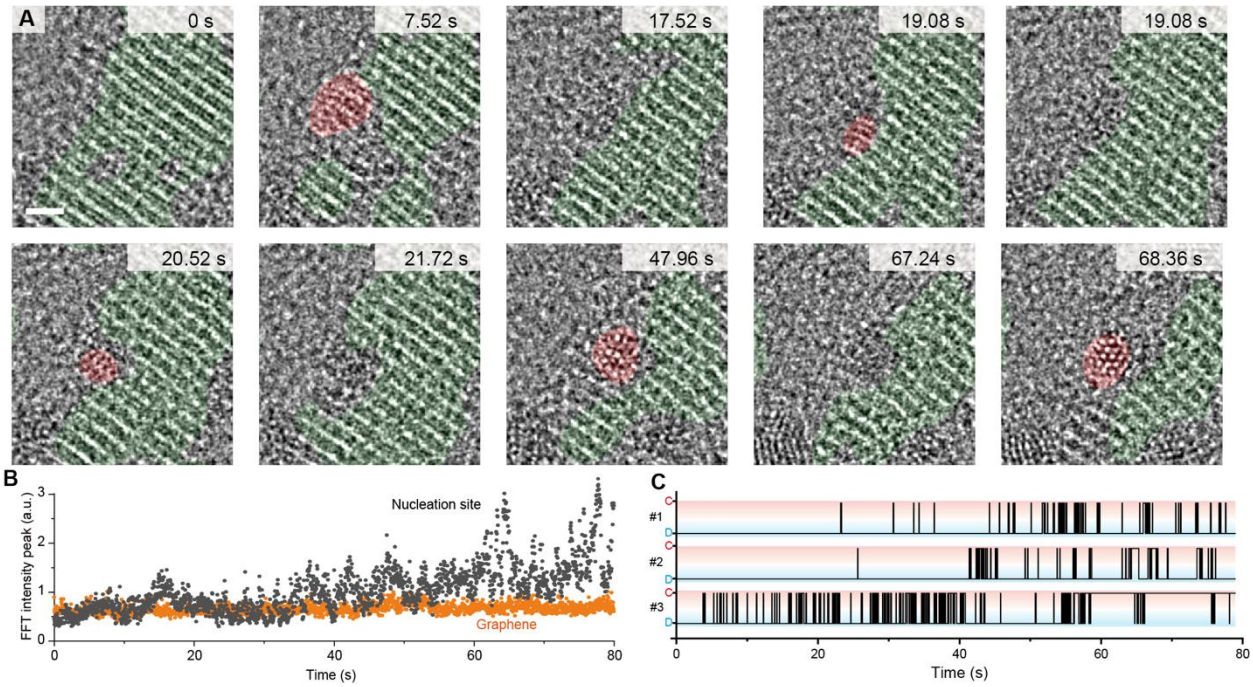

Fig. S29. Direct observation of the formation of an Au nanocrystal under a low electron-dose condition (Current density: 6.5×10^2 A/m^2, Accelerating voltage: 200 kV, Temporal resolution: 40 ms). (**A**) Individual frames from movie S5 showing nucleation. Scale bar: 1 nm. The areas of Au lattices are pseudo-colored in red. (**B**) The maximum intensity of the FFT image as a function of time. The signals from a graphene area represent ground noise levels (negative control) of this analysis. (**C**) Trajectories of structural transitions between disordered and crystalline states.

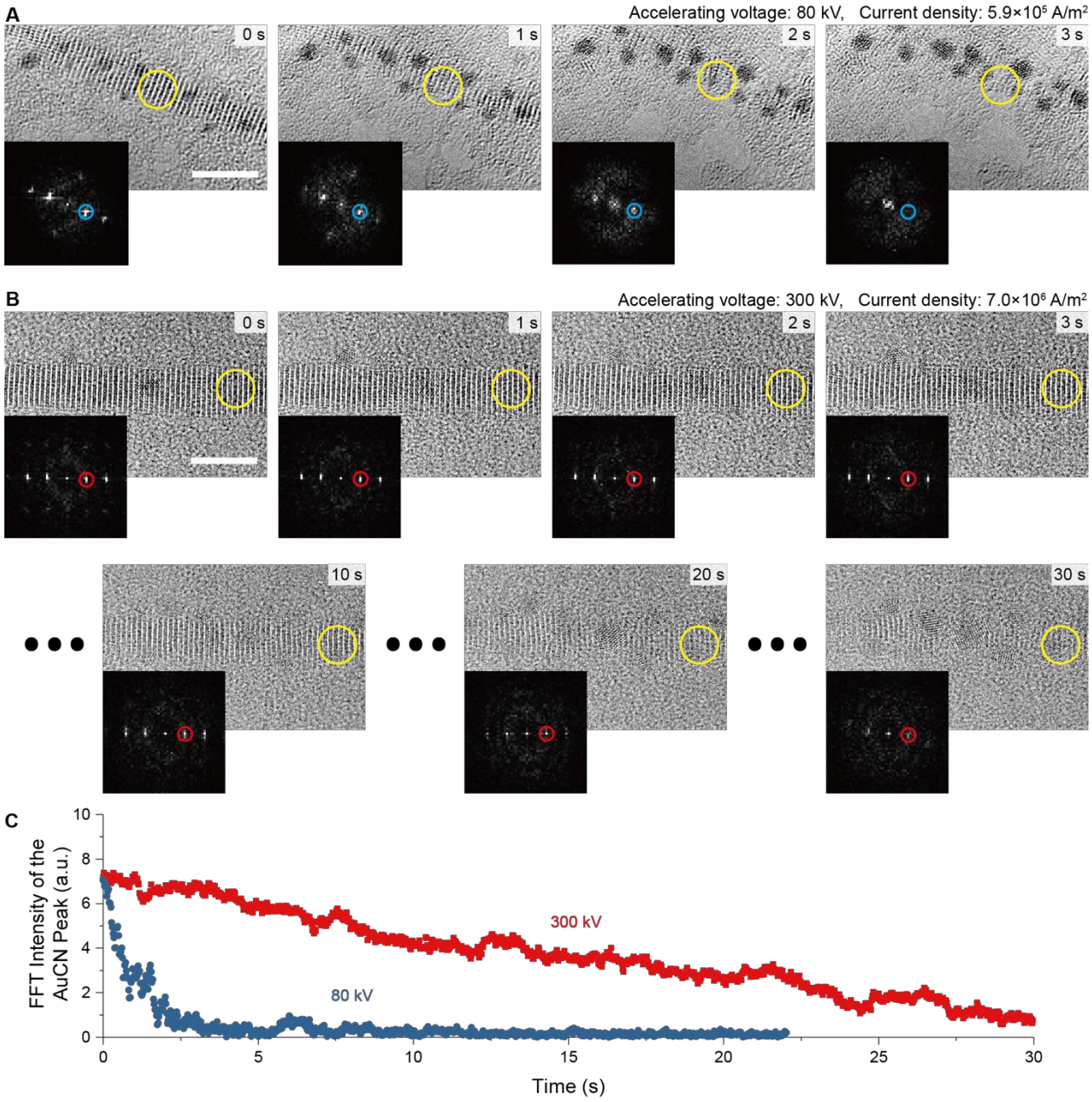

Fig. S30. Radiolytic decomposition of AuCN nanoribbons under two different accelerating voltages of the electron beam. (**A, B**) Selected snapshots of in-situ TEM movies captured under 80 kV, 5.9×10^5 A/m^2 (A) and 300 kV, 7.0×10^6 A/m^2 (B) electron beams. Lower left: FFT images that show AuCN peaks in blue and red circles. Scale bars: 5 nm. (**C**) Intensities of the AuCN peaks in FFT images (A, B) as a function of time. In this observation, the 80 kV electron beam decomposes AuCN nanoribbons ~10 times faster than the 300 kV electron beam does.

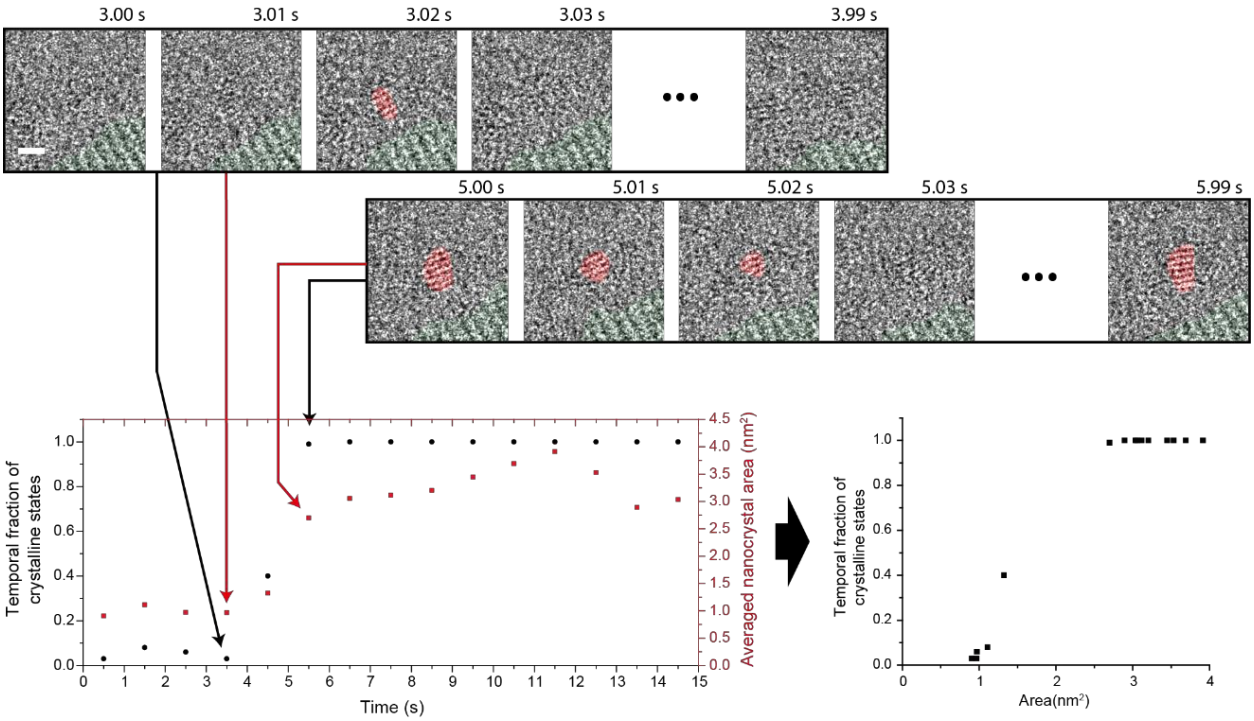

Fig. S31. Deriving the relation between the area and the stability of a nanocrystal. As the nanocrystals grow, they become more likely to exist as a crystal rather than as disordered atoms. To show this, we calculated the temporal fraction of crystalline states in a unit time (1.00 s). This tendency is clear regardless of the data being plotted as a function of time (left) or of area (right).

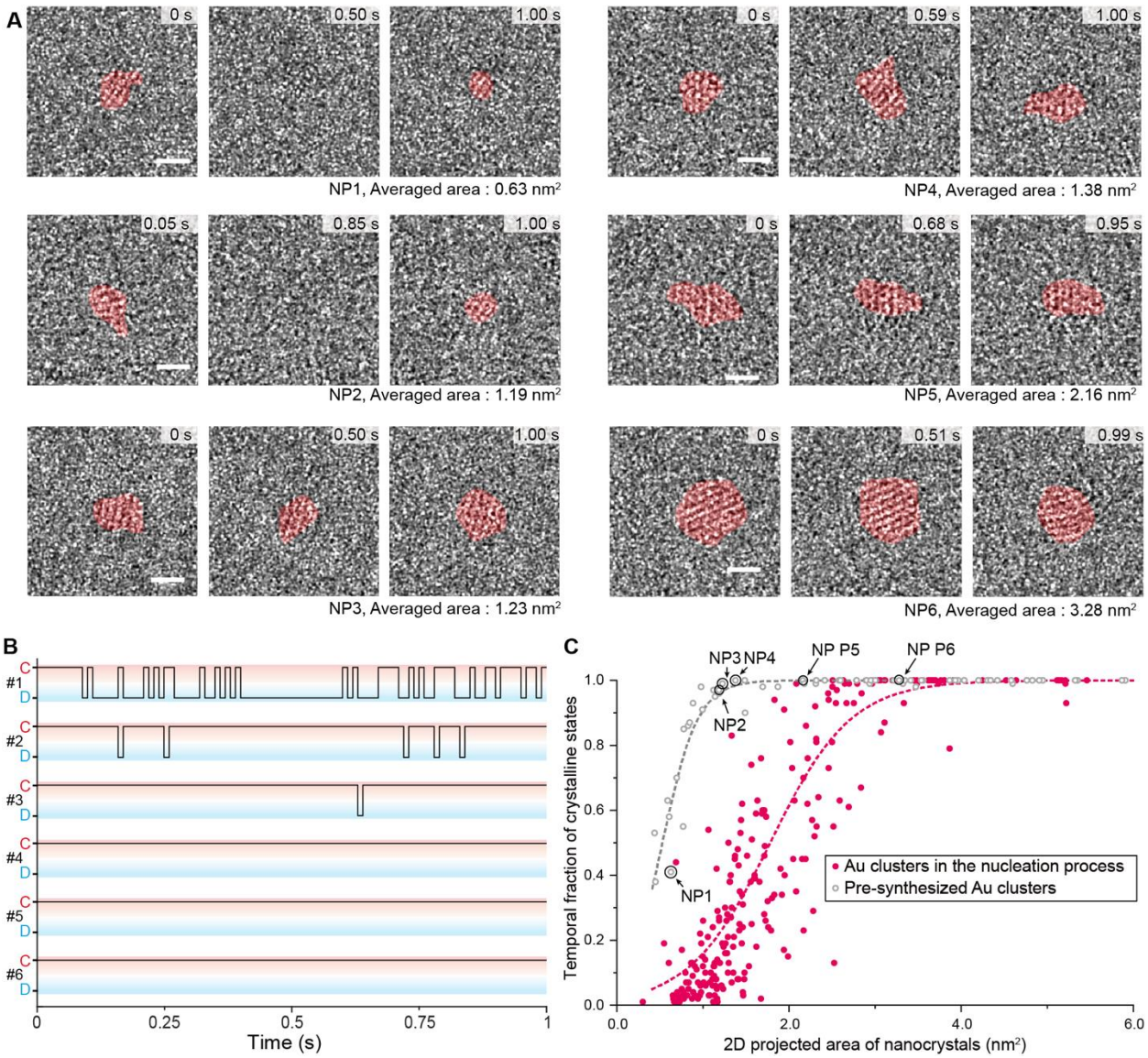

Fig. S32. Direct observation of pre-synthesized Au nanoclusters under the same e-beam conditions used in the experiment shown in Fig. 1 (Current density: 7.0×10^6 A/m^2, Accelerating voltage: 300 kV, Temporal resolution: 10 ms). (**A**) Selected frames from the in-situ TEM movies observing pre-synthesized Au nanoclusters. Scale bar: 1 nm. (**B**) Trajectories of structural transitions between disordered and crystalline states. (**C**) Temporal fraction of crystalline states versus 2D projected area of Au nanocrystals observed during the nucleation process (magenta dots) and observed using pre-synthesized Au nanoclusters (gray triangles). The dashed curves represent fitting lines to the data with sigmoid (logistic) functions.

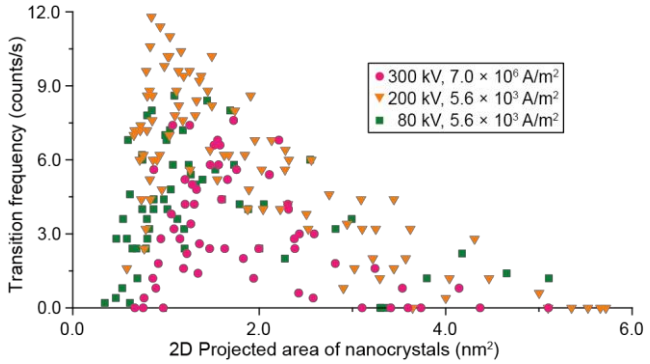

Fig. S33. Average frequency of structural transitions versus 2D projected area of nanocrystals for different electron beam conditions. All in-situ TEM movies captured at the three different conditions (Figs. 2A to 2C) were frame-averaged to have an identical temporal resolution (40 ms), and both C-to-D and C-to-D transition events were counted from the movies (time period: 5 s) to obtain transition frequencies.

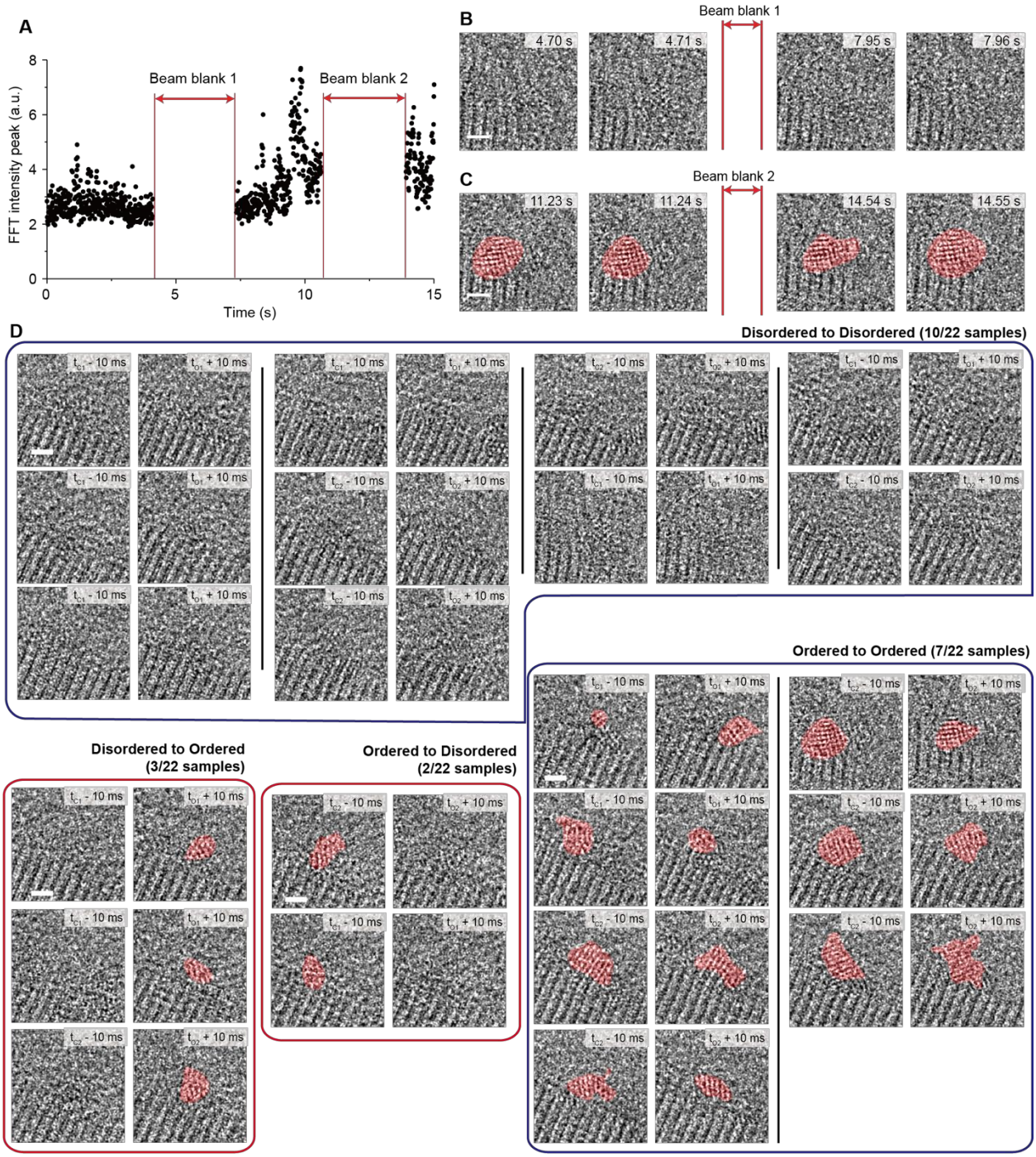

Fig. S34. in-situ TEM of the nucleation process with periodic switching of the e-beam (Current density: 7.0×10^6 A/m^2, Accelerating voltage: 300 kV, Temporal resolution: 10 ms). (**A**) FFT intensity peak of a nucleation site showing two periods (4.72 – 7.94 s and 11.25 – 14.53 s) when the e-beam is blanked. (**B** and **C**) TEM images of the nucleation cite right before and after the e-beam blanking periods. Scale bars: 1 nm. (**D**) Summary of the structural changes observed using the 22 periods of e-beam blanking.

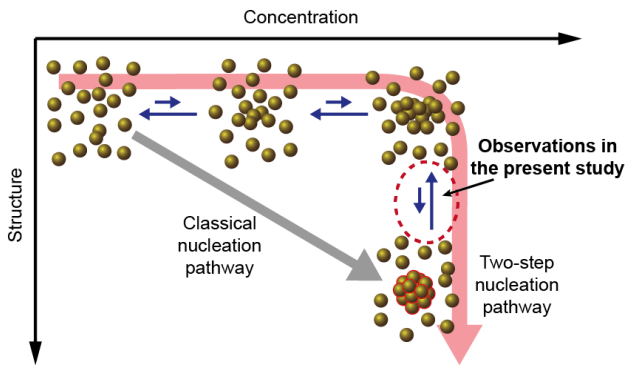

Fig. S35. Schematic illustration of the two-step mechanism of crystal nucleation. On the original illustration (*2, 64, 65*), additional information indicating the contribution of this work is overlaid. Early theories of non-classical two-step nucleation (*65*) included the hypothesis of "structure fluctuation" that may imply reversible transformations between disordered and crystalline states. However, only a few studies (*7*, *17*, *32*) have investigated the hypothesis, which is reintroduced as well as experimentally verified by this work.

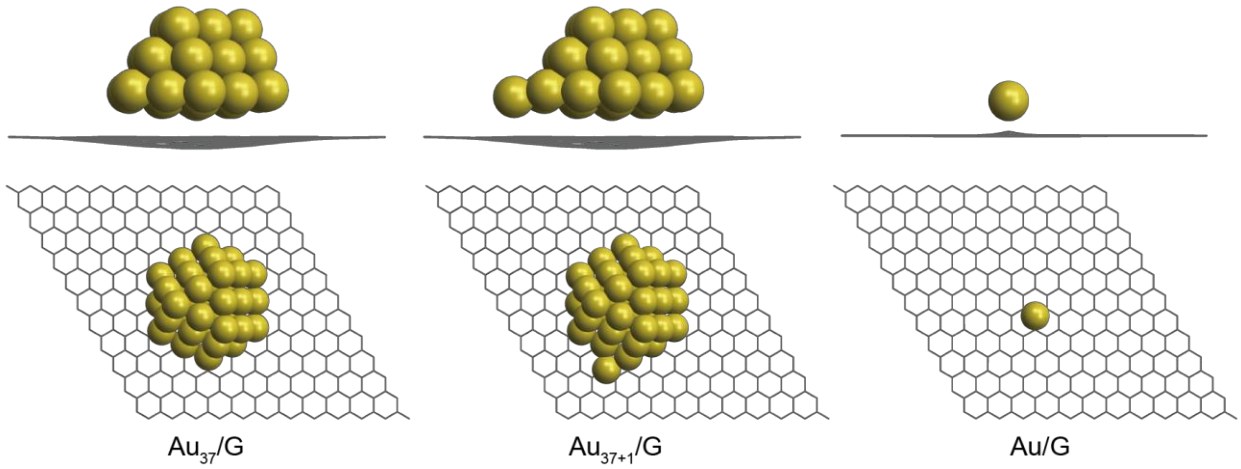

Fig. S36. Illustration of the optimized geometries of Au_n/G, Au_{n+1}/G, and Au/G models for the case of n = 37. The first row shows a side view, and the second row shows a top view of each model. The drawn geometry of Au_{37+1}/G corresponds to one of the different binding modes considered for Au_{37}/G (see fig. S37).

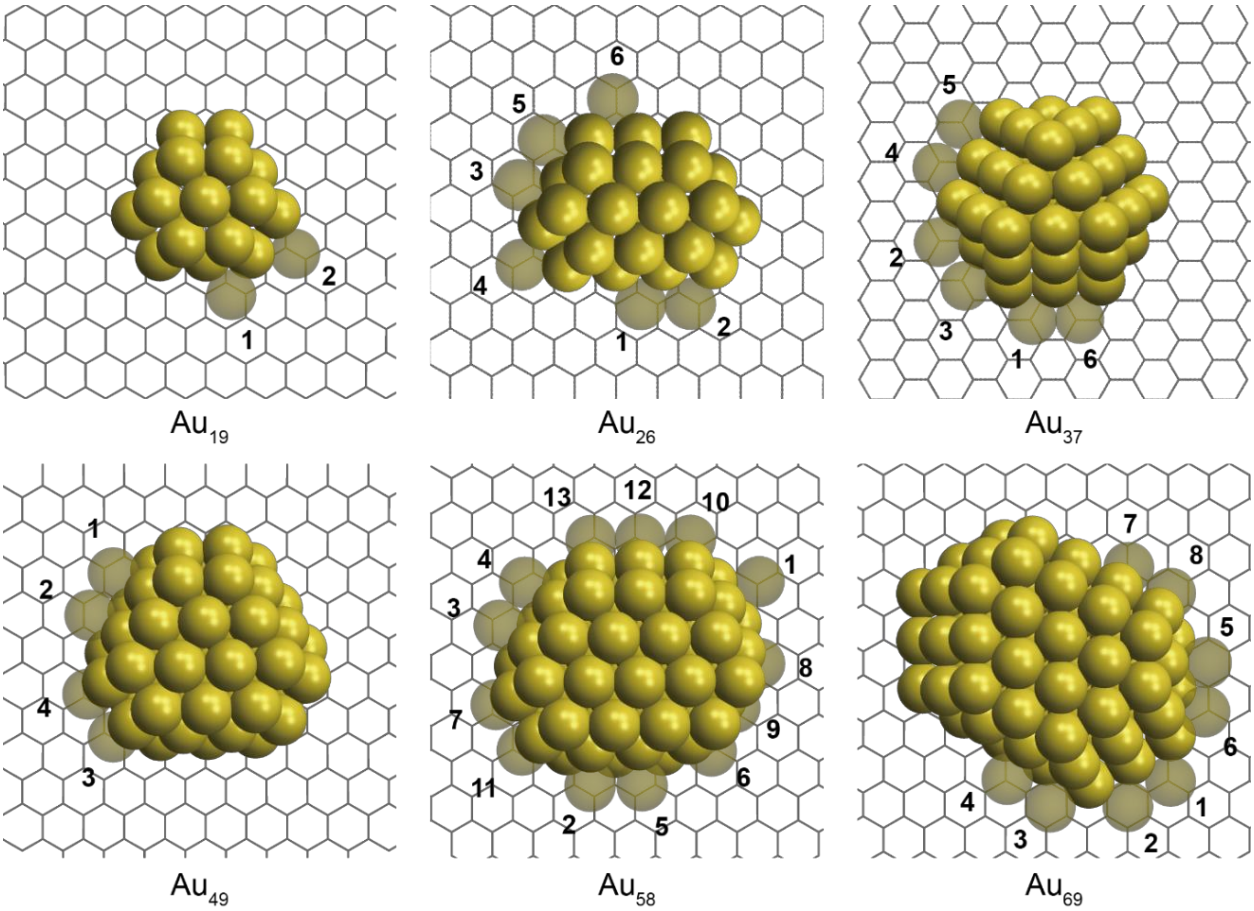

Fig. S37. The binding sites of the model nanocrystals considered in the calculation. Each of the semi-transparent spheres indicates the optimized position of the Au atom bound to the site. The resulting binding energies are listed in Table 1, with the same site indices.

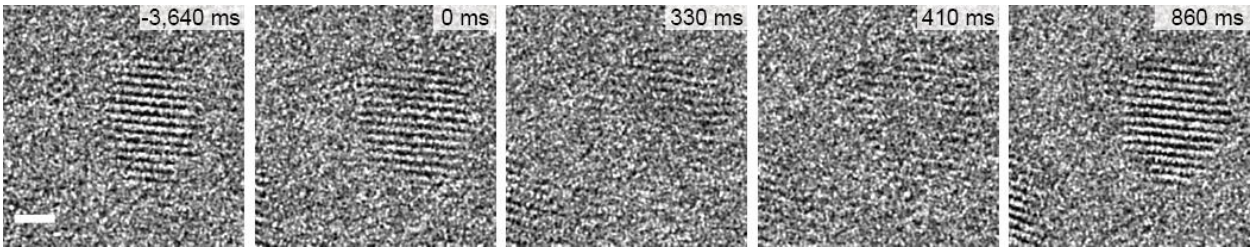

Fig. S38. In-situ TEM images (from movie S6) showing the binding of a small nanocluster to a large nanocrystal (Uncolored version of Fig. 3D). The binding of a small nanocluster induced a partially disordered structure in a nanocrystal. After that, the disordered area was recrystallized. Comparing the area of the nanoparticle before and after the binding event, the nanoparticle grew from 9.0 to 10.0 nm^2.

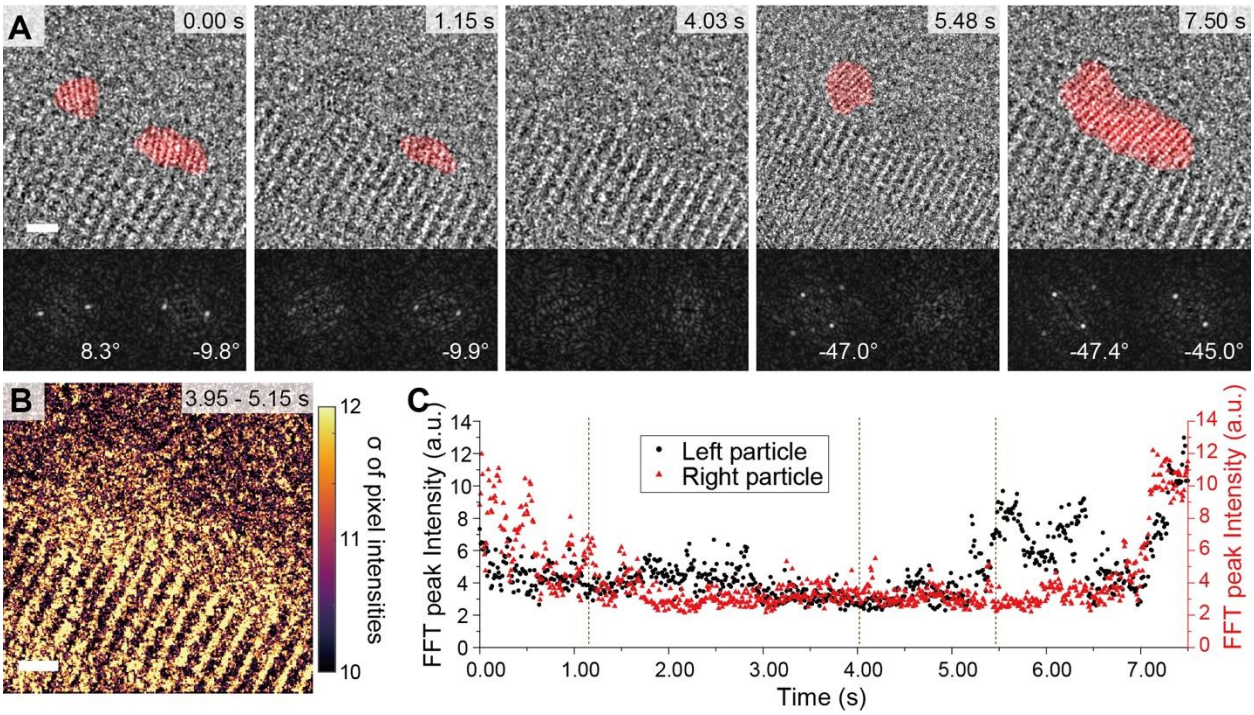

Fig. S39. Direct observation of gold nanoparticle coalescence. (**A**) Sequential TEM images of the nanocrystal coalescence. Crystal orientations of the two original nanocrystals (8.3° and -9.85° ± 0.05°) at 0 or 1.15 s were distinct from that of the merged nanocrystal (ranged from -45.0° to -47.4°) at 5.48 or 7.50 s, which implies that the initial crystalline structures collapsed before re-crystallization. (**B**) A color map obtained from standard deviations of intensities from 3.95 to 5.15 s for each pixel. Scale bar: 1 nm. (**C**) The maximum intensity of the FFT image from the left (black) and right (red) nanocrystal as a function of time. Vertical dotted lines and axes correspond to the time-labeled images in (A).

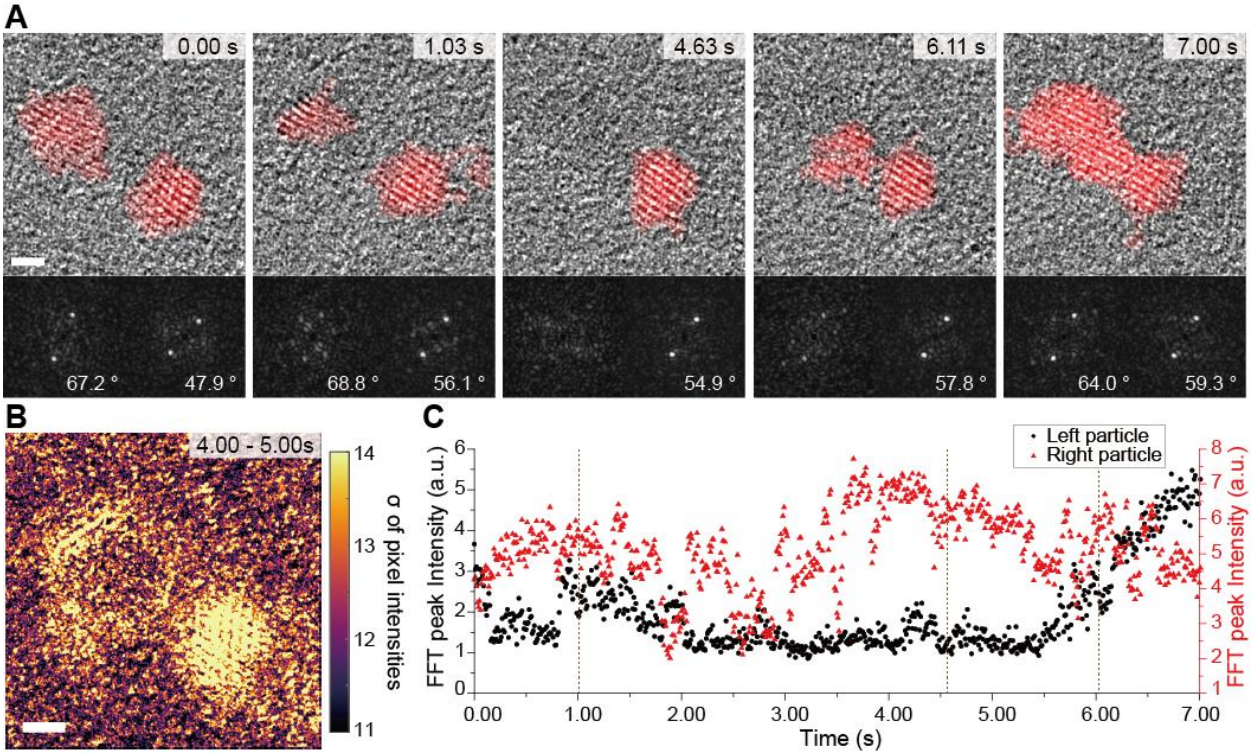

Fig. S40. Direct observation of gold nanoparticle coalescence. (**A**) Snapshots of the in-situ TEM movie showing coalescence of two nanocrystals. Scale bar: 1 nm. The lower-left and lower-right images respectively show FFT images of the left and right nanoparticles. (**B**) A color map obtained from standard deviations of intensities from 4.00 to 5.00 s for each pixel. Scale bar: 1 nm. (**C**) The maximum intensity of the FFT image from the left (black) and right (red) nanocrystal as a function of time. Vertical dotted lines and axes correspond to the time-labeled images in (A).

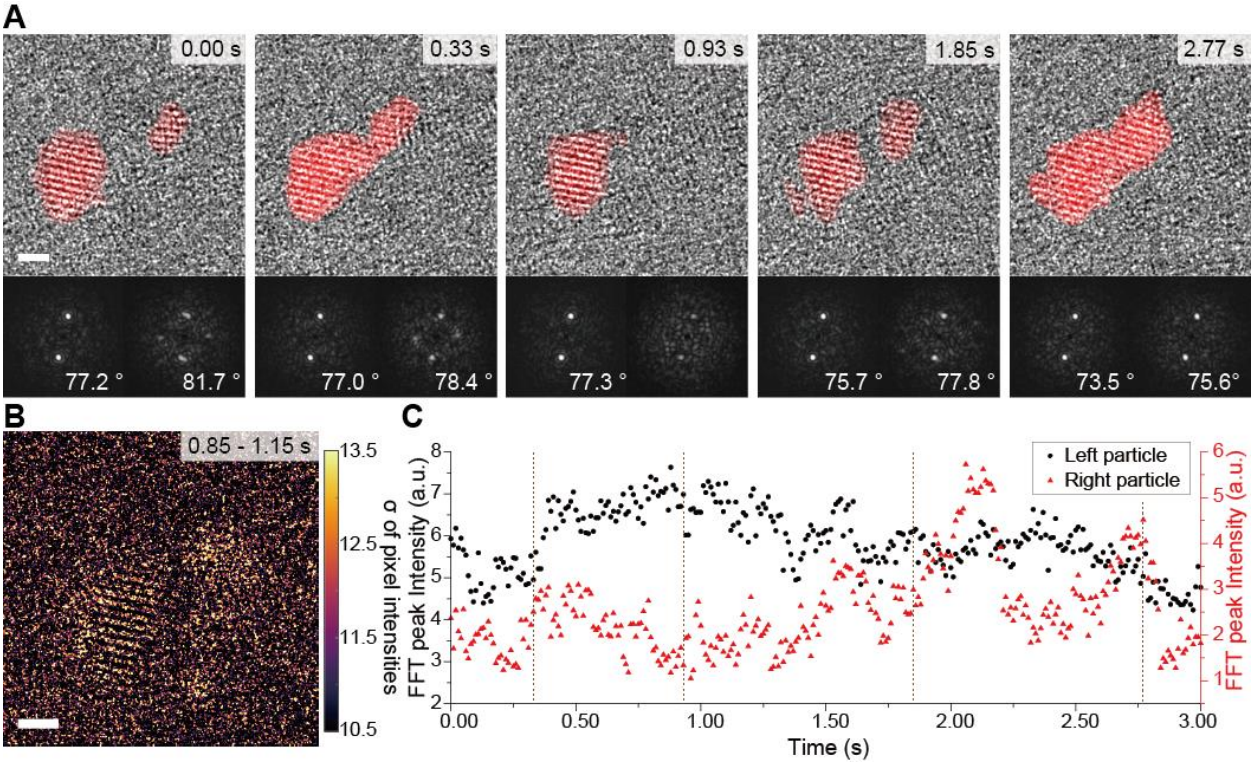

Fig. S41. Direct observation of gold nanoparticle coalescence. (**A**) Snapshots of the in-situ TEM movie showing coalescence of two nanocrystals. Scale bar: 1 nm. The lower-left and lower-right images show FFT images of the left and right nanoparticles, respectively. (**B**) A color map obtained from standard deviations of intensities from 0.85 to 1.15 s for each pixel. Scale bar: 1 nm. (**C**) The maximum intensity of the FFT image from the left (black) and right (red) nanocrystal as a function of time. Vertical dotted lines and axes correspond to the time-labeled images in (A).

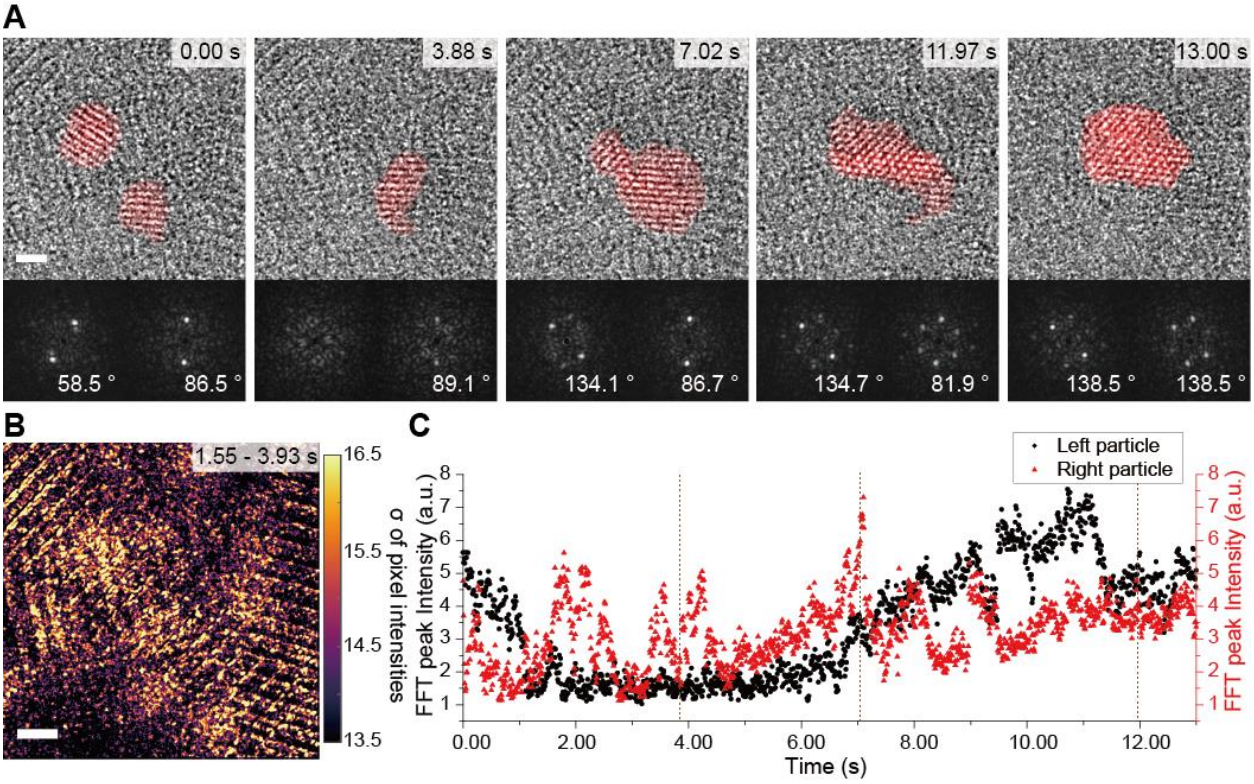

Fig. S42. Direct observation of gold nanoparticle coalescence. (**A**) Snapshots of the in-situ TEM movie showing coalescence of two nanocrystals. Scale bar: 1 nm. The lower-left and lower-right images show FFT images of the left and right nanoparticles, respectively. (**B**) A color map obtained from standard deviations of intensities from 1.55 to 3.93 s for each pixel. Scale bar: 1 nm. (**C**) The maximum intensity of the FFT image from the left (black) and right (red) nanocrystal as a function of time. Vertical dotted lines and axes correspond to the time-labeled images in (A).

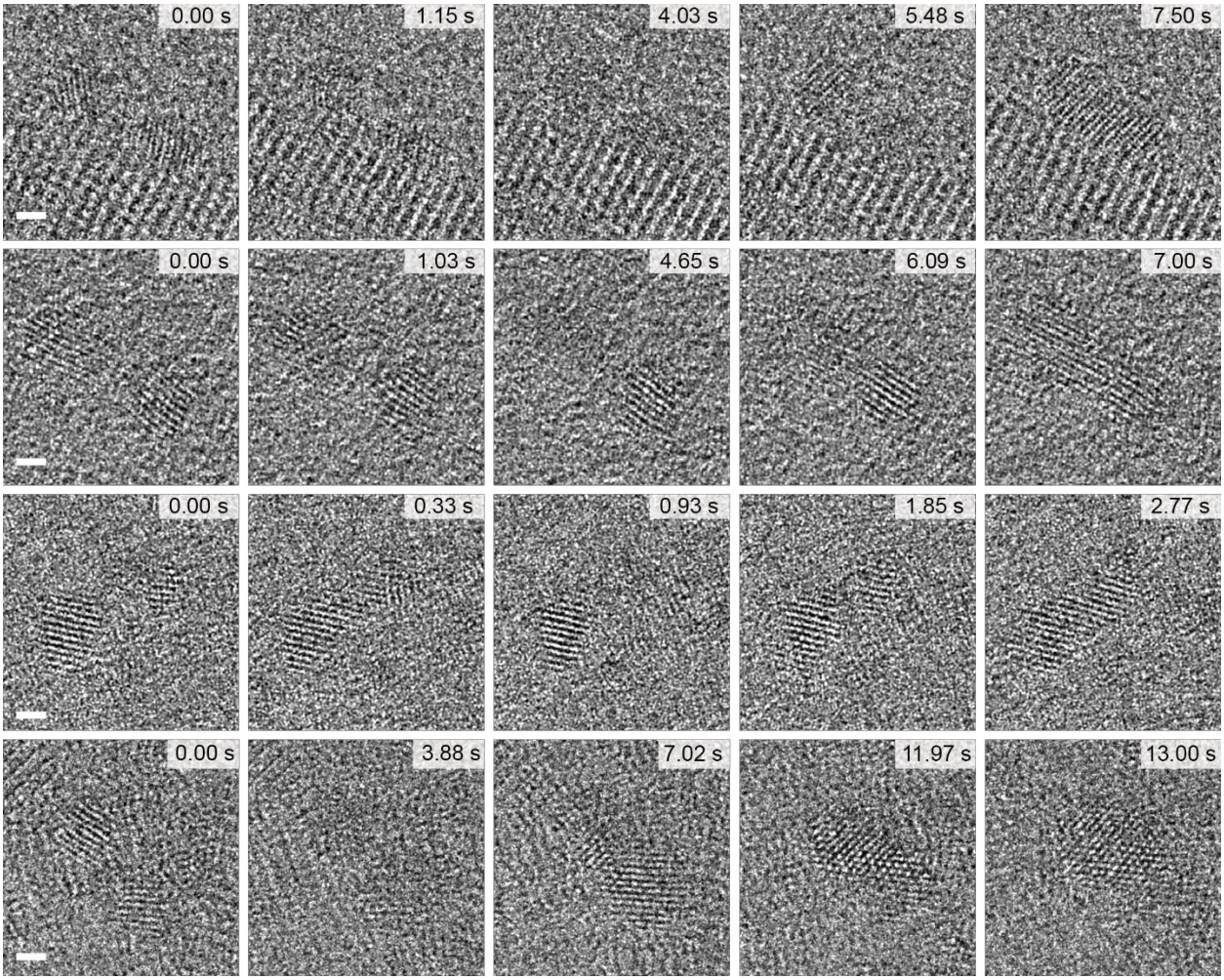

Fig. S43. Four sets of in-situ TEM images showing coalescence of two Au nanocrystals. The uncolored version of figs. S39A, S40A, S41A, S42A. Scale bars: 1 nm.

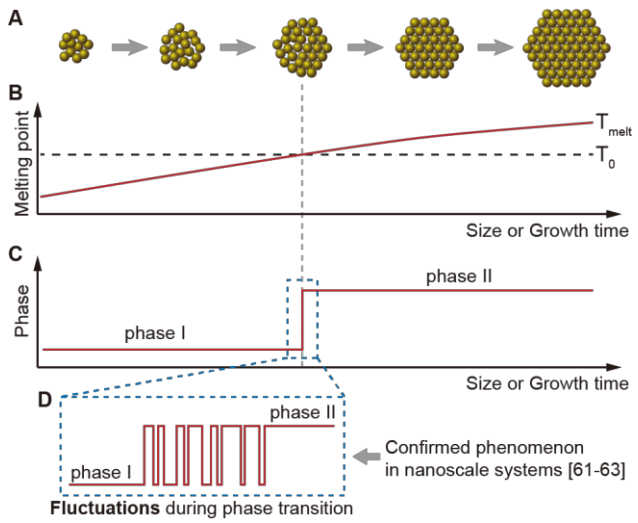

Fig. S44. Structural fluctuations in the early stage of crystallization. (**A**) Schematic illustration of the early-stage growth of a nucleus. (**B**) Melting temperature change of a nucleus depending on its size or growth time. Due to melting point depression (*29-31, 59*), a nucleus under a certain size can have a melting temperature lower than its reaction temperature (T_0). (**C**) Trajectory of phase transition expected based on (B) in an infinite-sized system. (**D**) Trajectory of phase transition in the growing nucleus. It was previously confirmed that fluctuations between two phases occur at the phase transition point in nanoscale systems (*61-63*).

Table S1. Calculated binding energies between the model Au_n nanocrystals and an Au atom

	Au_{19+1}	Au_{26+1}	Au_{37+1}	Au_{49+1}	Au_{58+1}	Au_{69+1}
			Binding energy (meV/atom)			
Site 1*	-106.4600	-80.8183	-62.2389	-46.7994	-38.7272	-38.8945
Site 2*	-108.2914	-85.7674	-63.4229	-52.7328	-41.4817	-39.2079
Site 3*		-92.1165	-64.5056	-57.4084	-42.4711	-40.4647
Site 4*		-92.3106	-64.5734	-60.7156	-42.7772	-40.9609
Site 5*		-93.3671	-65.9566		-42.8435	-41.3303
Site 6*		-99.4372	-67.4450		-43.9642	-42.4198
Site 7*					-44.0544	-42.9133
Site 8*					-44.1694	-42.9947
Site 9*					-44.5119	
Site 10*					-44.9023	
Site 11*					-45.3808	
Site 12*					-45.9517	
Site 13*					-46.2825	

*Different binding sites. Each index denotes the corresponding site depicted in fig. S37.

Table S2. Diameters and calculated melting temperatures of the model Au_{n+1} nanocrystals

Au_{n+1}	d^*	T_{melt}† (*29*)	T_{melt}‡ (*30*)	T_{melt}‖ (*31*)
Au_{20}	1.121 nm	404.301 K	345.907 K	306.167 K
Au_{27}	1.249 nm	500.066 K	447.667 K	412.008 K
Au_{38}	1.268 nm	512.923 K	461.330 K	426.218 K
Au_{50}	1.417 nm	599.611 K	553.444 K	522.026 K
Au_{59}	1.475 nm	628.488 K	584.130 K	553.942 K
Au_{70}	1.584 nm	676.947 K	635.623 K	607.500 K

*The diameters of the nanocrystals used in the calculations. The values were obtained by assuming the nanocrystals as hemispheres.

†Eq. 14 and the parameters in Table I (*29*). For the solid surface tension γ_s we used 1.409 J m^{-2}, which is the value the authors obtained by fitting Eq. 13 to their experimental data.

‡Eq. 2 and the parameters in the main text (*30*).

‖Eq. 10 with $\alpha = 1$ and $r = 0.144$ nm (*31*).

Table S3. Energies required to reach the melting temperatures of the model Au_{n+1} nanocrystals from the initial temperature 300 K

Au_{n+1}	*E* for T_{melt} (*29*) (meV/atom)	*E* for T_{melt} (*30*) (meV/atom)	*E* for T_{melt} (*31*) (meV/atom)
Au_{20}	23.9625	10.5245	1.4111
Au_{27}	47.3894	34.9349	26.4720
Au_{38}	51.6326	39.0783	30.5456
Au_{50}	73.7285	62.3236	54.5676
Au_{59}	81.3809	70.3483	62.8443
Au_{70}	93.9759	83.6339	76.5984

Captions for movies S1 to S7

Movie S1. In-situ TEM movie showing the nucleation and growth processes of gold nanocrystals on graphene. Snapshots from this movie are presented in Fig. 1A (temporal resolution: 10 ms) and fig. S3 (effective temporal resolution: 0.5 s). The accelerating voltage and current density are 300 kV and 7.0×10^6 A/m^2, respectively. The movie plays in real-time. Scale bar: 5 nm.

Movie S2. High-speed in-situ TEM movie of the crystal nucleation process in Fig. 1B (temporal resolution: 10 ms, frame rate: 100 fps). The accelerating voltage and current density are 300 kV and 7.0×10^6 A/m^2, respectively. The movie plays 2 times slower than real-time. Scale bar: 1 nm.

Movie S3. High-speed in-situ TEM movie of the crystal nucleation process in fig. S25 captured with a higher temporal resolution of 1.6 ms (frame rate: 624 fps). The accelerating voltage and current density are 200 kV and 6.1×10^7 A/m^2, respectively. The movie plays 12 times slower than real-time. Scale bar: 1 nm.

Movie S4. In-situ TEM movie of the crystal nucleation process in fig. S26 (temporal resolution: 26 ms, frame rate: 38.1 fps). The accelerating voltage and current density are 80 kV and 5.9×10^5 A/m^2, respectively. The movie plays in real-time. Scale bar: 1 nm.

Movie S5. High-speed in-situ TEM movie of the crystal nucleation process in fig. S29 (temporal resolution: 40 ms, frame rate: 25 fps). The accelerating voltage and current density are 200 kV and 6.6×10^2 A/m^2, respectively. The movie plays 4 times faster than real-time. Scale bar: 1 nm.

Movie S6. High-speed in-situ TEM movie showing the binding process of a small nanocluster to a relatively large nanocrystal in Fig. 3D (temporal resolution: 10 ms, frame rate: 100 fps). The accelerating voltage and current density are 300 kV and 7.0×10^6 A/m^2, respectively. The movie plays 10 times slower than real-time. Scale bar: 1 nm.

Movie S7. In-situ TEM movie showing the coalescence process of two nanocrystals in Fig. 3G (temporal resolution: 10 ms, frame rate: 100 fps). The accelerating voltage and current density are 300 kV and 7.0×10^6 A/m^2, respectively. The movie plays in real-time. Scale bar: 1 nm.

References and Notes

1. J. J. De Yoreo, P. U. P. A. Gilbert, N. A. J. M. Sommerdijk, R. L. Penn, S. Whitelam, D. Joester, H. Zhang, J. D. Rimer, A. Navrotsky, J. F. Banfield, A. F. Wallace, F. M. Michel, F. C. Meldrum, H. Cölfen, P. M. Dove, Crystallization by particle attachment in synthetic, biogenic, and geologic environments. *Science* **349**, aaa6760 (2015). doi:10.1126/science.aaa6760 Medline

2. P. G. Vekilov, Nucleation. *Cryst. Growth Des.* **10**, 5007–5019 (2010). doi:10.1021/cg1011633 Medline

3. D. Erdemir, A. Y. Lee, A. S. Myerson, Nucleation of crystals from solution: Classical and two-step models. *Acc. Chem. Res.* **42**, 621–629 (2009). doi:10.1021/ar800217x Medline

4. J. Chen, E. Zhu, J. Liu, S. Zhang, Z. Lin, X. Duan, H. Heinz, Y. Huang, J. J. De Yoreo, Building two-dimensional materials one row at a time: Avoiding the nucleation barrier. *Science* **362**, 1135–1139 (2018). doi:10.1126/science.aau4146 Medline

5. M. Sleutel, J. Lutsko, A. E. S. Van Driessche, M. A. Durán-Olivencia, D. Maes, Observing classical nucleation theory at work by monitoring phase transitions with molecular precision. *Nat. Commun.* **5**, 5598 (2014). doi:10.1038/ncomms6598 Medline

6. Z. Ou, Z. Wang, B. Luo, E. Luijten, Q. Chen, Kinetic pathways of crystallization at the nanoscale. *Nat. Mater.* **19**, 450–455 (2020). doi:10.1038/s41563-019-0514-1 Medline

7. T. H. Zhang, X. Y. Liu, Nucleation: What happens at the initial stage? *Angew. Chem. Int. Ed.* **48**, 1308–1312 (2009). doi:10.1002/anie.200804743 Medline

8. P. R. ten Wolde, D. Frenkel, Enhancement of protein crystal nucleation by critical density fluctuations. *Science* **277**, 1975–1978 (1997). doi:10.1126/science.277.5334.1975 Medline

9. L. Houben, H. Weissman, S. G. Wolf, B. Rybtchinski, A mechanism of ferritin crystallization revealed by cryo-STEM tomography. *Nature* **579**, 540–543 (2020). doi:10.1038/s41586-020-2104-4 Medline

10. M. H. Nielsen, S. Aloni, J. J. De Yoreo, In situ TEM imaging of $CaCO_3$ nucleation reveals coexistence of direct and indirect pathways. *Science* **345**, 1158–1162 (2014). doi:10.1126/science.1254051 Medline

11. A. S. Barnard, N. P. Young, A. I. Kirkland, M. A. van Huis, H. Xu, Nanogold: A quantitative phase map. *ACS Nano* **3**, 1431–1436 (2009). doi:10.1021/nn900220k Medline

12. N. D. Loh, S. Sen, M. Bosman, S. F. Tan, J. Zhong, C. A. Nijhuis, P. Král, P. Matsudaira, U. Mirsaidov, Multistep nucleation of nanocrystals in aqueous solution. *Nat. Chem.* **9**, 77–82 (2017). doi:10.1038/nchem.2618 Medline

13. J. Yang, J. Koo, S. Kim, S. Jeon, B. K. Choi, S. Kwon, J. Kim, B. H. Kim, W. C. Lee, W. B. Lee, H. Lee, T. Hyeon, P. Ercius, J. Park, Amorphous-phase-mediated crystallization of Ni nanocrystals revealed by high-resolution liquid-phase electron microscopy. *J. Am. Chem. Soc.* **141**, 763–768 (2019). doi:10.1021/jacs.8b11972 Medline

14. M. H. Hu, S. Noda, H. Komiyama, Amorphous-to-crystalline transition during the early stages of thin film growth of Cr on SiO_2. *J. Appl. Phys.* **93**, 9336–9344 (2003). doi:10.1063/1.1571214

15. L. Fei, X. Gan, S. M. Ng, H. Wang, M. Xu, W. Lu, Y. Zhou, C. W. Leung, C.-L. Mak, Y. Wang, Observable two-step nucleation mechanism in solid-state formation of tungsten carbide. *ACS Nano* **13**, 681–688 (2019). doi:10.1021/acsnano.8b07864 Medline

16. J. Zhou, Y. Yang, Y. Yang, D. S. Kim, A. Yuan, X. Tian, C. Ophus, F. Sun, A. K. Schmid, M. Nathanson, H. Heinz, Q. An, H. Zeng, P. Ercius, J. Miao, Observing crystal nucleation in four dimensions using atomic electron tomography. *Nature* **570**, 500–503 (2019). doi:10.1038/s41586-019-1317-x Medline

17. K. Cao, J. Biskupek, C. T. Stoppiello, R. L. McSweeney, T. W. Chamberlain, Z. Liu, K. Suenaga, S. T. Skowron, E. Besley, A. N. Khlobystov, U. Kaiser, Atomic mechanism of metal crystal nucleus formation in a single-walled carbon nanotube. *Nat. Chem.* **12**, 921–928 (2020). doi:10.1038/s41557-020-0538-9 Medline

18. B. W. Reed, A. A. Moghadam, R. S. Bloom, S. T. Park, A. M. Monterrosa, P. M. Price, C. M. Barr, S. A. Briggs, K. Hattar, J. T. McKeown, D. J. Masiel, Electrostatic subframing and compressive-sensing video in transmission electron microscopy. *Struct. Dyn.* **6**, 054303 (2019). doi:10.1063/1.5115162 Medline

19. W. C. Lee, K. Kim, J. Park, J. Koo, H. Y. Jeong, H. Lee, D. A. Weitz, A. Zettl, S. Takeuchi, Graphene-templated directional growth of an inorganic nanowire. *Nat. Nanotechnol.* **10**, 423–428 (2015). doi:10.1038/nnano.2015.36 Medline

20. J. Kim, K. Lim, Y. Lee, J. Kim, K. Kim, J. Park, K. Kim, W. C. Lee, Precise identification of graphene's crystal structures by removable nanowire epitaxy. *J. Phys. Chem. Lett.* **8**, 1302–1309 (2017). doi:10.1021/acs.jpclett.7b00279 Medline

21. M. T. Beck, I. Bertóti, M. Mohai, P. Németh, E. Jakab, L. Szabó, J. Szépvölgyi, Gold nano-particle formation from crystalline AuCN: Comparison of thermal, plasma- and ion-beam activated decomposition. *J. Solid State Chem.* **246**, 65–74 (2017). doi:10.1016/j.jssc.2016.10.031

22. Z. W. Wang, R. E. Palmer, Experimental evidence for fluctuating, chiral-type Au55 clusters by direct atomic imaging. *Nano Lett.* **12**, 5510–5514 (2012). doi:10.1021/nl303429z Medline

23. T. J. Pennycook, J. R. McBride, S. J. Rosenthal, S. J. Pennycook, S. T. Pantelides, Dynamic fluctuations in ultrasmall nanocrystals induce white light emission. *Nano Lett.* **12**, 3038–3042 (2012). doi:10.1021/nl3008727 Medline

24. P. M. Ajayan, L. D. Marks, Experimental evidence for quasimelting in small particles. *Phys. Rev. Lett.* **63**, 279–282 (1989). doi:10.1103/PhysRevLett.63.279 Medline

25. V. Petkov, N. Bedford, M. R. Knecht, M. G. Weir, R. M. Crooks, W. Tang, G. Henkelman, A. Frenkel, Periodicity and atomic ordering in nanosized particles of crystals. *J. Phys. Chem. C* **112**, 8907–8911 (2008). doi:10.1021/jp801195c

26. L. Li, L.-L. Wang, D. D. Johnson, Z. Zhang, S. I. Sanchez, J. H. Kang, R. G. Nuzzo, Q. Wang, A. I. Frenkel, J. Li, J. Ciston, E. A. Stach, J. C. Yang, Noncrystalline-to-

crystalline transformations in Pt nanoparticles. *J. Am. Chem. Soc.* **135**, 13062–13072 (2013). doi:10.1021/ja405497p Medline

27. Y. Sun, L. Zhuang, J. Lu, X. Hong, P. Liu, Collapse in crystalline structure and decline in catalytic activity of Pt nanoparticles on reducing particle size to 1 nm. *J. Am. Chem. Soc.* **129**, 15465–15467 (2007). doi:10.1021/ja076177b Medline

28. I. L. Garzón, K. Michaelian, M. R. Beltrán, A. Posada-Amarillas, P. Ordejón, E. Artacho, D. Sánchez-Portal, J. M. Soler, Lowest energy structures of gold nanoclusters. *Phys. Rev. Lett.* **81**, 1600–1603 (1998). doi:10.1103/PhysRevLett.81.1600

29. P. Buffat, J. P. Borel, Size effect on melting temperature of gold particles. *Phys. Rev. A* **13**, 2287–2298 (1976). doi:10.1103/PhysRevA.13.2287

30. K. Dick, T. Dhanasekaran, Z. Zhang, D. Meisel, Size-dependent melting of silica-encapsulated gold nanoparticles. *J. Am. Chem. Soc.* **124**, 2312–2317 (2002). doi:10.1021/ja017281a Medline

31. W. H. Qi, M. P. Wang, Size and shape dependent melting temperature of metallic nanoparticles. *Mater. Chem. Phys.* **88**, 280–284 (2004). doi:10.1016/j.matchemphys.2004.04.026

32. P. W. Sutter, E. A. Sutter, Dispensing and surface-induced crystallization of zeptolitre liquid metal-alloy drops. *Nat. Mater.* **6**, 363–366 (2007). doi:10.1038/nmat1894 Medline

33. W. Regan, N. Alem, B. Alemán, B. Geng, Ç. Girit, L. Maserati, F. Wang, M. Crommie, A. Zettl, A direct transfer of layer-area graphene. *Appl. Phys. Lett.* **96**, 113102 (2010). doi:10.1063/1.3337091

34. M. Azubel, J. Koivisto, S. Malola, D. Bushnell, G. L. Hura, A. L. Koh, H. Tsunoyama, T. Tsukuda, M. Pettersson, H. Häkkinen, R. D. Kornberg, Electron microscopy of gold nanoparticles at atomic resolution. *Science* **345**, 909–912 (2014). doi:10.1126/science.1251959 Medline

35. M. Brust, M. Walker, D. Bethell, D. J. Schiffrin, R. Whyman, Synthesis of thiol-derivatised gold nanoparticles in a two-phase Liquid–Liquid system. *Chem. Commun.* **1994**, 801–802 (1994). doi:10.1039/C39940000801

36. X. Yuan, B. Zhang, Z. Luo, Q. Yao, D. T. Leong, N. Yan, J. Xie, Balancing the rate of cluster growth and etching for gram-scale synthesis of thiolate-protected Au_{25} nanoclusters with atomic precision. *Angew. Chem. Int. Ed.* **126**, 4711–4715 (2014). doi:10.1002/ange.201311177

37. B. W. Reed, S. T. Park, D. J. Masiel, Beyond movie mode: Bridging the gap of time resolution. *Microsc. Microanal.* **22**, 706–707 (2016). doi:10.1017/S1431927616004384

38. T. LaGrange, B. W. Reed, D. J. Masiel, Movie-mode dynamic electron microscopy. *MRS Bull.* **40**, 22–28 (2015). doi:10.1557/mrs.2014.282

39. M. J. Hytch, Analysis of variations in structure from high resolution electron microscope images by combining real space and Fourier space information. *Microsc. Microanal. Microstruct.* **8**, 41–57 (1997). doi:10.1051/mmm:1997105

40. E. J. Kirkland, *Advanced Computing in Electron Microscopy* (Springer, 2010).

41. J. A. Venables, G. D. T. Spiller, M. Hanbucken, Nucleation and growth of thin films. *Rep. Prog. Phys.* **47**, 399–459 (1984). doi:10.1088/0034-4885/47/4/002

42. Z. W. Wang, R. E. Palmer, in *Frontiers of Nanoscience*, vol. 9, T. Tsukuda, H. Häkkinen, Eds. (Elsevier, 2015), pp. 127–159.

43. R. F. Egerton, Choice of operating voltage for a transmission electron microscope. *Ultramicroscopy* **145**, 85–93 (2014). doi:10.1016/j.ultramic.2013.10.019 Medline

44. R. F. Egerton, P. Li, M. Malac, Radiation damage in the TEM and SEM. *Micron* **35**, 399–409 (2004). doi:10.1016/j.micron.2004.02.003 Medline

45. R. F. Egerton, Beam-induced motion of adatoms in the transmission electron microscope. *Microsc. Microanal.* **19**, 479–486 (2013). doi:10.1017/S1431927612014274 Medline

46. A. T. N'Diaye, T. Gerber, C. Busse, J. Mysliveček, J. Coraux, T. Michely, A versatile fabrication method for cluster superlattices. *New J. Phys.* **11**, 103045 (2009). doi:10.1088/1367-2630/11/10/103045

47. I. G. Gonzalez-Martinez, A. Bachmatiuk, V. Bezugly, J. Kunstmann, T. Gemming, Z. Liu, G. Cuniberti, M. H. Rümmeli, Electron-beam induced synthesis of nanostructures: A review. *Nanoscale* **8**, 11340–11362 (2016). doi:10.1039/C6NR01941B Medline

48. O. Dyck, M. Ziatdinov, D. B. Lingerfelt, R. R. Unocic, B. M. Hudak, A. R. Lupini, S. Jesse, S. V. Kalinin, Atom-by-atom fabrication with electron beams. *Nat. Rev. Mater.* **4**, 497–507 (2019). doi:10.1038/s41578-019-0118-z

49. B. H. Kim, J. Yang, D. Lee, B. K. Choi, T. Hyeon, J. Park, Liquid-phase transmission electron microscopy for studying colloidal inorganic nanoparticles. *Adv. Mater.* **30**, 1703316 (2018). doi:10.1002/adma.201703316 Medline

50. D. Schebarchov, F. Baletto, D. J. Wales, Structure, thermodynamics, and rearrangement mechanisms in gold clusters-insights from the energy landscapes framework. *Nanoscale* **10**, 2004–2016 (2018). doi:10.1039/C7NR07123J Medline

51. G. te Velde, E. J. Baerends, Precise density-functional method for periodic structures. *Phys. Rev. B* **44**, 7888–7903 (1991). doi:10.1103/PhysRevB.44.7888 Medline

52. G. te Velde, F. M. Bickelhaupt, E. J. Baerends, C. Fonseca Guerra, S. J. A. van Gisbergen, J. G. Snijders, T. Ziegler, Chemistry with ADF. *J. Comput. Chem.* **22**, 931–967 (2001). doi:10.1002/jcc.1056

53. J. P. Perdew, K. Burke, M. Ernzerhof, Generalized gradient approximation made simple. *Phys. Rev. Lett.* **77**, 3865–3868 (1996). doi:10.1103/PhysRevLett.77.3865 Medline

54. S. Grimme, S. Ehrlich, L. Goerigk, Effect of the damping function in dispersion corrected density functional theory. *J. Comput. Chem.* **32**, 1456–1465 (2011). doi:10.1002/jcc.21759 Medline

55. E. van Lenthe, E. J. Baerends, J. G. Snijders, Relavistic total-energy using regular approximations. *J. Chem. Phys.* **101**, 9783–9792 (1994). doi:10.1063/1.467943

56. P. H. T. Philipsen, E. van Lenthe, J. G. Snijders, E. J. Baerends, Relativistic calculations on the adsorption of CO on the (111) surfaces of Ni, Pd, and Pt within the zeroth-order

regular approximation. *Phys. Rev. B* **56**, 13556–13562 (1997). doi:10.1103/PhysRevB.56.13556

57. D. A. McQuarrie, J. D. Simon, *Physical Chemistry: A Molecular Approach* (University Science Books, 1997).

58. M. Schwartzkopf, A. Buffet, V. Körstgens, E. Metwalli, K. Schlage, G. Benecke, J. Perlich, M. Rawolle, A. Rothkirch, B. Heidmann, G. Herzog, P. Müller-Buschbaum, R. Röhlsberger, R. Gehrke, N. Stribeck, S. V. Roth, From atoms to layers: In situ gold cluster growth kinetics during sputter deposition. *Nanoscale* **5**, 5053–5062 (2013). doi:10.1039/c3nr34216f Medline

59. P. Puri, V. Yang, Effect of particle size on melting of aluminum at nano scales. *J. Phys. Chem. C* **111**, 11776–11783 (2007). doi:10.1021/jp0724774

60. J. van Embden, A. S. Chesman, J. J. Jasieniak, The heat-up synthesis of colloidal nanocrystals. *Chem. Mater.* **27**, 2246–2285 (2015). doi:10.1021/cm5028964

61. H. E. Stanley, *Introduction to Phase Transitions and Critical Phenomena* (Oxford Univ. Press, 1987).

62. M. Challa, D. Landau, K. Binder, Monte Carlo studies of finite-size effects at first-order transitions. *Phase Transit.* **24-26**, 343–369 (1990). doi:10.1080/01411599008210236

63. H. Zheng, J. B. Rivest, T. A. Miller, B. Sadtler, A. Lindenberg, M. F. Toney, L.-W. Wang, C. Kisielowski, A. P. Alivisatos, Observation of transient structural-transformation dynamics in a Cu_2S nanorod. *Science* **333**, 206–209 (2011). doi:10.1126/science.1204713 Medline

64. P. G. Vekilov, The two-step mechanism of nucleation of crystals in solution. *Nanoscale* **2**, 2346–2357 (2010). doi:10.1039/c0nr00628a Medline

65. P. G. Vekilov, Dense liquid precursor for the nucleation of ordered solid phases from solution. *Cryst. Growth Des.* **4**, 671–685 (2004). doi:10.1021/cg049977w